# Brillouin Scattering in the Rare Gas Liquids and some Mixtures of the Rare Gases

by

Bin Yatim Baharudin

Thesis submitted for the degree of Ph.D.
at the University of Kent
at Canterbury

January, 1974

The Physics Laboratory,
The University,
Canterbury,
Kent.

To Aysah,

whose infinite patience throughout the
duration of this work is deeply appreciated

ACKNOWLEDGEMENTS

I wish to express my gratitude for the able guidance, encouragement and moral support and constructive criticisms of my supervisor, Dr. D.A. Jackson.

I am also indebted to Dr. P.E. Schoen, whose assistance both experimental and theoretical is invaluable and to Prof. J.G. Powles who has shown continued interest in this work.

Every member of the Light Scattering Group contributed in some way or another towards the success of this project, and for this I am grateful to them.

My thanks and great admiration are due to each and every member of the technical staff, mechanical and electronic, for their tolerance and skill which enabled this project to be completed.

I also wish to thank Miss Margaret Cross for undertaking the typing of this thesis.

Throughout the duration of this work I have been given leave of study and a maintenance grant by the National University of Malaysia, for which I am grateful.

B.Y. Baharudin

# CONTENTS

CHAPTER PAGE

# LIST OF FIGURES

# LIST OF TABLES

# ABSTRACT

We have observed the Brillouin scattering of light from the pure monatomic liquids Argon and Krypton and the binary monatomic gas mixtures Argon-Neon and Krypton-Helium.

The spectrum of light scattered from a fluid for a scattering process with momentum transfer $\bar{K}$ and frequency $\omega$ is proportional to the power spectrum, $S(\bar{K}, \omega)$, of fluctuations in the thermodynamic properties of the fluid. For a one-component system this reduces to the power spectrum of fluctuations in the density of the fluid; while for a binary mixture $S(\bar{K}, \omega)$ can be expressed as the total power spectrum of fluctuations in a set of independent thermodynamic variables.

When the fluid is dense the mean free path of the atoms (or molecules) is much smaller than the wavelength, $\Lambda$, associated with the scattering process ($\Lambda = 2\pi/K$) and the scattering process is dominated by interatomic collisions. In this case $S(\bar{K}, \omega)$ can be calculated from the equations of hydrodynamics.

The spectrum of light scattered from liquid Argon and liquid Krypton along their saturated vapour pressure curves has been measured. The experiments were performed over a range of scattering angles for both liquids. The velocities of hypersound in each liquid, calculated from the Brillouin shifts of the scattered light, show no dispersion over the frequency range measured, i.e.$\sim$300-3000 MHz.

These results also agree with sound velocities measured by ultrasonic techniques within the experimental errors.

We have also measured the Brillouin linewidths from these liquids, and from these calculated the intrinsic bulk viscosities of these liquids.

The spectrum of light scattered from the binary monatomic gas mixtures Argon-Neon and Krypton-Helium as a function of Neon and Helium concentrations respectively has been measured. From the shifts and widths of the Brillouin lines we have investigated the propagation and attenuation of sound waves in these mixtures. In the case of the Krytpon-Helium mixture measurements were also made at different scattering angles to investigate the dispersion of sound in this mixture.

From the measurements of the attenuation coefficients in the binary monatomic gas mixtures we have estimated the mutual diffusion coefficients, $D_{12}$, in these mixtures. The results obtained agree with theoretical calculations for atoms with the Lennard-Jones potential.

# CHAPTER I

# INTRODUCTION

## 1.1. Brillouin Scattering from a Fluid

The molecules (or atoms) in a fluid in a state of thermal equilibrium undergo chaotic random thermal motion. Thus if one considers a small volume element in the fluid one finds that the molecules (or atoms) move in and out of the volume element randomly. (The volume element considered here is small compared with the volume of the fluid as a whole but large enough to contain a large number of molecules (or atoms)). Because of this random movement the number of molecules (or atoms) contained in the volume element, and hence its density, is continuously fluctuating. These statistical density fluctuations give rise to sonic disturbances (Debye waves or phonons) which are propagated in all possible directions. The fluctuations are completely random, hence for every sound wave of given amplitude and frequency travelling in one direction one expects another wave of equal amplitude and frequency travelling in the opposite direction.

In 1922 Brillouin (1) applied the above concept of thermally driven elastic sound waves in a macroscopically homogeneous transparent medium to analyse the mechanism of the interaction of light with such a medium. He showed that for constructive interference of the light scattered from the sound waves the Bragg condition holds. That is the conservation of momentum in the scattering process requires the condition:

$$\bar{K} = \bar{k} - \bar{k}_s \qquad (1.1)$$

where $\bar{K}$ is the wave vector of the scattering sound wave, $\bar{k}$ and $\bar{k}_s$ are the wave vectors of the incident and scattered light respectively.

The sound waves in the scattering medium are travelling waves, thus the scattered light is Doppler shifted in frequency. Since there are two waves of the same amplitude and frequency with wave vector $\bar{K}$, travelling in opposite directions the Doppler shifts $\Delta\nu$ are:

$$\Delta\nu = \pm 2n\nu_0 \left(\frac{v}{c}\right) \sin\left(\frac{\theta}{2}\right) \qquad (1.2)$$

where n is the refractive index of the medium, v is the phase velocity of the scattering sound waves, $\nu_0$ and c are the frequency and velocity of the incident light and $\theta$ is the angle between the incident wave vector and the scattered wave vector (i.e. the scattering angle).

In this classical concept one can regard the positively Doppler shifted component of the scattered light (in equation (1.2)) as being scattered from the wave travelling towards the observer and the negatively Doppler shifted component as being scattered from the wave travelling away from the observer.

**Landau** and **Placzek** (2) developed the theory further using a macroscopic thermodynamic fluctuation theory. They showed that the spectrum of the scattered light consists of three lines: an unshifted central line and the two shifted lines predicted by Brillouin. The presence of the three lines has been shown by experimental observation (3).

Landau and Placzek showed that the central line is due to non-propagating fluctuations of entropy (or temperature) at constant pressure. The shifted 'Brillouin' doublets were shown to be due to adiabatic pressure fluctuations, i.e. sound waves. The results of the theory show that the ratio of the intensities of the unshifted line to that of the shifted lines is:

$$\frac{I_C + 2I_B}{2I_B} = \frac{\beta_T}{\beta_S} = \frac{C_p}{C_v} \qquad (1.3)$$

which is often rewritten in the form:

$$\frac{I_C}{2I_B} = \frac{\beta_T - \beta_S}{\beta_S} = \frac{C_p - C_v}{C_v} = \gamma - 1 \qquad (1.4)$$

In the above equations the symbols are as follows:

$I_C$ and $I_B$ are the intensities of the central line and Brillouin lines respectively, $\beta_T$ and $\beta_S$ are isothermal and adiabatic compressibilities of the medium, $C_p$ and $C_v$ are the specific heats of the medium at constant pressure and volume respectively and $\gamma$ is their ratio, $C_p/C_v$.

The line shapes were calculated by Landau and Placzek assuming that the fluctuation decayed back to equilibrium exponentially with time. Thus the lineshapes are Lorentzian with halfwidths proportional to the reciprocal relaxation time, $1/\tau$, characterising the decay of the fluctuations. For the central (Rayleigh) line the halfwidth, $\Gamma_C$, is related to the thermal diffusivity, $a_T$, and is given by:

$$\Gamma_C = a_T |K|^2 \tag{1.5}$$

where

$$a_T = \lambda/\rho C_p \tag{1.6}$$

Here $\lambda$ and $\rho$ are the thermal conductivity and mass density of the medium respectively and $\overline{K}$ is the wave vector of the scattering sound wave.

The linewidth of the shifted Brillouin lines, $\Gamma_B$, is associated with the damping of sound waves. This can be calculated from the equations of hydrodynamics and is given by (4):

$$\Gamma_B = \frac{1}{2\rho} |K|^2 \left[ \frac{4}{3} \eta_s + \frac{\lambda}{C_p} (\gamma - 1) \right] \tag{1.7}$$

where $\eta_s$ is the shear viscosity of the fluid.

Equation (1.7) gives the 'classical' sound attenuation coefficient. Experimental observation showed $\Gamma_B$ to be invariably larger than that given by equation (1.7). The 'excess' attenuation is normally attributed to the bulk or volume viscosity, $\eta_B$, of the fluid. Hence the observed halfwidth of the Brillouin lines is represented by:

$$\Gamma_B = \frac{1}{2\rho} |K|^2 \left[ \frac{4}{3}\eta_s + \eta_B + \frac{\lambda}{C_p} (\gamma - 1) \right] \tag{1.8}$$

In a light scattering experiement $\Gamma_B$ is measured and $\eta_B$ may be obtained from this provided the other thermodynamic coefficients in equation (1.8) are known.

## 1.2. The Spectrum of the Scattered Light

The advent of the laser towards the middle of the 1960's made available light sources of high intensity and narrow linewidth which were not previously attainable using any conventional optical source. The utilisation of the laser together with the improved resolution and detection efficiency of modern optical techniques have made it possible to perform Brillouin Scattering experiments with higher accuracy than was possible before (5, 6, 7).

The possibility of obtaining much more accurate experimental data has led to further refinement of the theory of light scattering. The original theories of light scattering from fluids were based on thermodynamics (1, 3, 8). The more recent approach is to treat the scattering process in terms of the intermolecular (or interatomic) properties of the medium. The spectrum of the scattered light is calculated in terms of the correlation functions of the transport coefficients of the fluid. Similar techniques have been applied to x-ray and Neutron scattering theories. The spectral distribution of the scattered light can be expressed in terms of the space-time correlation function of the particles in the system (to first order perturbation), and is given by (9, 10):

$$I(K,\omega) = |I_0|^2 \frac{\omega_0{}^4 N \sin^2 \psi}{32\pi^3 c^4 R^2} \left(\frac{\partial \varepsilon}{\partial \rho}\right)^2_{\rho=\rho_0}$$

$$\times \int\int [G(\bar{r}, t) - \rho_0] \, e^{i(\bar{K}.\bar{r} - \omega t)} \, d^3\bar{r}dt \qquad (1.9)$$

where $I_0$ and $\omega_0$ are the intensity and angular frequency of the incident light, R is the distance of the observer from the scattering volume containing N molecules, $\psi$ is the angle between the incident electric field vector and the scattering vector, $\varepsilon$ is the dielectric constant of the fluid. The space integration is taken over the scattering volume, which is smaller than the fluid volume to avoid surface effects. $G(\bar{r}, t)$ is the space-time correlation function, defined by Van Hove as (11):

$$G(\bar{r},t) = \frac{1}{N} < \sum_{ij}\sum \int d\bar{r}' . \delta(\bar{r}+\bar{r}_i(o) - \bar{r}') \delta(\bar{r}'-\bar{r}_j(t)) > \qquad (1.10)$$

The angular brackets $<....>$ indicate averaging over the ensemble. Physically the space-time correlation function $G(\bar{r}, t)$ is the probability that there will be a molecule at $\bar{r}$ at time t, given that there was a molecule at the origin at time zero.

Equation (1.9) is important since it shows the possibility of obtaining $G(\bar{r}, t)$ from the spectral density of the scattered light (10), in a similar way to that of obtaining the radial distribution function $g(\bar{r})$ from Neutron scattering experiments.

Writing the generalised structure factor $S(K,\omega)$ as:

$$S(K,\omega) = \int\int [G(\bar{r},t) - \rho_0] e^{i(\bar{K}.\bar{r} - \omega t)} d^3\bar{r}\, dt \qquad (1.11)$$

one can see that $G(\bar{r}, t)$ could be obtained by Fourier Inversion:

$$[G(\bar{r},t) - \rho_0] = (\frac{1}{2\pi})^3 \iint S(K,\omega) e^{-i(\bar{K}.\bar{r} - \omega t)} d\bar{K}\, d\omega \qquad (1.12)$$

Thus from (1.12) it is possible to interpret the kinetics of molecular motion in terms of the spectral density of the scattered light.

For light scattering in fluids, except for dilute gases, the wavelength of the sound waves observed is much longer than the correlation length of $G(\bar{r}, t)$ and one can use the long-time and large $\bar{r}$ limit of $G(\bar{r}, t)$. In this limit the from of $G(\bar{r}, t)$ reduces to the density-density auto correlation function (11):

$$G(\bar{r},t) = \frac{1}{N} \int \langle \rho(\bar{r}'-\bar{r}, o)\ \rho(\bar{r}',t) \rangle\, d^3r' \qquad (1.13)$$

where $\rho(\bar{r}, t)$ is the number density of the fluid particles. For dense fluids (liquids and gases at high pressures) the wavelengths of the thermal pressure waves (phonons) observed by light scattering are much greater than the intermolecular spacings or mean free paths of the molecules. This means that in these cases the time of decay of the fluctuations involved are much longer than the time intervals characteristic of molecular scattering processes. In this limit the decay of fluctuations of density can be adequately described by the equations of linearized hydrodynamics. Thus one can conclude that with light scattering one can probe the kinetics of microscopic fluctuations of macroscopic variables in dense fluids.

## 1.3. Simple Liquids

The derivation of an expression for the generalised structure factor, $S(K, \omega)$ for fluids using linearized hydrodynamic equations has been performed by many authors (12 - 16). The degree of sophistication of the resultant expression depends on the extent of the exactness carried out in the mathematical manipulations. The simplest treatment was given by Mountain (12) who obtained an expression showing that the spectrum of the scattered light consists of three lines, the central line and two shifted Brillouin lines all of Lorentzian shape for a simple liquid. More rigorous treatment shows that the shifted lines contain an asymmetric term, which makes the lineshape of the Brillouin lines asymmetric (12, 15). However, experimentally it is very difficult to distinguish the asymmetry introduced by this effect from the distortion of the spectrum in the process of detection. The observed spectrum is generally distorted by the overlapping of the tails of the central line on the Brillouin lines which produces an asymmetry in the observed Brillouin lineshape. The asymmetry introduced by this effect is of the same magnitude or even larger than the effect that would have been introduced by the calculated asymmetric term.

In a simple monatomic liquid such as liquid Argon there are no molecular internal degrees of freedom. Hence the damping processes which produce attenuation of the sound waves are connected with the kinetics of the atoms only, through the transport coefficients. The broadening of the Brillouin lines of the light scattered from such a system is

then due to the viscosity and thermal conductivity of the liquid. This enables one to determine the intrinsic bulk viscosity of the liquid from the sound attenuation coefficient. In the case of a molecular liquid energy exchange between external and internal degrees of freedom can also lead to additional broadening of the Brillouin lines. However, this work deals only with atomic liquids and this effect will not be discussed further.

Brillouin scattering experiments on liquid Argon in its normal liquid range has been performed by Fleury and Boon who reported a systematically lower sound velocity, compared with the data obtained from ultrasonic experiments, (17). However, the magnitude of this negative dispersion of the velocity of sound was within their experimental errors. Hence the presence of a negative dispersion in the sound velocity in liquid Argon at hypersonic frequencies (~3GHz) could not be established from their results.

In this work we have observed Brillouin scattering in liquid Argon and liquid Krypton along their saturated vapour pressure curves from near their triple points to near their critical points. The measurements were made at various scattering angles, $\theta$: $13^{\circ}35'$, $102^{\circ}47'$ and $169^{\circ}51'$ in liquid Argon and $93^{\circ}48'$ and $169^{\circ}20'$ in liquid Krypton. The measured sound velocities obtained from the different scattering angles in each liquid were compared with each other to establish the internal consistency of the measurement and also compared with those obtained from ultrasonic methods. In this way we were able to make a wider comparison of the data

to establish whether there is any dispersion of the sound velocity in these liquids, since these data cover a large range of frequencies. Within the limits of experimental error the data showed no systematic dispersion. We also made use of a high resolution spherical Fabry-Perot (FPS) interferometer to determine the Brillouin linewidths of the light scattered in the backward direction in these liquids: $\theta = 169^{\circ}51'$ in liquid Argon and $\theta = 169^{\circ}20'$ in liquid Krypton. Measurements of the sound attenuation coefficient in liquid Argon by ultrasonic methods have been reported by Naugle (18) and Cowan (19). Our results obtained by light scattering agree with the ultrasonic results within experimental accuracy. There is no prior measurement of sound attenuation coefficient in liquid Krypton (to the author's knowledge) either by ultrasonic or light scattering method.

## 1.4. Binary Monatomic Gas Mixture

The theoretical investigation of the form of the spectral density of light scattered from a multicomponent system via the generalised structure factor, $S(K, \omega)$ has been carried out by several authors (20 - 24). For a binary mixture these investigations have been performed for both the kinetic regime and the hydrodynamic regime. In this work we restrict ourselves to the latter case.

In a binary gaseous mixture, especially when the molecular (or atomic) masses of the components are very different the sound waves are damped not only through overcoming

viscous forces and energy loss by heat conduction but also by mass diffusion through the system. This is because pressure gradients produced by the sound waves in the system give rise to different molecular velocities of the components, i.e. the molecular velocity of the lighter component will be greater than that of the heavier component. Hydrodynamic fluctuation theory predicts for such a system that the linewidths of the central line and the Brillouin lines should contain additional contributions from the mutual diffusion coefficient of the mixture:

$$\Gamma_C = \Gamma(\lambda) + \Gamma(D) \tag{1.14}$$

and

$$\Gamma_B = \Gamma(\eta) + \Gamma(\lambda) + \Gamma(D) \tag{1.15}$$

where $\Gamma_C$ and $\Gamma_B$ are the line widths of the central line and Brillouin lines respectively, and $\Gamma(\eta)$, $\Gamma(\lambda)$ and $\Gamma(D)$ are the contributions to the linewidths due to transport coefficients: viscosity, thermal conductivity and mutual diffusion coefficient respectively .

Thus it is possible to determine the mutual diffusion coefficient of a binary mixture from the measurement of the linewidths of the scattered light. The accuracy of the measurement is enhanced in cases where the contribution to the Brillouin linewidth from the viscosity and thermal conductivity is much smaller than the contribution due to diffusion (25).

In this work we have observed Brillouin scattering from

the binary monatomic gas mixtures Argon-Neon and Krypton-Helium. These two mixtures have component mass ratios of approximately 2:1 and 20:1. The mutual diffusion coefficient of a binary gaseous mixture is inversely proportional to the reduced atomic mass of the mixture, hence the diffusion effect would be expected to be more prominent in the Krypton-Helium mixture.

The experiments on the Argon-Neon mixture were carried out at various concentrations (Neon concentration C = 0 - 0.3) at one scattering angle only. Thus we have investigated the sound velocity in this mixture as a function of concentration. The experiments on the Krypton-Helium mixture were done at a much lower concentration range (Helium concentration C = 0 - 0.03) and at different scattering angles at a single concentration (0.01). This has enabled us to investigate the sound velocity as a function of concentration as well as the dependence of the sound velocity on the scattering vector (i.e. the dispersion of the sound velocity) in this mixture.

Previous light scattering experiments on a binary gas mixture in the hydrod ynamic region has been done by Gornal, et al. (26) who reported a lowering of the observed sound velocity in the mixture Helium-Sulfur Hexafluoride from the adiabatic sound velocity. Clarke (27) has investigated the system Helium-Xenon in the kinetic region and investigated the correctness of the solution to the Boltzman Equation.

## 1.5. Summary

From the above we see that Brillouin scattering, applied to fluids, provides a means of measuring:

(a) the velocity of high frequency sound waves in the medium from the Brillouin shifts,

(b) the compressibilities of the medium, calculated from the ratio of the intensities of the scattered light,

(c) the sound attenuation coefficient, and hence, the transport coefficients of the medium; obtained from the Brillouin linewidths.

(d) Applied to a mixture, the measurement of the linewidths could yield information on the mutual diffusion coefficient of the mixture.

The contributions of this work may be summarised as follows:

A. In the simple monatomic liquids:

(1) we have determined the hypersonic sound velocity in liquid Argon and liquid Krypton along their saturated vapour pressure curves, at different scattering vectors.

(2) Within the accuracy of our experiments we have verified that there is no dispersion of sound velocity in these liquids.

(3) We have measured the sound attenuation coefficient and hence deduced the bulk viscosity in these liquids as a function of temperature.

B. In the Binary Gaseous Mixtures:

(1) we have attempted to investigate the sound velocity as a function of the concentration in the mixtures Argon-Neon and Krypton-Helium.

(2) We have investigated the dependence of the sound velocity and attenuation on the scattering vector in the binary mixture Krypton-Helium.

References in Chapter I

(1) L. Brillouin; Ann. Phys. 17 88 (1922)

(2) E. Gross; Nature 126 201 (1930)

(3) L. Landau, G. Placzek; Z. Phys. Sowjet Union 5 172 (1934)

(4) L. Landau, S. Lifshitz; 'Fluid Mechanics' Addison Wesley Publishing Company (1959)

(5) D.H. Rank; J. Acoust. Soc. Amer. 49 937 (1971)

(6) D.I. Mash, V.S. Starunov, I.L. Fabelinskii; Soviet Phys. - JETP 20 523 (1965)

(7) D.I. Mash, V.S. Starunov, E.V. Tiganov, I.L. Fabelinskii; Soviet Phys. - JETP 22 1205 (1966)

(8) G.P. Mutalevich, I.L. Fabelinskii; Soviet Phys. Doklady 1 81 (1956)

(9) R. Pecora; J. Chem. Phys. 40 1604 (1964)

(10) L.I. Kamarov, I.Z. Fisher; Soviet Phys. - JETP 16 1358 (1963)

(11) L. Van Hove; Phys. Rev. 95 249 (1954)

(12) R.D. Mountain; Rev. Mod. Phys. 38 205 (1966)

(13) C.J. Montrose, V.A. Solovyev, T.A. Litovitz; J. Acous. Soc. Amer. 43 117 (1968)

(14) A.B. Bhatia, E. Tong; Phys. Rev. 173 231 (1968)

(15) P.A. Selwyn, I. Oppenheim; Physica 54 195 (1971)

(16) J.E. Piercy, G.R. Hanes; J. Acous. Soc. Amer. 49 1001 (1971)

(17) P.A. Fleury, J.P. Boon; Phys. Rev. 186 224 (1969)

(18) D.G. Naugle; J. Chem. Phys. 44 741 (1966)

(19) R.N. Ball, J.A. Cowen; Phys. Can. 27 68 (1971)

(20) L. Blum; J. Chem. Phys. 50 17 (1969)

(21) R.D. Mountain, J.M. Deutch; J. Chem. Phys. 50 1103 (1969)

(22) H.N.W. Lekkerkerker , J.P. Boon; Phys. Lett. 39A 9 (1972)

(23) C. Cohen, J.W.H. Sutherland, J.M. Deutch; Phys. Chem. Liquids 2 213 (1971)

(24) H.N.W. Lekkerkerker , W.G. Laidlaw; Phys. Chem. Liquids 3 175 (1972)

(25) I.M. Arefev; JETP Lett. 10 340 (1969)

(26) W.S. Gornal, C.S. Wang, C.C. Yang, N. Bloembergen; Phys. Rev. Lett. 26 1094 (1971)

(27) N.A. Clarke; Ph.D. Thesis, Massachusetts Institute of Technology, 1970.

# CHAPTER II

# LIGHT SCATTERING IN A PURE MONATOMIC LIQUID

## 2.1. Introduction

In this chapter an outline of the theory of light scattering from isotropic continuous media is given. By using the classical theory of scattering of radiation we show that the spectrum of the scattered light is determined by the generalised structure factor $S_{\varepsilon}(K, \omega)$, the Fourier-Laplace transform of fluctuations in the local dielectric constant of the medium. The generalised structure factor is then expressed in terms of the density- density correlation function which is derived using the linearized hydrodynamic equations and statistical irreversible thermodynamics for a one component monatomic liquid.

## 2.2. Light Scattering in Continuous Isotropic Media

The spectrum of the scattered light from a continuous medium may be calculated using the equations of hydrodynamics and classical irreversible thermodynamics (1). A medium can be assumed to be continuous if the intermolecular distances or the mean free paths of the molecules are smaller than the wavelength of the incident radiation in the medium. Such an assumption is valid when applied to liquids and moderately high pressure gases.

The medium can be characterised by an equilibrium dielectric constant $\varepsilon_0$. Thermal motion of the molecules in the medium gives rise to fluctuations in the local

dielectric constant, $\Delta\varepsilon$. The scattering of light from a continuous isotropic medium arises from these local inhomogeneities in the dielectric constant. Generally the fluctuations in the dielectric constant are position- and time-dependent. Thus we can represent the dielectric constant of the medium as:

$$\varepsilon(\bar{r}, t) = \varepsilon_0 + \Delta\varepsilon(\bar{r}, t) \qquad (2.1)$$

It is assumed that the fluctuations $\Delta\varepsilon(\bar{r}, t)$ are small compared with the equilibrium dielectric constant $\varepsilon_0$. The homogeneous equilibrium term in (2.1) does not contribute to the scattering of light (except in the forward direction), so we can restrict our discussion on the fluctuations $\Delta\varepsilon(\bar{r}, t)$ only.

The fluctuations in the dielectric constant may be expressed in terms of fluctuations in the mutually independent thermodynamic variables of the system such as pressure, $\Delta P$ and entropy, $\Delta S$; or density, $\Delta\rho$ and temperature, $\Delta T$ (2). In the case of mixtures or solutions fluctuations in the concentration, $\Delta C$ also contribute to $\Delta\varepsilon$ (3).

The experimental situation in a light scattering experiment is depicted in Figure (2.1). The system is illuminated with a plane polarized monochromatic electromagnetic wave with wave vector $\bar{k}$ and frequency $\omega/2\pi$ Hz in the medium. The plane of polarization of the incident electric field is along the z-axis. The scattered

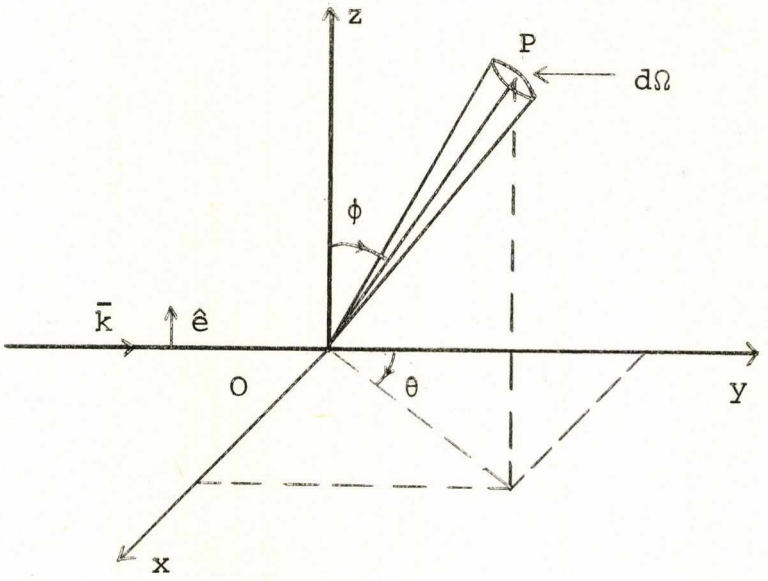


Figure 2.1: Experimental Scattering Geometry

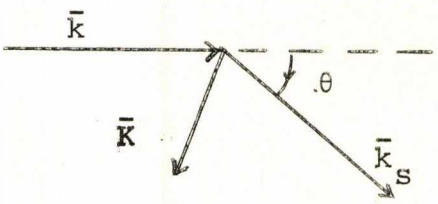


Figure 2.2: Momentum Vector diagram of scattering process, θ is the scattering angle

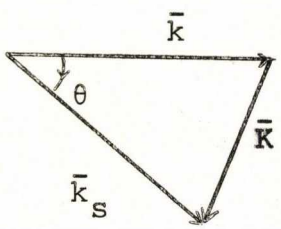


Figure 2.3: Momentum Conservation diagram. $k \simeq k_s$

field intensity is detected and its frequency analysed at a point P on a radius vector $\bar{R}$ at an angle $\theta$ to the direction of the incident wave vector $\bar{k}$. The detector has a collection solid angle $d\Omega$.

The incident electric field can be represented by

$$\bar{E}_0(\bar{r}, t) = \hat{e}E_0 e^{-i(\bar{k}\cdot\bar{r} - \omega t)} \qquad (2.2)$$

where $\hat{e}$ is a unit vector along the direction of polarization of the electric field and $E_0$ is the amplitude of the field.

To evaluate the field at the detector point P we consider a volume element v in the scattering region, at a distance $\bar{r}'$ from an arbitrary (but fixed) origin within the scattering volume. The scattering geometry is depicted in Figure (2.2). The incident radiation induces a radiating dipole moment $\bar{p}(\bar{r}', t)$ in the volume element, which gives rise to scattered light. In terms of the fluctuations in the dielectric constant $\Delta\varepsilon(\bar{r}', t)$ and the incident electric field this induced dipole moment is given by:

$$\bar{p}(\bar{r}', t) = \Delta\varepsilon(\bar{r}', t)\, E_0(\bar{r}', t) \qquad (2.3)$$

per unit volume.

Assuming the change in frequency between the incident light and the scattered light is small, the field at P can be represented by:

$$\bar{E}(\bar{R},\ t) = E'(\bar{r}')e^{i(\bar{k}_s\cdot\bar{r}' - \omega t)} \qquad (2.4)$$

where $E'(\bar{r}')$ is the amplitude of the field radiated by the induced dipole moment of the volume element v, and is given by (4):

$$E'(\bar{r}') = \frac{e^{i\bar{k}_s\cdot\bar{R}}}{4\pi\varepsilon_v R}\left[(\bar{p}(\bar{r}',\ t)\cdot\frac{\varepsilon_v}{\varepsilon_0}\times\bar{k}_s)\times\bar{k}_s\right] \qquad (2.5)$$

$\varepsilon_v$ is the vacuum permitivity. $\bar{p}(\bar{r}',\ t)$ is reduced by $\frac{\varepsilon_v}{\varepsilon_0}$ since it is surrounded by the medium with dielectric constant $\varepsilon_0$.

Since the medium is isotropic the direction of $\bar{p}(\bar{r}',\ t)$ is along the direction of the polarization of the incident electric field (i.e. the z-axis). Thus we have:

$$E'(\bar{r}') = \frac{-k_s^2 e^{i\bar{k}_s\cdot\bar{R}}}{4\pi\varepsilon_0 R}\sin(\phi)\,\bar{p}(\bar{r}',\ t) \qquad (2.6)$$

where $\phi$ is the angle that the radiation vector $\bar{R}$ makes with the direction of polarization of the incident field (refer to Figure 2.1). In our experiments the detector is in the scattering plane and $\phi = 90^{\circ}$.

The scattered field at the detector point P due to the volume element v is then, from (2.6), (2.3) and (2.2):

$$\bar{E}(\bar{R},\ t) = -\frac{k_s^2 e^{i\bar{k}_s\cdot\bar{R}}}{4\pi\varepsilon_0 R}\sin(\phi)\,\Delta\varepsilon(\bar{r}',\ t)E_0 e^{-i\left[(\bar{k}_s-\bar{k})\cdot\bar{r}' - \omega t\right]} \qquad (2.7)$$

From the scattering geometry shown in Figure (2.2) we see that:

$$\bar{k}_s - \bar{k} = \bar{K} \qquad (2.8)$$

where $\bar{K}$ is the scattering vector.

Since the frequency shifts involved are small we have $\bar{k}_s \simeq \bar{k}$. The magnitude of $\bar{K}$ can be seen from Figure (2.3) to be:

$$|K| = 2|k| \sin(\theta/2) \qquad (2.9)$$

where $\theta$ is the scattering angle.

The scattering process can thus be characterised by the scattering vector $\bar{K}$ and the scattered field (2.7) becomes:

$$\bar{E}(\bar{R}, t) = \frac{E_0 k^2 e^{i\bar{k}_s \cdot \bar{R}}}{4\pi\varepsilon_0 R} \sin(\phi) \Delta\varepsilon(\bar{r}', t) e^{-i(\bar{K} \cdot \bar{r}' - \omega t)} \qquad (2.10)$$

Integrating (2.10) over the scattering volume (over all $\bar{r}'$) we get:

$$\bar{E}(\bar{R}, t) = - \frac{E_0 k^2 e^{i\bar{k}_s \cdot \bar{R}}}{4\pi\varepsilon_0 R} \sin(\phi) e^{i\omega t} \int \Delta\varepsilon(\bar{r}', t) e^{-i\bar{K} \cdot \bar{r}'} d^3\bar{r}' \qquad (2.11)$$

The integration is taken over the scattering volume which is much smaller than the volume of the bulk medium. However, the scattering volume is much larger than intermolecular parameters and the limits of integration can be taken to be infinity. Hence we can recognise that the

integral is the $\bar{K}$th Fourier component of $\Delta\varepsilon(\bar{r}', t)$, defined as:

$$\Delta\varepsilon(\bar{K}, t) = \int e^{-i\bar{K}\cdot\bar{r}}\, \Delta\varepsilon(\bar{r}, t)\, d\bar{r} \qquad (2.12)$$

and with this definition the scattered field can then be written as:

$$E(\bar{K}, t) = -\frac{E_0 k^2 e^{i\bar{k}_s\cdot\bar{R}}}{4\pi\varepsilon_0 R} \sin(\phi)\, e^{i\omega t}\, \Delta\varepsilon(\bar{K}, t) \qquad (2.13)$$

which can be regarded as the Kth Fourier component of the scattered field.

## 2.3. The Spectrum of the Scattered Field

In order to obtain the spectral power density (power spectrum) of the scattered field $E(\bar{K}, t)$ we form the field correlation function, $\langle E(\bar{K}, t)\cdot E^*(\bar{K}, t+\tau)\rangle$. The field correlation function is the ensemble average of the product of $E(\bar{K}, t)$ and $E^*(\bar{K}, t+\tau)$ of similar samples. Since the system we are investigating is in equilibrium, the fluctuations $E(\bar{K}, t)$ form a stationary random process; and the field correlation function will be independent of the starting time t. Thus we can define the correlation function $C_E(\tau)$ as:

$$C_E(\tau) = \langle E(\bar{K}, t)\cdot E^*(\bar{K}, t+\tau)\rangle$$

$$= \langle E(\bar{K}, 0)\cdot E^*(\bar{K}, \tau)\rangle \qquad (2.14)$$

Putting (2.13) in (2.14) we then have the correlation function for the scattered field as:

$$C_E(\tau) = \frac{|E_0|^2 k^4 \sin^2(\phi)}{16\pi^2 \varepsilon_0^2 R^2} <\Delta\varepsilon(\bar{K}, 0) . \Delta\varepsilon^*(\bar{K}, \tau)> \qquad (2.15)$$

The quantity that is measured in a light scattering experiment is the spectral power distribution of the scattered field. The power spectrum $S(K, \omega)$ of a correlation function $C(\tau)$ is given by the Wiener-Khintchine theorem and defined as (5):

$$S(K, \omega) = \int_{-\infty}^{\infty} e^{-i\omega\tau} C(\tau) d\tau \qquad (2.16)$$

From (2.15) and (2.16) we obtain the power spectrum of the scattered field as:

$$S_E(K, \omega) = \frac{|E_0|^2 k^4 \sin^2(\phi)}{16\pi^2 \varepsilon_0^2 R^2} \int_{-\infty}^{\infty} e^{-i\omega\tau} <\Delta\varepsilon(\bar{K}, 0) . \Delta\varepsilon^*(\bar{K}, \tau) d\tau \qquad (2.17)$$

Thus the intensity distribution $I(\omega)$ of the scattered light at the scattering vector $\bar{K}$ is given by:

$$I(\omega) = \frac{k^4}{16\pi^2 \varepsilon_0^2 R^2} I_0 \sin^2(\phi) S_\varepsilon(K, \omega) \qquad (2.18)$$

where $I_0$ is the incident intensity and we have defined

$$S_\varepsilon(K, \omega) \equiv \int_{-\infty}^{\infty} e^{-i\omega\tau} <\Delta\varepsilon(K, 0) . \Delta\varepsilon^*(K, \tau)> d\tau \qquad (2.19)$$

$S_\varepsilon(K, \omega)$* is the double Fourier transform of the space-time correlation function of fluctuations in the dielectric constant $\Delta\varepsilon(\bar{r}, t)$.

## 2.4. Pure Monatomic Liquid

The fluctuations in the dielectric constant in a one component fluid can be expressed in terms of fluctuations in the local thermodynamic variables of the system. In this section we outline the method of obtaining the spectrum of light scattered from a pure monatomic liquid, using this assumption. This procedure is essentially the same as that adopted by Mountain (6) for a general fluid.

The dielectric constant is assumed to be a function of the density $\rho$ and the temperature T. We can then represent the fluctuations in the dielectric constant $\Delta\varepsilon(\bar{r}, t)$ by:

$$\Delta\varepsilon(\bar{r}, t) = \left(\frac{\partial\varepsilon}{\partial\rho}\right)_T \Delta\rho(\bar{r}, t) + \left(\frac{\partial\varepsilon}{\partial T}\right)_\rho \Delta T(\bar{r}, t) \qquad (2.20)$$

---

* Since the fluctuations form a stationary random process the correlation function $C(\tau)$ is even in $\tau$. Thus, as normally written in the literature, we can write,

$$S_\varepsilon(K, \omega) = 2\mathrm{Re} \int_0^\infty d\tau\, e^{-i\omega\tau} \langle \Delta\varepsilon(K, 0)\, \Delta\varepsilon(K, \tau) \rangle .$$

Generally in a monatomic liquid $(\frac{\partial \varepsilon}{\partial T})_{\rho}$ is very small and the second term in (2.20) can be neglected without giving rise to serious errors. In the following discussions we will not include this term.

In accordance with equation (2.12) we can write the Kth Fourier component of the fluctuations in the dielectric constant as:

$$\Delta\varepsilon(K, t) = (\frac{\partial \varepsilon}{\partial \rho})_T \int e^{-i\bar{K}\cdot\bar{r}} \Delta\rho(\bar{r}, t)\, d^3\bar{r}$$

$$= (\frac{\partial \varepsilon}{\partial \rho})_T \Delta\rho(K, t) \qquad (2.21)$$

where we have written:

$$\Delta\rho(K, t) = \int e^{-i\bar{K}\cdot\bar{r}} \Delta\rho(\bar{r}, t)\, d^3\bar{r} \qquad (2.22)$$

The correlation function of the fluctuations in the dielectric constant can then be written as:

$$C_{\varepsilon}(\tau) = (\frac{\partial \varepsilon}{\partial \rho})_T^2 \langle \Delta\rho\ (K, 0) \cdot \Delta\rho^*(K, \tau) \rangle \qquad (2.23)$$

The averaging operation in (2.23) is equivalent to two ensemble averages. First we obtain the conditional ensemble average $\langle \Delta\rho^*(K, \tau) \rangle$ of the values which $\Delta\rho^*(K, \tau)$ can have at time $\tau$, given that it had some original value $\Delta\rho^*(K, 0)$. Secondly we obtain the final ensemble average of

the weighted products $\Delta\rho(K, 0)\Delta\rho^*(K, \tau)$ and all possible values of $\Delta\rho(K, 0)$ for a given $\bar{K}$.

The conditional average $<\Delta\rho^*(K, \tau)>$ may be obtained from the equations of motion of the fluctuations. In the long wavelength and small $\bar{K}$ limit, i.e. where the time of decay of the fluctuation is much greater than the time-scales of molecular collision, the hydrodynamic equations, for given initial conditions, have been shown to adequately provide the conditional ensemble average (7, 8).

We define the local state variables of the system by:

$$\bar{A}(\bar{r}, t) = \{\rho_1(\bar{r}, t), T_1(\bar{r}, t), \bar{v}(\bar{r}, t)\} \qquad (2.24)$$

The curley brackets indicate a column vector. The local state variables are defined as

$$\rho_1(\bar{r}, t) = \rho(\bar{r}, t) - \rho_0 \qquad (2.25)$$

and

$$T_1(\bar{r}, t) = T(\bar{r}, t) - T_0 \qquad (2.26)$$

$\rho_0$ and $T_0$ being the equilibrium values and $\rho_1(\bar{r}, t)$ and $T_1(\bar{r}, t)$ are the fluctuations, which are assumed small, i.e.

$$\rho_1(\bar{r}, t) << \rho_0$$

and

$$T_1(\bar{r}, t) << T_0$$

The average velocity field is assumed to be zero.

The assumption of small fluctuations makes it possible to linearize the hydrodynamic equations and it also implies that the transverse component of the velocity $\bar{v}(\bar{r}, t)$ is uncoupled to the sound mode (9). The linearized hydrodynamic equations for the system are (9):
the continuity equation:

$$\frac{\partial \rho_1}{\partial t} + \rho_0 \nabla \cdot \bar{v} = 0 \qquad (2.27)$$

the longitudinal part of the Narier-Stokes equation:

$$\rho_0 \frac{\partial \bar{v}}{\partial t} + \frac{C_0^2}{\gamma} \nabla \rho_1 + \frac{C_0^2 \beta_T \rho_0}{\gamma} \nabla T_1 - (\frac{4}{3} \eta_s + \eta_B) \nabla(\nabla \cdot \bar{v}) = 0 \qquad (2.28)$$

and the energy transport equation:

$$\rho_0 C_v \frac{\partial T_1}{\partial t} - \frac{C_v(\gamma-1)}{\beta_T} \frac{\partial \rho_1}{\partial t} - \lambda \nabla^2 T_1 = 0 \qquad (2.29)$$

In the above equations we have used the symbols:

$C_v$: the specific heat at constant volume,

$C_0$: the low frequency limit of the adiabatic sound velocity,

$\gamma$ : the ratio of the specific heat at constant pressure to the specific heat at constant volume = $C_p/C_v$,

$\eta_s, \eta_B$ : the shear and bulk viscosities ,

$\lambda$ : the termal conductivity.

Taking the divergence of (2.28) and substituting $\nabla \cdot \bar{v}$ from (2.27) we are left with two coupled equations:

$$\frac{\partial^2 \rho_1}{\partial t^2} - \frac{C_0^2}{\gamma}\frac{\partial^2 \rho_1}{\partial x^2} - \frac{C_0^2 \beta_T \rho_0}{\gamma}\frac{\partial^2 T_1}{\partial x^2}$$

$$- \left(\frac{4}{3}\eta_s + \eta_B\right)\frac{1}{\rho_0}\frac{\partial^2}{\partial x^2}\frac{\partial \rho_1}{\partial t} = 0 \qquad (2.30)$$

and

$$\rho_0 C_v \frac{\partial T_1}{\partial t} - \frac{C_0(\gamma-1)}{\beta_T}\frac{\partial \rho_1}{\partial t} - \lambda \frac{\partial^2 T_1}{\partial x^2} = 0 \qquad (2.31)$$

Following the method adopted by Mountain (6) we solve the equations by performing a Laplace transformation on the time coordinate and a Fourier transformation on the spatial coordinate of equations (2.30) and (2.31). Assuming the statistical independence of the fluctuations of the density with its derivative and with the fluctuations of the temperature we obtain the Laplace transform of the Fourier transform of the density fluctuation, $\rho_1(K, s)$ in terms of the initial condition $\rho_1(K, 0)$ as:

$$\rho_1(K,s) = \rho_1(K, 0)\,\frac{s^2+(a+b)K^2 s+abK^4 + C_0^2\left(1-\frac{1}{\gamma}\right)K^2}{s^3+(a+b)K^2 s^2 + (C_0^2K^2+abK^4)s+\frac{aC_0^2}{\gamma}K^4} \qquad (2.32)$$

where

$$\left.\begin{aligned} \rho_1(K,s) &= \int_{-\infty}^{\infty} d\bar{r} \int_0^{\infty} dt\; e^{-i\bar{K}\cdot\bar{r}}\, e^{-st}\, \rho_1(\bar{r}, t) \\ \rho_1(K,0) &= \int d\bar{r}\; e^{-i\bar{K}\cdot\bar{r}}\, \rho_1(\bar{r}, 0) \\ s &= i\omega \end{aligned}\right\} \qquad (2.33)$$

and we have written

$$a = \lambda/\rho_0 C_v \tag{2.34}$$

$$b = (\tfrac{4}{3}\eta_s + \eta_B)/\rho_0 \tag{2.35}$$

To obtain the inverse Laplace transform of $\rho_1(K, s)$ we have to find the roots of the denominator of (2.32), hence the solutions of the dispersion equation:

$$D(s) = s^3+(a+b)K^2s^2+(C_0{}^2K^2+abK^4)s+ \frac{aC_0{}^2}{\gamma} K^4 = 0 \tag{2.36}$$

Even though it is possible to solve (2.36) algebraically, it is not very convenient to do so because of its complexity. Here we consider approximate solutions of $D(s) = 0$ based on the experimental fact that for liquids $aK^2 << C_0K$ and $bK^2 << C_0K$. Thus we can solve $D(s) = 0$ in terms of a power series of $aK^2/C_0K$ and $bK^2/C_0K$. To the lowest order in $aK^2$ and $bK^2$ the solutions are found to be (6, 10):

$$\left.\begin{aligned} s &= \pm iC_0K - \tfrac{1}{2}(a + b - \frac{a}{\gamma}) K^2 \\ \text{and} \\ s &= -(a/\gamma)K^2 \end{aligned}\right\} \tag{2.37}$$

We write:

$$\omega_0 \equiv C_0K \tag{2.38}$$

$$\Gamma_B \equiv \tfrac{1}{2}(a + b - \frac{a}{\gamma})\ K^2 \qquad (2.39)$$

$$\Gamma_C \equiv (a/\gamma)\ K^2 \qquad (2.40)$$

In terms of the original parameters (2.39) and (2.40) are:

$$\Gamma_B \equiv \frac{1}{2\rho_0}\left[(\frac{4}{3}\eta_s + \eta_B) + \lambda(\gamma-1)/C_p\right] K^2 \qquad (2.41)$$

and

$$\Gamma_C \equiv \lambda/\rho_0 C_p\ K^2 \qquad (2.41)$$

which are the values obtained by Landau and Placzek (1.5 , 8)

Using the solutions (2.37) and the definitions (2.38 - 40) we find the lowest order term of the inverse Laplace transform of $\rho_1(K, s)$ or the Kth Fourier component of the fluctuation $\rho_1(\bar{r}, t)$ as: (11)

$$\rho_1(K, t) = \rho_1(K, 0)\left\{(1 - \frac{1}{\gamma})\exp(-\Gamma_C t) + \frac{1}{\gamma}\left[e^{-\Gamma_B t}\cos(\omega_0 t) + \frac{(3\Gamma_B - bK^2)}{\omega_0} e^{-\Gamma_B t}\sin(\omega_0 t)\right]\right\} \qquad (2.42)$$

The Kth component of the density- density correlation function is then:

$$C_\rho(K,t) = \langle\rho_1(K,0)\ \rho_1(K,t)\rangle$$

$$= \langle\rho_1(K)\ \rho_1(K)\rangle\left\{(1-\frac{1}{\gamma})\ e^{-\Gamma_C t} + \frac{1}{\gamma}\left[e^{-\Gamma_B t}\cos(\omega_0 t) + \frac{(3\Gamma_B - bK^2)}{\omega_0} e^{-\Gamma_B t}\sin(\omega_0 t)\right]\right\} \qquad (2.43)$$

Applying the definition (2.16) to (2.43) we obtain the generalized structure factor $S_\rho(K, \omega)$:

$$S_\rho(K, \omega) = < \rho_1(K)\ \rho_1(K) > \left\{(1-\frac{1}{\gamma})\ \frac{2\Gamma_C}{(\Gamma_C)^2 + \omega^2}\right.$$

$$+ \frac{\Gamma_B/\gamma}{(\Gamma_B)^2 + (\omega + \omega_0)^2} + \frac{\Gamma_B/\gamma}{(\Gamma_B)^2 + (\omega - \omega_0)^2}$$

$$\left. + \frac{(3\Gamma_B - bK^2)}{\gamma\omega_0}\left[\frac{\omega+\omega_0}{(\Gamma_B)^2+(\omega+\omega_0)^2} - \frac{\omega-\omega_0}{(\Gamma_B)^2+(\omega-\omega_0)^2}\right]\right\} \qquad (2.44)$$

From statistical thermodynamic fluctuation theory, for a Gaussian probability distribution of fluctuations, we have the result (2):

$$<\rho_1(K)\rho_1(K)> = \rho_0^2 k_B T \beta_T \qquad (2.45)$$

per unit volume, where $k_B$ is the Boltzman constant and $\beta_T$ is the isothermal compressibility.

The first term on the right-hand side of (2.44) is the unshifted central line, indicating a non-propagating mode which has a linewidth (half width at half height) of $\Gamma_C$, which is proportional to the thermal diffusivity $a = \lambda/\rho_0 C_p$. This mode arises from density fluctuations which relax through heat conduction. The two shifted (Brillouin) lines contain two terms, a Lorentzian term centered at $\omega = \pm\omega_0$ and an asymmetric term with zero cross-over points at $\omega = \pm\omega_0$. These shifted lines represent

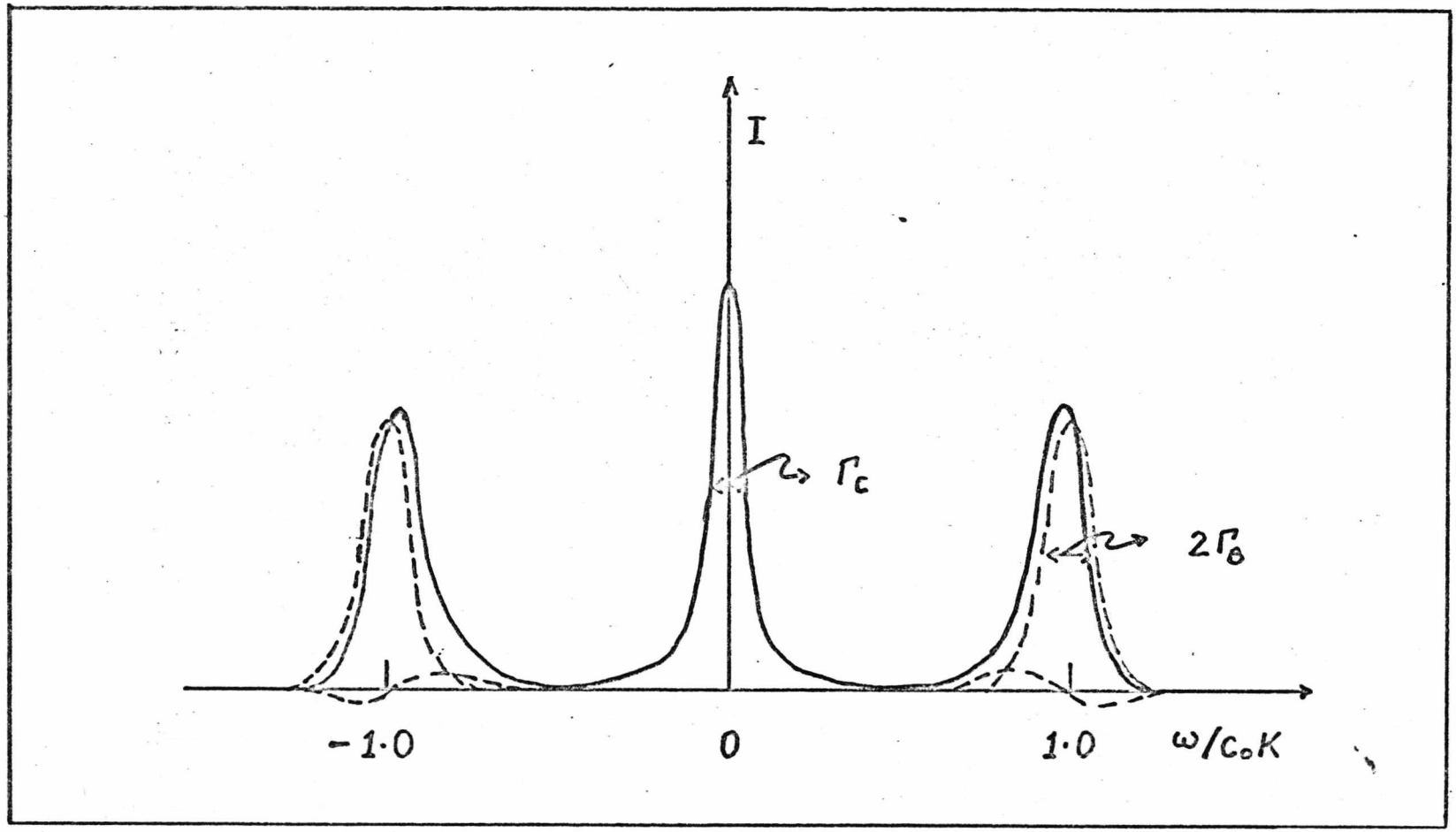


Figure 2.4: Schematic diagram of the spectrum of light scattered from a pure monatomic liquid showing the important components.

thermally driven propagating density fluctuation modes which are the damped acoustic modes. There are two of these because there are waves travelling in opposite directions with the same magnitude of wave vector. The frequency shift $\omega_0 = KC_0$ is the frequency of the adiabatic sound waves of wave vector $\bar{K}$. The effect of the asymmetric term is to shift the peak of the shifted lines towards the lower frequency side and in making the shape of the Brillouin lines asymmetric (12). Consequently the tail of the Brillouin lines on the high-frequency side falls more sharply than that on the low-frequency side. However, the magnitude of the asymmetric term is very small and its effect on the line shape is equally small. Further, the integral of the asymmetric term vanishes and the ratio of intensities of the central line to the Brillouin lines, $I_C/2I_B = \gamma-1$, giving the Landau-Placzek result. Figure (2.4) shows schematically the different contributions of the terms in equation (2.44) to the spectrum of the scattered light.

## 2.5. Dispersion of Sound Velocity in a Simple Fluid

The equations of hydrodynamics describe the low frequency and small wave vector limit of fluctuations in a fluid adequately. In this limit the fluctuations in a fluid are collision dominated, thus the effects that are described by hydrodynamics are the collective effects of intermolecular collisions. At frequencies approaching the

reciprocal collision time of the molecules and at wavelenghts approaching the intermolecular distances, the fluid can no longer be regarded as a continuum. The phenomena in this region have to be looked at in terms of the kinetics of the molecules. This region is usually described as the transition region between the hydrodynamic and kinetic region. Thus the hydrodynamic region can be described by:

$$\lim \omega = 0 , \quad \lim K = 0 \tag{2.46}$$

and the transition region can be described as the region:

$$\omega/\omega_c \sim 1 , \quad K/K_c \sim 1 \tag{2.47}$$

where $\omega_c$ is the characteristic frequency, of the order of the reciprocal collision time and $K_c^{-1}$ is the characteristic wavelength which is of the order of the intermolecular distance.

In a monatomic liquid such as liquid Argon the characteristic frequency is of the order of $10^{12}$ Hz and the characteristic wavelength is of the order of $10^{-8}$ cm; i.e. the characteristic wave vector, $K_c$ is of the order of $10^{8}$ $cm^{-1}$. Molecular dynamics calculations ('experiments') (13) and neutron scattering data (14) show a point of inflection in the $\omega(K)$ curve for a value of K of the order of $K_c$. This tends to infer the presence of relaxation processes in this region.

In light scattering experiments the frequencies observed (the Brillouin frequency shifts) are of the order of $10^{10}$ Hz and the wave vector K is of the order of $10^{5}$ $cm^{-1}$. Hence this region, characterised by $\omega/\omega_c \simeq 10^{-2}$ and $K/K_c \simeq 10^{-3}$, can be regarded as an intermediate region. Although this is still far away from the transition region it is expected that the effects of relaxation processes would begin to be observed, i.e. in this region the transport coefficients of the liquid, namely the diffusion coefficient, the viscosity and the thermal conductivity would be expected to show a small but finite frequency dependence.

Theoretical calculations by Boon and Deguent (15) in which frequency dependent transport functions from the generalised Berne-Boon-Rice model (16) are substituted in place of the constant transport functions in the linearized hydrodynamic equations produces a modification in the spectrum of the scattered light. The modification, however, is only a second order effect. In particular Boon and Deguent found the first order solutions to the dispersion equation (2.36) as:

$$s = \pm iC_0K(1 - \delta_2) - \Gamma_B(1 - \delta_3)$$

and (2.48)

$$s = -\Gamma_C(1 - \delta_1)$$

where $C_0$ $\Gamma_B$ and $\Gamma_C$ are the same as described before; and $\delta_1$, $\delta_2$ and $\delta_3$ are the first order corrections which

arise because of the introduction of the frequency dependence of the transport coefficients. Applied to liquid Argon, Boon and Deguent have shown these calculations to obtain the results:

(a) the hypersonic velocity at $\omega \sim 3\times10^{10}$ Hz

$$v_s = C_0(1 - 3\times10^{-5}) \tag{2.49}$$

where $C_0$ is the low frequency sound velocity.

(b) the lineshape of the Brillouin lines depart from the Lorentzian shape and the width of these lines is modified to the extent

$$(\Delta\omega_B - \Delta\omega_B{}^o)/\ \Delta\omega_B{}^o \simeq \pm\tfrac{1}{2}\% \tag{2.50}$$

where $\Delta\omega_B$ and $\Delta\omega_B{}^o$ are the high-frequency and low-frequency limit of the half widths respectively.

The magnitudes of the modifications to the values of the Brillouin shift and linewidth implied are considerably smaller than that which can be experimentally observed. However, the experimental results of Fleury and Boon (17) on liquid Argon indicate a finite and systematic difference between the hypersonic ($\sim$ 3 GHz) and ultrasonic ($\sim$ 1 MHz) velocities of sound in this liquid. Because these data cover only a small range of temperature and were obtained at one scattering angle, further investigation into this effect is carried out in this work.

References in Chapter II

(1) D. McIntyre, J.V. Senger in 'Physics of Simple Liquids' edited by H.N.V. Tumperley, J.S. Rawlinson, and G.S. Rushbrooke, North-Holland Publishing Company (1968)

(2) L.D. Landau, E.M. Lifshitz; 'Statistical Physics' English Translation, Pergamon Press (1959)

(3) I.L. Fabelinskii; 'Molecular Scattering of Light' English Translation, Plenum Press (1968)

(4) W.K.H. Panofsky, M. Philips; 'Classical Electricity and Magnetism', Addison-Wesley (1962)

(5) C. Kittel; 'Elementary Statistical Physics' John Wiley and Sons (1958)

(6) R.D. Mountain; Rev. Mod. Phys. 38, 205 (1966)

(7) L.P. Kadanoff, P.C. Martin; Ann. Phys. 24, 419 (1963)

(8) B.U. Felderhof, I. Oppenheim; Physica 31, 1441 (1965)

(9) L.D. Landau, E.M. Lifshitz; 'Fluid Mechanics' English Translation, Pergamon Press (1958)

(10) See Appendix I

(11) See Appendix II and Appendix of Ref. 23 of Ch. I

(12) C.J. Montrose, V.A. Solovyev, T.A. Litovitz; J. Acous. Soc. Amer. 43, 117 (1968)

(13) A. Rahman; Phys. Rev. 136, A 405 (1964)

(14) K. Sköld, K.E. Larson; Phys. Rev. 161, 102 (1967)

(15) J.P. Boon, P. Deguent; Phys. Rev. A 2542 (1970)

(16) B.J. Berne, J.P. Boon, S.A. Rice; J. Chem. Phys. 47, 2283 (1967)

(17) Reference (17) in Chapter I

# CHAPTER III

# THEORY OF LIGHT SCATTERING FROM A BINARY MONATOMIC GAS MIXTURE

## 3.1. Introduction

The shape of the spectrum of light scattered from a gaseous system in general depends on the ratio of the wavelength of the fluctuations which produce the scattering (characteristic of the scattering geometry) to the collision mean free path of the atoms. The characteristic wavelength, $\Lambda$, is that associated with the momentum transfer in the scattering process, defined as:

$$\Lambda = \frac{\lambda}{2 \sin (\theta/2)} \tag{3.1}$$

where $\lambda$ is the wavelength of the incident light in the medium and $\theta$ is the scattering angle. When $\Lambda$ is much greater than the mean free path the system can be regarded as a continuum, describable by the hydrodynamic equations. When $\Lambda$ is smaller than the mean free path, interatomic collisions are unimportant and the system has to be treated in terms of the kinetics of the atoms. In this case the spectrum of the scattered light approaches the Doppler lineshape of a Gaussian distribution of atomic velocities. In this work we consider only the hydrodynamic case, and outline the derivation of the form of the spectrum of light scattered from a binary mixture of monatomic gases.

A detailed derivation of the form of the spectrum of light scattered from mixtures (1 - 4) was first given by Mountain and Deutch (1) for the case of a binary liquid mixture. This method of analysis was subsequently applied, with more mathematical rigour, by Cohen, et al. (4) to the case of a binary gaseous mixture.

Here we outline the method and emphasise only the important terms in the calculations.

## 3.2. Binary Monatomic Gaseous Mixture

In a binary mixture the fluctuations in the local dielectric constant, $\Delta\varepsilon(\bar{r}, t)$ may be related (in the same way as that outlined for the pure liquid) to the fluctuations in the local thermodynamic quantities, with the addition of the local concentration fluctuations. Following Mountain and Deutch (1) we choose the statistically independent set of variables $(P, \phi, C)$ where

$$\phi = T_1 - \frac{T_0 \alpha_T}{\rho_0 C_p} P_1; \quad \Delta\phi = \Delta T_1 - \frac{T_0 \alpha_T}{\rho_0 C_p} \Delta P_1 \qquad (3.2)$$

where P and T are the pressure and temperature of the system and C is the mass concentration of the solute. Zero subscripts indicate the equilibrium values and subscript 1 indicates the local fluctuation value. $\alpha_T$ is the thermal expansion coefficient of the system.

The fluctuations in the local dielectric constant $\Delta\varepsilon(\bar{r}, t)$ of the system may then be expressed as:

$$\Delta\varepsilon(\bar{r},t) = \left(\frac{\partial\varepsilon}{\partial P}\right)_{\phi,C} \Delta P\ (\bar{r},t) + \left(\frac{\partial\varepsilon}{\partial\phi}\right)_{P,C} \Delta\phi(\bar{r},t) + \left(\frac{\partial\varepsilon}{\partial C}\right)_{P,\phi} \Delta C(\bar{r},t) \tag{3.3}$$

Using the state variables (P, $\phi$, C) and the Gaussian distribution approximation, the probability W of establishing a fluctuation with changes of ($\Delta$P, $\Delta\phi$, $\Delta$C) from the equilibrium values is given by (5):

$$W \alpha \exp\left\{-\frac{1}{2k_B T_0}\left[\frac{\beta_s}{\rho_0}(\Delta P)^2 + \frac{C_p}{T_0}(\Delta\phi)^2 + \left(\frac{\partial\mu}{\partial C}\right)_{P,T}(\Delta C)^2\right]\right\} \tag{3.4}$$

where $\beta_s$ is the adiabatic compressibility:

$$\beta_s = \frac{1}{\rho_0}\left(\frac{\partial\rho}{\partial P}\right)_{S,C} = \frac{\beta_T}{\gamma} \tag{3.5}$$

and $\mu$ is the chemical potential of the mixture.

From the expression for the fluctuations in the dielectric constant (3.3) and the definition of the generalised structure factor, $S_\varepsilon(K, \omega)$, we can write:

$$S_\varepsilon(K,\omega) = 2\,\mathrm{Re}\left\{\left(\frac{\partial\varepsilon}{\partial P}\right)^2 < P(K, s)P(-K, 0)> + \left(\frac{\partial\varepsilon}{\partial\phi}\right)^2 < \phi(K, s)\phi(-K, 0) > + \left(\frac{\partial\varepsilon}{\partial C}\right)^2 < C(K, s)C(-K, 0) > \right\} \tag{3.6}$$

ignoring the term in $\langle \phi C \rangle$ which is assumed to be small*.

For the binary gas mixture we define the following quantities.

$$
\begin{aligned}
m_1 &= \text{mass of solvent atom} \\
m_2 &= \text{mass of solute atom} \\
n_i &= \text{number of density of component } i \\
n &= n_1 + n_2 \\
x_i &= \text{number fraction of atoms of component } i \\
&= n_i/n \\
\rho &= \text{mass density of the mixture} \\
&= n_1 m_1 + n_2 m_2 \\
C &= \text{mass concentration of solute} \\
&= n_2 m_2/\rho \\
P &= \text{pressure of the system} \\
\mu_i &= \text{chemical potential of component } i \\
&= k_B T \ln (n_i k_B T) \\
\mu &= \text{chemical potential of mixture} \\
&= \frac{\mu_1}{m_1} - \frac{\mu_2}{m_2} \\
D &= \text{the mutual diffusion coefficient} \\
k_T &= \text{the thermal diffusion ratio} \\
k_P &= \text{pressure diffusion coefficient} \\
&= \left[(P_0/\rho^2)(\partial\rho/\partial C)_{P,T}\right] (\partial\mu/\partial C)_{P,T} \\
\lambda &= \text{the thermal conductivity}
\end{aligned}
\qquad (3.7)
$$

---

* This term contributes to the unshifted line only (see references (1) and (4)), and since it is small it is not expected to affect the shift of the Brillouin lines.

## 3.3. The Hydrodynamic Equations

For a binary mixture in a state of thermal equilibrium the deviations of the system from its equilibrium condition may be assumed to be small. Thus the linearized hydrodynamic equations adequately describe the system. For a binary fluid mixture the equations of mass conservation (continuity equation) and momentum conservation (Navier-Stokes equation) are the same as those for a pure fluid (2.27 - 28) which we rewrite here for ease of reference. Thus the linearised hydrodynamic equations for the binary mixture are:

(a) the continuity equation;

$$\frac{\partial \rho_1}{\partial t} + \rho_0 \, \nabla.\bar{v} = 0 \qquad (3.8)$$

(b) the longitudinal part of the Navier-Stokes equation;

$$\rho_0 \frac{\partial \bar{v}}{\partial t} = -\nabla P + (\frac{4}{3}\eta_s + \eta_B) \, \nabla(\nabla.\bar{v}) \qquad (3.9)$$

(c) the energy transport equation;

$$\rho_0 C_p \frac{\partial T}{\partial t} - \rho_0 k_T (\frac{\partial \mu}{\partial C})_{P,T} \frac{\partial C}{\partial t} + \rho_0 T_0 (\frac{\partial S}{\partial P})_{T,C} \frac{\partial P}{\partial t} = \lambda \nabla^2 T \qquad (3.10)$$

and

(d) the diffusion equation;

$$\frac{\partial C}{\partial t} = D\{\nabla^2 C + (\frac{k_T}{T_0}) \, \nabla^2 T + (\frac{k_p}{P_0}) \, \nabla^2 P\} \qquad (3.11)$$

The time dependence of the correlation functions of the local thermodynamic variables are then computed according to the linearlized hydrodynamic equations (3.8 - 11).

The procedure is described in detail in references (1) and (4). The hydrodynamic equations (3.8 - 11) are Fourier-Laplace transformed. The dispersion relation, D(s), for the system is obtained by solving these transformed hydrodynamic equations. Writing $\psi \equiv \nabla.\bar{v}$, we use the set of variables, ($\mathcal{P}$, $\phi$, C, $\psi$), which transform as follows:

$$P(\bar{r}, t) \rightleftharpoons P(K, s)$$

$$\phi(\bar{r}, t) \rightleftharpoons \phi(K, s)$$

$$C(\bar{r}, t) \rightleftharpoons C(K, s)$$

$$\psi(\bar{r}, t) \rightleftharpoons \psi(K, s)$$

The transformed variables are expressed in terms of the initial conditions P(K, O), $\phi$(K, O), C(K, O) and $\psi$(K, O).

The transformed hydrodynamic equations can be written in matrix form as:

$$\underset{\sim}{D}(s) \cdot \underline{\hat{N}}(K, s) = \underset{\sim}{T} \cdot \underline{N}(K, O) \qquad (3.12)$$

where $\hat{N}(K, s)$ is a column vector:

$$\hat{N}(K, s) = \{\hat{C}(K, s) \quad \hat{P}(K, s) \quad \hat{\phi}(K, s) \quad \hat{\psi}(K, s)\}$$

D(s) is a 4 x 4 matrix of the form:

$$D(s)=\begin{bmatrix} s(\partial\rho/\partial C)_{P,T} & s/C_0^2 & s(\partial\rho/\partial_T)_{P,C} & \rho_0 \\ 0 & -K^2/\rho_0 & 0 & s+bK^2 \\ s+DK^2 & DK^2\left[K_p/\rho_0+\frac{k_T\alpha_T}{\rho_0 C_p}\right] & DK^2(k_T/T_0) & 0 \\ -s\left(\frac{k_T}{C_p}\right)(\partial\mu/\partial C)_{P,T} & aK^2(T_0\alpha_T/\rho_0 C_p) & s+aK^2 & 0 \end{bmatrix} \tag{3.13}$$

and T is a 4 x 4 matrix of the form:

$$T=\begin{bmatrix} (\partial\rho/\partial C)_{P,T} & 1/C_0^2 & (\partial\rho/\partial_T)_{P,C} & 0 \\ 0 & 0 & 0 & 1 \\ 1 & 0 & 0 & 0 \\ -(k_T/C_p)(\partial\mu/\partial C)_{P,T} & 0 & 1 & 0 \end{bmatrix} \tag{3.14}$$

where

$$a = \lambda/\rho_0 C_p$$

$$b = \left(\frac{4}{3}\eta_s + \eta_B\right)/\rho_0$$

as in Chapter II.

Mountain and Deutch obtained the lowest order non-trivial factorization of the characteristic determinant, $|D(s)|$. This is shown to be:

$$D(s) \simeq (s + \Gamma_+)\ (s + \Gamma_-)\ (s - i\omega_0 + \Gamma_B)\ (s + i\omega_0 + \Gamma_B) \qquad (3.15)$$

where

$$\Gamma_\pm = \frac{1}{2} K^2 [a + D_c] \pm \frac{1}{2} K^2 \{[a + D_c]^2 - 4aDK^2\} \qquad (3.16)$$

$$D_c = D[1 + (k_T^2/T_0 C_p)(\partial\mu/\partial C)_{P,T}] \qquad (3.17)$$

$$\Gamma_B = \frac{1}{2}K^2 \{b + a(\gamma - 1) + \frac{DC_0^2}{\rho_0^2}(\frac{\partial C}{\partial \mu})_{P,T}[(\frac{\partial \rho}{\partial C})_{P,T} + \frac{k_T}{C_p}(\frac{\partial \rho}{\partial T})_{P,C}(\partial\mu/\partial C)_{P,T}]^2\} \qquad (3.18)$$

Thus the roots related to the two propagating modes are:

$$s = \pm i\omega_0 - \Gamma_B \qquad (3.19)$$

and the roots related to the non-propagating modes are:

$$s_\pm = -\Gamma_\pm \qquad (3.20)$$

In equation (3.15) we see that there are two roots corresponding to non-propagating components in the spectrum which are unshifted in frequency (3.20). Their linewidths are equal to $\Gamma_\pm$. These components arise from the coupled energy transport and diffusion in the mixture,

as can be shown by solving (3.10) and (3.11) with the constraints of constant pressure;

$$\left[\dot{P} = \nabla^2 P = \frac{\partial P}{\partial t} = 0\right]$$

The dispersion relation then becomes:

$$s^2 + (aK^2 + D_c K^2)s + aDK^4 = 0 \tag{3.21}$$

When the coupling between the energy transport and diffusion is small, that is when

$$\frac{k_T^2}{T_0 C_p} \left(\frac{\partial \mu}{\partial C}\right)_{p,T} << 1 \quad \text{or} \quad D_c \simeq D \tag{3.22}$$

the roots of (3.21) are

$$\Gamma_+ \simeq aK^2 \tag{3.23}$$

and

$$\Gamma_- \simeq DK^2 \tag{3.24}$$

Thus the unshifted line consists of two Lorentzians of linewidths arising from thermal damping and diffusion damping respectively.

Looking at the roots corresponding to the propagating modes we note that equation (3.18) for $\Gamma_B$ contains the transport coefficients of a general fluid mixture. Further simplification of this equation can be made in the case of the binary gas mixture. In a gaseous system the term in (3.18) involving the thermal conductivity is much smaller

than either the viscosity or the diffusion term. Indeed, Aref'ev has shown that for certain gas mixtures both the thermal conductivity and viscosity terms are negligible compared with the diffusion term (6). Thus we can simplify (3.18) into the form:

$$\Gamma_B \simeq \frac{1}{2}K^2\{b + \frac{DC_0^2}{\rho_0^2}\left(\frac{\partial C}{\partial \mu}\right)_{P,T}\left(\frac{\partial \rho}{\partial C}\right)^2\} \tag{3.25}$$

## 3.4. The Correlation functions and the Spectrum of the Scattered Light

With the above roots of the dispersion equation (3.23 - 25) we can obtain a simplified form of the correlation functions of the thermodynamic variables. The simplifications discussed in the last section have the effect of decoupling the fluctuations in $\phi$ and C. Thus we can write a modified form of the correlation function (Cohen, et al. (4)):

$$\frac{\langle P(K,t)P(K)\rangle}{\langle|P(K)|^2\rangle} = e^{-\Gamma_B t}\cos(\omega_0 t) + \frac{(\Gamma_B - bK^2)}{\omega_0} e^{-\Gamma_B t}\sin(\omega_0 t) \tag{3.26}$$

(propagating fluctuations)

$$\frac{\langle\phi(K,t)\phi(-K)\rangle}{\langle|\phi(K)|^2\rangle} = e^{-\Gamma_+ t} \tag{3.27}$$

$$\frac{\langle C(K,t)C(-K)\rangle}{\langle|C(K)|^2\rangle} = e^{-\Gamma_- t} \tag{3.28}$$

(non-propagating fluctuations)

The ensemble average values of the initial thermodynamic variables: $\langle|\mathbf{P}(K)|^2\rangle$, $\langle|\phi(K)|^2\rangle$ and $\langle|C(K)|^2\rangle$ are obtained from the probability distribution function (3.4). These can be seen to be:

$$\langle|\mathbf{P}(K)|^2\rangle = \frac{k_B T_0 \rho_0}{\beta_s} \tag{3.29}$$

$$\langle|\phi(K)|^2\rangle = \frac{k_B T_0}{C_p} \tag{3.30}$$

$$\langle|C(K)|^2\rangle = k_B T_0 \left(\frac{\partial C}{\partial \mu}\right)_{P,T} \tag{3.31}$$

With the correlation functions (3.26 - 28), the ensemble averaged initial values (3.29 - 31) and using the definition of the power spectrum (2.16) we obtain the generalised structure factor $S_\varepsilon(K, \omega)$:

$$\begin{aligned} S_\varepsilon(K,\omega) = {} & \left(\frac{\partial \varepsilon}{\partial \mathbf{P}}\right)^2_{\phi,C} \frac{k_B T_0 \rho_0}{\beta_s} \left( \frac{\Gamma_B}{(\Gamma_B)^2+(\omega+\omega_0)^2} + \frac{\Gamma_B}{(\Gamma_B)^2+(\omega-\omega_0)^2} \right) \\ & + \left(\frac{\partial \varepsilon}{\partial C}\right)^2_{P,T} k_B T_0 \left(\frac{\partial C}{\partial \mu}\right)_{P,T} \left( \frac{2\Gamma_-}{(\Gamma_-)^2+\omega^2} \right) \\ & + \left(\frac{\partial \varepsilon}{\partial T}\right)^2_{P,C} \frac{k_B T_0^2}{C_p} \left( \frac{2\Gamma_+}{(\Gamma_+)^2+\omega^2} \right) \\ & + \left(\frac{\partial \varepsilon}{\partial \mathbf{P}}\right)^2_{\phi,C} \frac{k_B T_0 \rho_0}{\beta_s} \frac{(\Gamma_B - bK^2)}{\omega_0} \left( \frac{\omega+\omega_0}{(\Gamma_B)^2+(\omega+\omega_0)^2} - \frac{\omega-\omega_0}{(\Gamma_B)^2+(\omega-\omega_0)^2} \right) \end{aligned} \tag{3.32}$$

The first terms in (3.32) give rise to the two shifted Brillouin lines of Lorentzian shape, shifted in frequency by $\pm \omega_0$ with linewidth $2\Gamma_B$. In the case of the mixture $\Gamma_B$ contains a contribution arising from the mutual diffusion of the components (3.25). The diffusion contribution is present here because sound waves give rise to peressure and temperature gradients which give rise to irreversible mass diffusion.

The spectrum also contains two non-propagating components which are unshifted in frequency, of Lorentzian shape. The linewidths of these lines, $\Gamma_+$ and $\Gamma_-$ , are governed by thermal conduction and mass diffusion respectively. Since in a gaseous mixture $a < D$ the part arising from the heat conduction will appear as a sharp narrow peak superimposed on a broader peak arising from the diffusion.

The last term in (3.32) gives rise to the two shifted asymmetric lines which pass through zero at $\pm \omega_0$. As is the case in a pure fluid (Chapter II: Section 2.4), these asymmetric lines have the effect of distorting the shape of the Brillouin lines.

The resultant spectrum is the summation of these various components and is shown in Figure (3.1)*

---

* Although it is convenient to use this approach and 'break up' the spectrum into the various components, experimentally it is the resultant spectrum that is observed and it is not an easy task to separate out the components.

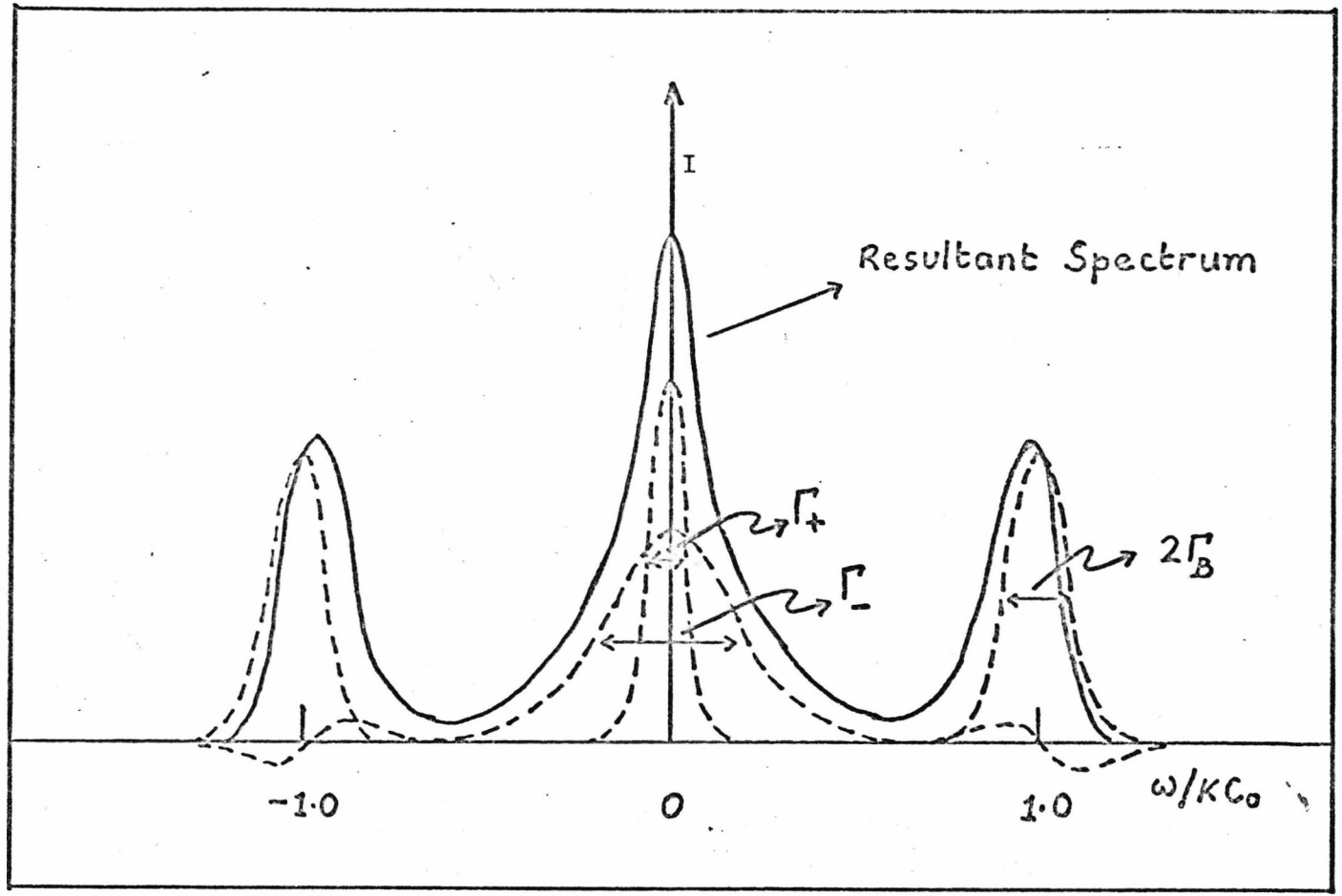


FIGURE 3.1: Schematic diagram of the Spectrum of Light scattered from a binary gas mixture, showing the important components.

Finally, using the definitions (3.7) we can calculate the various derivatives appearing in the equations:

For the partial derivative $(\partial\mu/\partial C)_{P,T}$ we use the fact that for a gaseous system we can make the approximation $P = nk_BT$. Thus constant P and T implies constant n. Then we have:

$$\left(\frac{\partial\mu}{\partial C}\right)_{P,T} = \frac{\partial}{\partial C}\left\{\frac{k_BT\ \ln\ (n_1k_BT)}{m_1} - \frac{k_BT\ \ln\ (n_2k_BT)}{m_2}\right\}\Bigg|_n \qquad (3.33)$$

$$= -\frac{\rho}{n_1n_2m_1m_2}\ k_BT\left(\frac{\partial n_2}{\partial C}\right)_n$$

But $$\left(\frac{\partial n_2}{\partial C}\right)_n = \frac{\rho^2}{nm_1m_2} \qquad (3.34)$$

Thus we get:

$$\left(\frac{\partial\mu}{\partial C}\right)_{P,T} = -\frac{k_BT\rho}{nm_1m_2C(1-C)} \qquad (3.35)$$

Similarly we find the partial derivatives:

$$\left(\frac{\partial\rho}{\partial C}\right)_{P,T} = \frac{\rho^2(m_2-m_1)}{nm_1m_2} \qquad (3.36)$$

$$k_P = \frac{P/\rho^2\,(\partial\rho/\partial C)_{P,T}}{(\partial\mu/\partial C)_{P,T}} = \frac{-(m_2-m_1)C(1-C)n}{\rho} \qquad (3.37)$$

We also have:

$$\left(\frac{\partial\rho}{\partial T}\right)_{P,C} = -\rho/T \qquad (3.38)$$

Finally, for the adiabatic sound velocity $C_0$ in the system we can use:

$$C_0^2 = \left(\frac{\gamma P}{\rho}\right) = \left(\frac{5}{3}\frac{k_B T}{\bar{m}}\right) \tag{3.39}$$

where $\bar{m} = m_1 x_1 + m_2 x_2$ . (3.40)

$\bar{m}$ can be regarded as the mean molecular mass of the mixture.

For a binary gaseous mixture the dielectric constant at optical frequencies can be adequately represented by the Clausius-Mossoti formula:

$$\frac{\varepsilon-1}{\varepsilon+2} = \frac{4\pi}{3}\left[\left(\frac{\alpha_1}{m_1}\right)\rho_1 + \left(\frac{\alpha_2}{m_2}\right)\rho_2\right] \tag{3.41}$$

where $\alpha_i$ and $\rho_i$ are the molecular polarizability and mass density of component i. In terms of C, the mass fraction of the second component (solute), we have:

$$\frac{\varepsilon-1}{\varepsilon+2} = \frac{4\pi}{3}\rho\left[\frac{\alpha_1}{m_1} + \left(\frac{\alpha_2}{m_2} - \frac{\alpha_1}{m_1}\right)C\right] \tag{3.42}$$

so that $\varepsilon = \varepsilon(\rho, C)$.

Noting that for a gaseous system $\varepsilon + 2 \simeq 3$ we can approximate (3.42) to a form:

$$\varepsilon - 1 \simeq 4\pi\rho\left[\frac{\alpha_1}{m_1} + \left(\frac{\alpha_2}{m_2} - \frac{\alpha_1}{m_1}\right)C\right] \tag{3.43}$$

and the derivatives of the dielectric constant with respect to the parameters (P, $\phi$, C) can be calculated accordingly. These derivatives may be evaluated using the thermodynamic relations:

$$\left(\frac{\partial \varepsilon}{\partial C}\right)_{P,\phi} = \left(\frac{\partial \varepsilon}{\partial C}\right)_{P,T} \tag{3.44}$$

$$\left(\frac{\partial \varepsilon}{\partial \phi}\right)_{P,C} = \left(\frac{\partial \varepsilon}{\partial T}\right)_{P,C} \tag{3.45}$$

and

$$\left(\frac{\partial \varepsilon}{\partial P}\right)_{\phi,C} = \left(\frac{\partial \varepsilon}{\partial P}\right)_{T,C} + \frac{T\alpha_T}{\rho C_p}\left(\frac{\partial \varepsilon}{\partial T}\right)_{P,C} \tag{3.46}$$

## 3.5. Dispersion of Sound Velocity in a Binary Gas Mixture

The equations of hydrodynamics applies in the low-frequency long-wavelength region and in this limit the velocity of sound in the system is assumed to obey the classical adiabatic form. Hence the Brillouin frequency shift is given by $\omega_0 = KC_0$. However, recent observation of Brillouin scattering in the gas mixture He - $SF_6$ by Gornall, et al (7) showed that the Brillouin shifts are smaller than that calculated from the adiabatic sound velocity. These workers attributed this phenomenon to the effect of strong coupling between the hydrodynamic modes due to the high diffusion rate in the mixture. The observed lowering and broadening of the Brillouin lines is attributed to the damping effect of the diffusion.

The effects of diffusion on the propagating modes had been considered by Lekkerkerker and Boon (8). Neglecting transport phenomena other than diffusion they obtained the dispersion equation, $D(s)$ for the binary mixture as:

$$D(s) = s^3 + DK^2(C_0/C_x)^2 s^2 + (KC_0)^2 s + DK^2(KC_0)^2 \qquad (3.47)$$

where

$$\frac{1}{C_x^2} = \frac{1}{C_0^2} + \frac{1}{\rho^2}\left(\frac{\partial\rho}{\partial C}\right)^2_{P,T} \Big/ (\partial\mu/\partial C)_{P,T} \qquad (3.48)$$

For the two limiting cases of ($DK^2 << KC$) and ($DK^2 >> KC$) these authors obtained the roots of the dispersion equation (3.47) as:

$$-DK^2 \; ; \quad \pm iC_0K - \frac{1}{2}\left(\frac{D}{C_0}\right)\left(\frac{C_0^2 - C_x^2}{C_x^2}\right)K^2 \qquad (3.49)$$

and

$$-D\left(\frac{C_0}{C_x}\right)^2 K^2 \; ; \quad \pm iC_xK - \frac{1}{2}\left(\frac{C_x}{D}\right)\left(\frac{C_0^2 - C_x^2}{C_0^2}\right) \qquad (3.50)$$

respectively.

For high K values (3.50) shows that the width of the Brillouin lines is constant. This is to be compared with the $K^2$ dependence of the linewidth for low K values (3.49). The results show that the coupling between the diffusion mode and the sound modes causes the sound velocity to change from the adiabatic value $C_0$ to a lower value $C_x$. The broadening in the Brillouin lines which accompanies an increase in the concentration of the lighter component of the mixture is explained by the increase in the thermodynamic quantity $(C_0^2 - C_x^2)$. This behaviour is

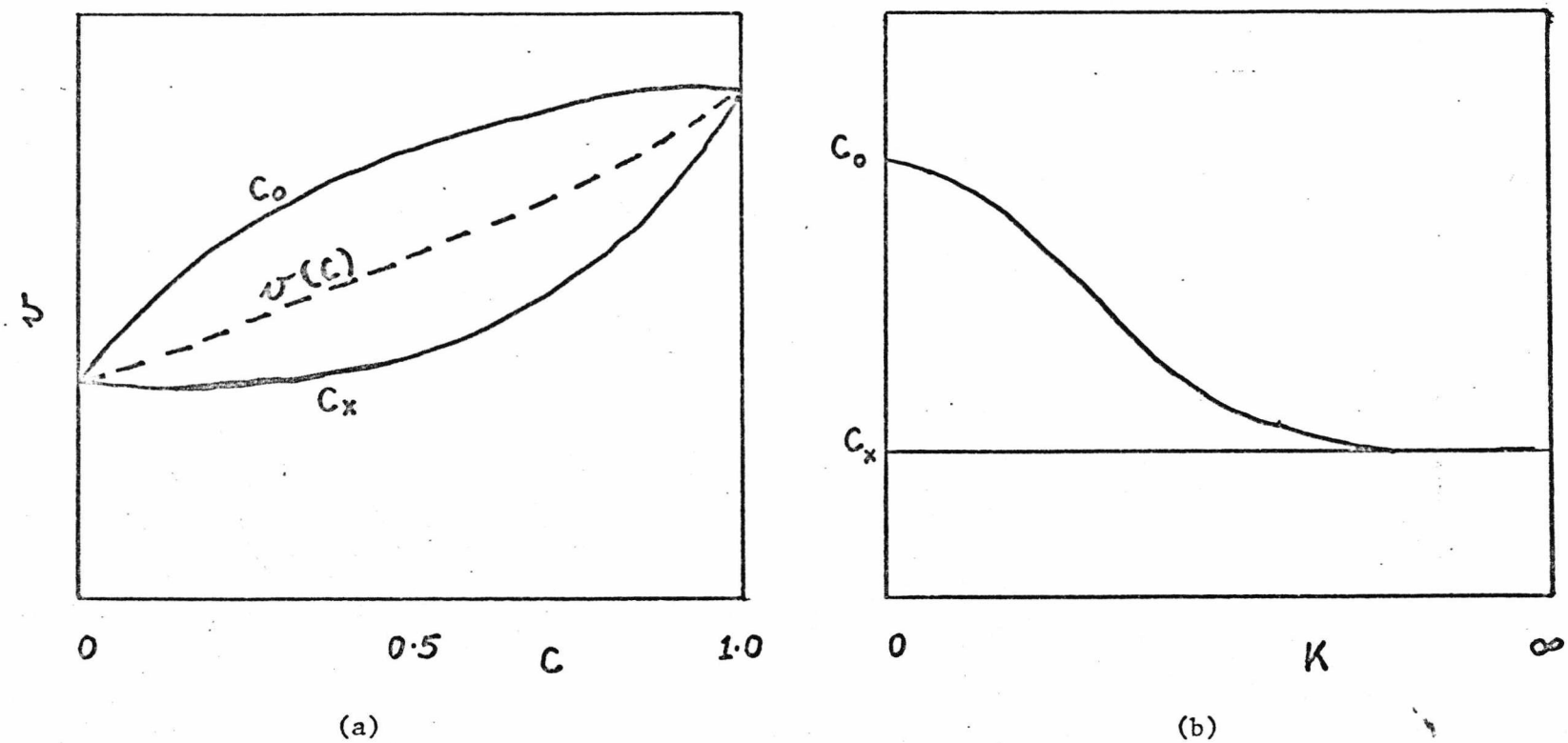


FIGURE 3.2: Qualitative behaviour of the velocity of sound in a gas mixture as a function of (a) Concentration and (b) Scattering vector. C refers to the mass fraction of the lighter component.

depicted in Figures (3.2).

We can summarize briefly by stating that the linearized hydrodynamic equations yield the spectrum of the scattered light from a binary gas mixture in terms of the transformed thermodynamic variables of the system. The concentration diffusion in the system contributes towards the broadening of the Brillouin lines as well as towards an additional unshifted line of Lorentzian shape.

References in Chapter III

(1) R.D. Mountain, J.M. Deutch; J. Chem. Phys. 50, 1103 (1969)

(2) L. Blum; J. Chem. Phys. 50, 17 (1969)

(3) H.N.W. Lekkerkerker, W.G. Laidlaw; Phys. Chem. Liq. 3, 175 (1972)

(4) C. Cohen, J.W.H. Sutherland, J.M. Deutch; Phys. Chem. Liq. 2, 213 (1971)

(5) L.D. Landau, E.M. Lifshitz; 'Statistical Physics', English Translation, Pergamon PRESS (1959)

(6) I.M. Aref'ev, JETP Lett. 10, 340 (1969)

(7) W.S. Gornall, C.S. Wang, C.C. Yang, N. Bloembergen; Phys. Rev. Lett. 26 1094 (1971)

(8) H.N.W. Lekkerkerker, J.P. Boon; Phys. Lett. 39, A 9 (1972)

# CHAPTER IV

# APPARATUS AND EXPERIMENTAL TECHNIQUES

## 4.1.1. Introduction

In this chapter we describe the apparatus and experimental techniques used to obtain the spectrum of the scattered light. We also describe the details of the analysis of the spectrum used to obtain information about the properties of the scattering medium.

We begin by discussing the conditions under which measurements are to be taken and consider the characteristics of the apparatus necessary to enable us to do these measurements.

In our studies of the rare gas liquids we are interested in obtaining from the spectrum of the scattered light information on: (a) the sound velocity, (b) the sound absorption coefficient and (c) whether there is evidence of measurable dispersion in the velocity of sound in these liquids at hypersonic frequencies.

The experimental investigation to establish the presence of dispersion in the sound velocity can be approached in two ways. The first is to make a measurement of the sound velocity at the hypersonic frequency, i.e. by light scattering, at a convenient scattering angle ($90^{\circ}$ scattering being the most convenient in general) and compare the results with those of measurements by ultrasonics. Measurement of sound velocity in the rare gas liquids by ultrasonic method has been performed by various workers

and reported extensively. The second method is to perform light scattering measurements at different scattering angles (hence different frequencies) and compare the results. In the latter case we have to perform measurements over as large a range of angles as possible to obtain the maximum range in the frequencies of the observed sound waves. Furthermore this approach gives us the advantage of comparing results obtained from the same sample under the same thermodynamic conditions. Consequently any systematic errors in the different measurements due to inaccuracies in the measurement of local temperature, etc. are eliminated.

The sound absorption coefficient can be calculated from the width of the Brillouin lines. The Brillouin linewidth is at least one order of magnitude smaller than the Brillouin shifts. Thus measurement of Brillouin linewidths requires high resolution instruments. However, the Brillouin linewidths have a squared dependence on the scattering vector, i.e. $\Gamma_B \alpha K^2$. Hence it is easier to measure the linewidth when the measurement is performed in the backward scattering direction, as the linewidth will then be at its maximum. This is illustrated in Figure (4.1) which shows the significant difference in the linewidths of the forward and backward scattered spectra from liquid Krypton (recorded simultaneously).

For the binary gas mixture the objectives of the experiments are: (a) to determine the sound velocity and sound absorption coefficient as a function of concentration and (b) to determine the dependence of the sound velocity

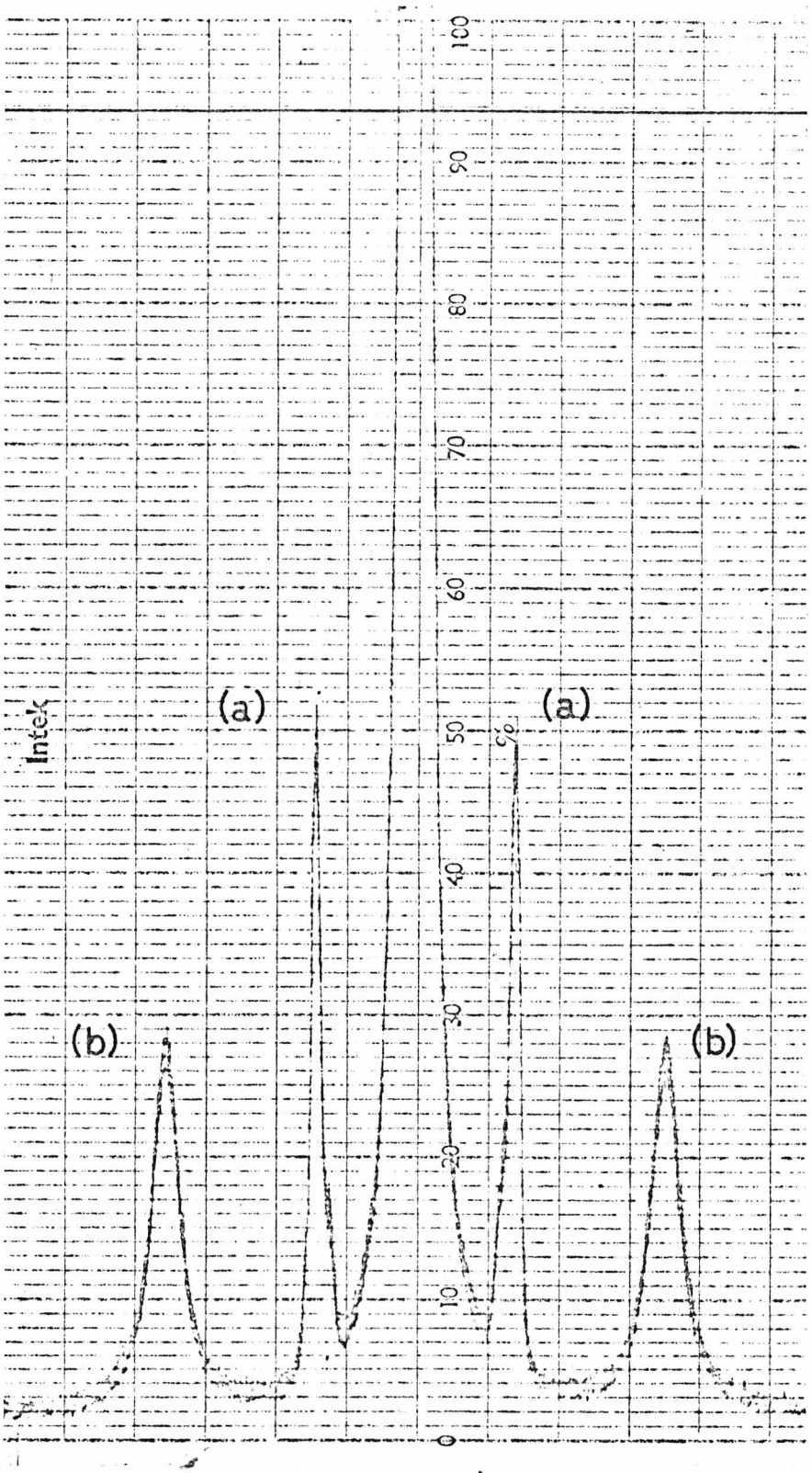


Figure 4.1: Brillouin linewidths of the scattered light from liquid Krypton at 120 °K: (a) $\theta = 9°$, (b) $\theta = 171°$.

and absorption coefficient on the scattering vector. Thus both the experiments on the rare gas liquids and the binary gas mixtures have similar geometrical requirements.

The measurements on the rare gas liquids were taken along the saturated vapour pressure curve from near the triple point to near the critical point. Hence the measurements cover a large range of sound velocities in the liquids, and consequently a large range of frequency shifts was spanned. (The range of frequency shifts measured in the gas mixtures was considerably smaller). The range of frequencies covered in the whole set of experiments was from $\sim$300 MHz to $\sim$4 GHz. This governed the choice of interferometers which could be used. They are described in more detail in sections (4.3) and (4.4).

### 4.1.2. Outline of Apparatus

Figure (4.2) shows a schematic diagram of a typical experimental set-up for observing the spectrum of light scattered from the sample. The laser is a 'Coherent Radiation Laboratories' (CRL) model 52 Argon ion laser which can be tuned to operate at several lines in the region of 5000Å. The scattered light from the sample is analysed with a Fabry-Perot (FP) interferometer, essentially a single channel frequency filter. The light transmitted by the FP is detected with standard photon counting technique. Data could be recorded either through a linear rate meter onto an x-t chart recorder or through a digital rate meter (designed and constructed in this laboratory) and stored on

Figure 4.2: Schematic diagram of standard experimental set-up.

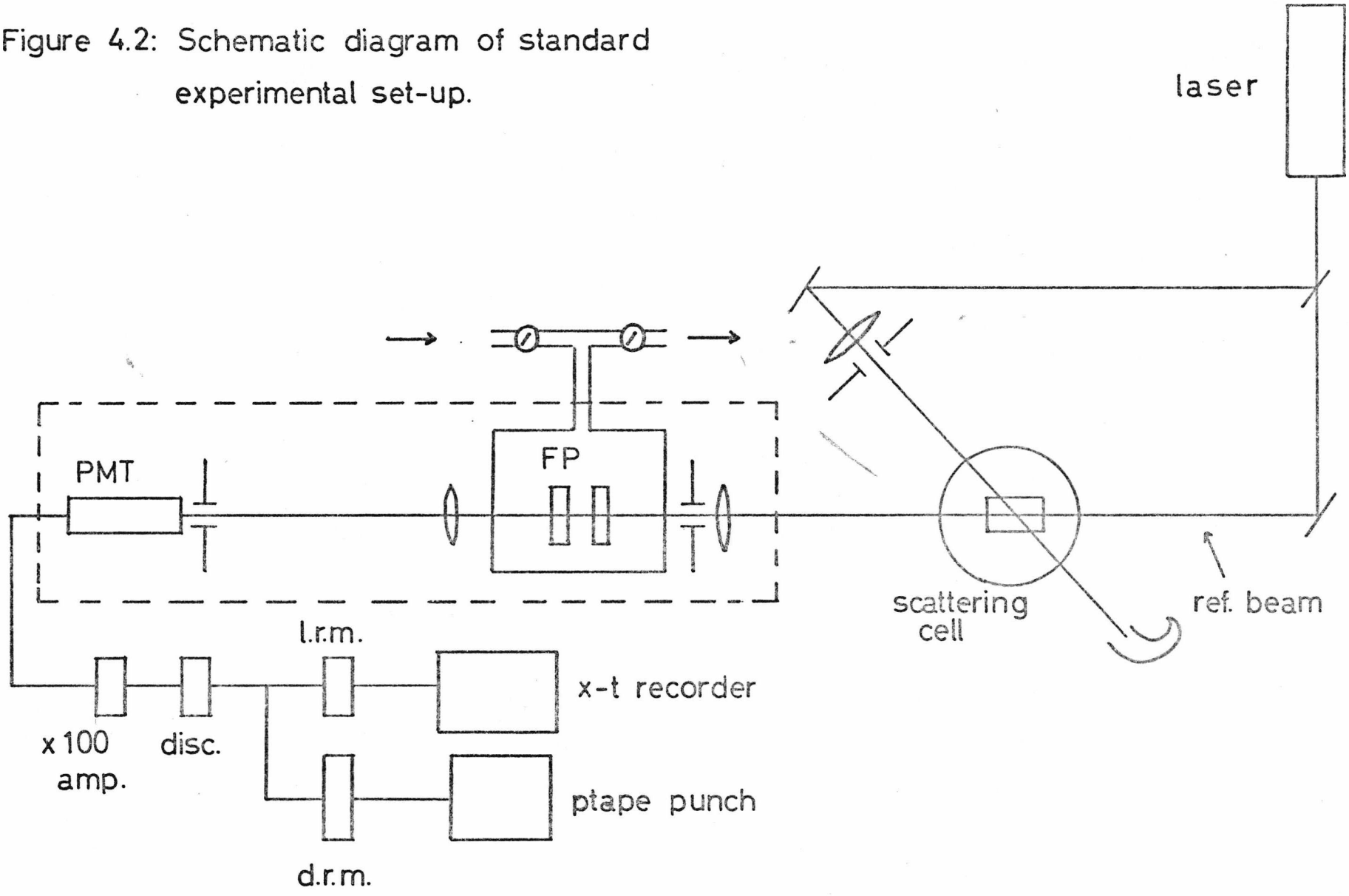

paper tape. These two means of recording data could also be used simultaneously.

The FP is a periodic instrument, i.e. the transmission function of the instrument is repeated every time it is scanned through a free spectral range. This periodicity of the FP transmission function is used for frequency calibration. The recorded spectrum is the result of the convolution of the spectrum of the scattered light with the transmission function of the FP.

In the rest of this chapter we will describe the various parts of the apparatus in more detail.

## 4.2. The Laser

### 4.2.1. Introduction

The light source used in the experiments was a Coherent Radiation Laboratories (CRL) Model 52 Argon ion laser, which has been available commercially for several years. The theory of operation of the gas laser has been studied and published extensively (1), consequently it is unnecessary to discuss them in detail in this work. However, it is essential that we recognise the properties of the laser which are important for light scattering experiments. These include parameters such as the power and frequency stability of the laser.

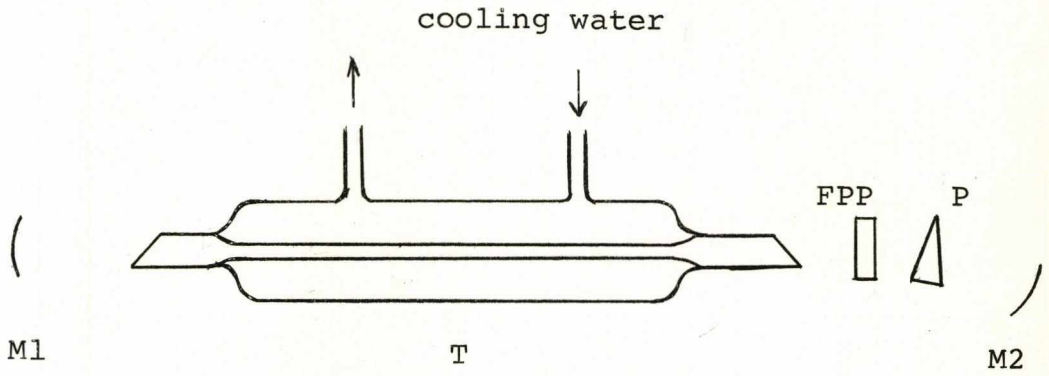


Figure 4.3: Schematic diagram of the Laser Cavity

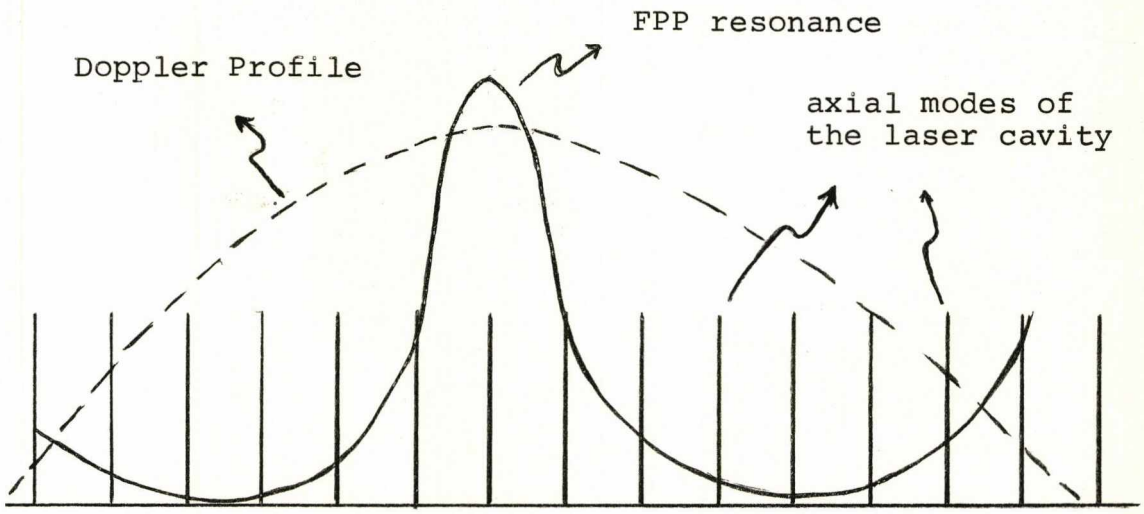


Figure 4.4: Single mode selection with the FPP intracavity etalon

4.2.2. Operation

Figure (4.3) shows a schematic drawing of the laser cavity. The laser cavity is formed by the spherical reflectors M1 and M2, which enclose the plasma tube T. Wavelength selection is obtained with the adjustable minimum deviation prism P. FPP is an intracavity etalon which acts as a frequency filter, selecting one of the modes in the Doppler profile of the laser, as shown in Figure (4.4). Hence the system produces highly monochromatic light, the wavelengths of which could be any of the laser-active transitions of the argon ion. In practice either the 4880$\mathring{A}$ or the 5145$\mathring{A}$ lines were used, these lines being the strongest available. The optical power output of the laser at these lines was about 500 mW.

4.2.3. Power Stability

The instabilities with which we are concerned can be classified as long term instabilities (2). Long term here means periods greater than the time it takes to record a spectrum, typically of the order of twenty minutes to half an hour. Fluctuations in the power output of the laser are mainly caused by thermal relaxation of the mechanical parts of the laser cavity. This manifests itself in the 'warming-up' period of the laser. This means that the laser requires some time to reach thermal equilibrium before it will operate satisfactorily. In the laser used this 'warming-up' time was generally of the order of one and a half to two hours. When the laser has reached thermal stabilization the power output was stable to within

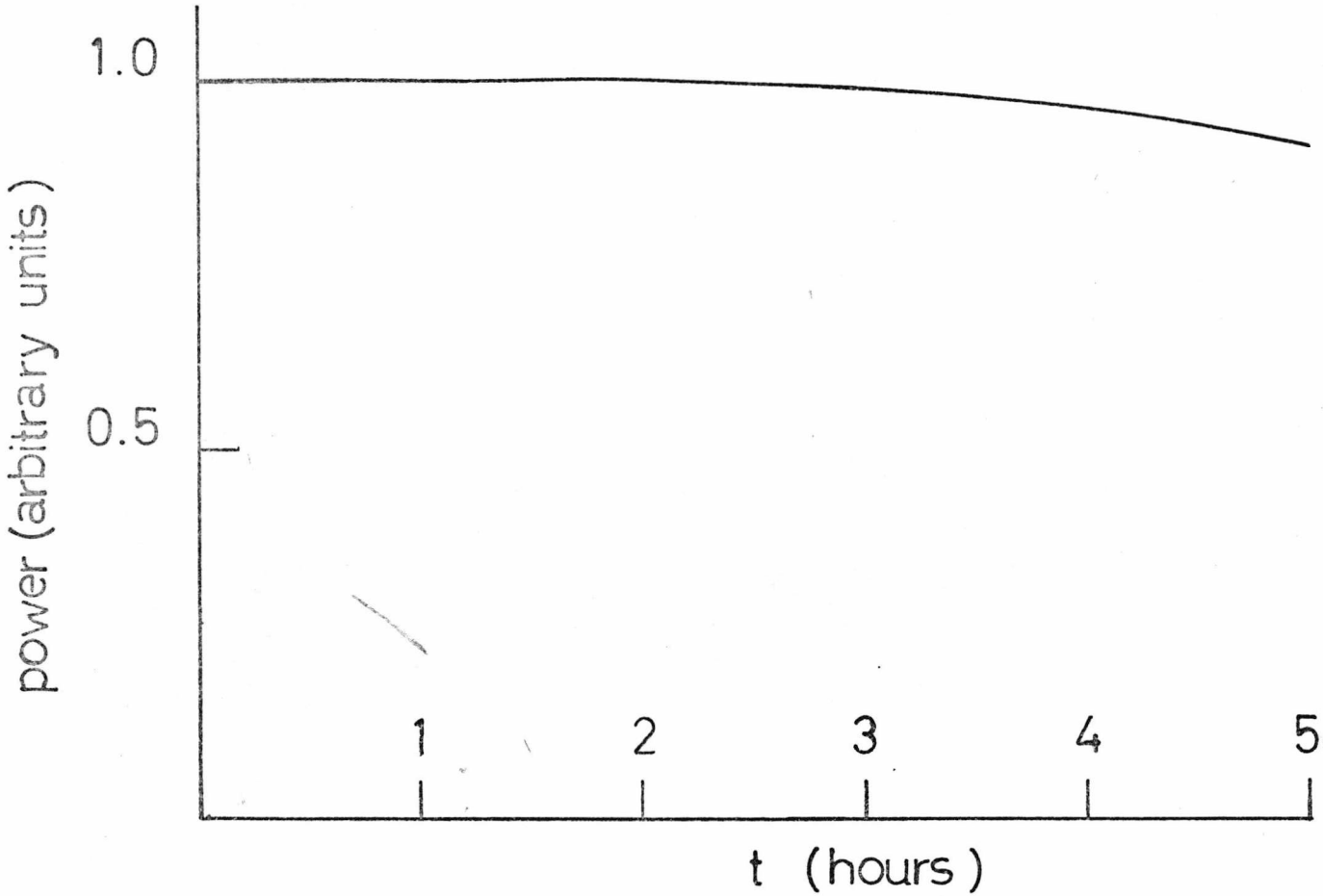


Figure 4.5: The stability of the laser power output.

± 10% for periods of four hours or more, as shown in Figure (4.5). This period is long enough compared with the measuring time that the laser power is effectively constant throughout the recording of a spectrum. This is borne out by the observation of constant intensities of the successive transmission peaks in the recorded spectrum, when the interferometer was scanned through up to 5 free spectral ranges. Further, since we did not measure the absolute intensities of the scattered light, this stability was adequate for our purposes.

4.2.4. Frequency Stability

The frequency stability of the laser can be classified into short term stability and long term stability. We define short term stability as the stability in terms of a time interval less than the resolving time of the instrument (effectively the time to scan the bandwidth). So we can write the short term stability as:

$$S_f(t) = \frac{f}{\Delta f(t)} \qquad t < \tau \qquad (4.1)$$

where $\tau$ is the 'resolving time' of the instrument, which in our case was of the order of 15 - 30 sec. Thus by this definition the short term stability is the effective band width of the laser output.

For the laser used in the experiments, the short term frequency stability, according to the manufacturers' specification, is better than 1 part in $10^8$. This implies that the bandwidth of the laser output is of the order of

$10^7$ Hz. This figure is somewhat smaller than the transmission halfwidth of our FP interferometers (as discussed in sections 4.3 and 4.4).

Long term stability can be defined as:

$$S_f(t) = \frac{\bar{f}}{\Delta f(t)} \qquad t > \tau \qquad (4.2)$$

where $\bar{f}$ is the mean frequency and $\Delta f(t)$ is the spread of frequencies during the time of measurement. Long term stability is not limited by the resolving time of the instrument. In this case we choose the time it takes to measure and record a spectrum ($\sim$ 30 mins.) as the period defining the long term stability of the laser frequency.

Long term stability is governed by macroscopic changes in the system, mainly thermal relaxation of mechanical parts. Hence the long term frequency stability (like the power stability) could only be assessed when the laser has reached thermal equilibrium.

In this work the long term frequency stability of the laser was assessed using the interferometer. This being the case it cannot be separated from the long term stability and the linearity of the frequency sweep of the interferometer, so this will be dealt with in more detail when describing the interferometers in the following section.

## 4.3. The Pressure Scanned Plane Fabry Perot (FPP) Interferometer

### 4.3.1. Theory of Operation of the FPP

The FPP interferometer is described in many text books on geometrical optics (3). It is an angular filter which consists of two high quality plane mirrors arranged with the mirror faces parallel to each other as shown in Figure (4.6). Analysis of the path of a ray intersecting the mirror at an angle $\theta$, shows that the phase difference $\phi$ between successive transmitted beams is given by (3):

$$\phi = \frac{2\pi}{\lambda} (2nd \cos \theta) + 2\pi \qquad (4.3)$$

where n is the refractive index of the medium between the mirrors, d is the mirror separation and $\lambda$ is the wavelength of the incident light. The ratio, M, of the intensity

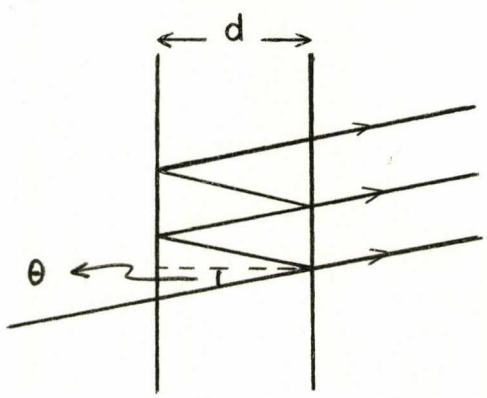


Figure 4.6: Schematic Diagram of an FPP

of the transmitted light to the incident intensity is given by

$$M = \frac{T^2}{(1-R)^2} \cdot \frac{1}{1 + F\sin^2(\phi/2)} \qquad (4.4)$$

where T and R are the transmission coefficient and reflectivity of the mirrors respectively, and F is the factor:

$$F = \frac{4R}{(1 - R)^2} \qquad (4.5)$$

From (4.4) we see that the transmitted intensity is periodic in $(\phi/2)$ and the separation between adjacent maxima in the transmission pattern is called the interorder spacing or the free spectral range (FSR). The halfwidth $\Delta p$ (full width at half maximum) of the transmitted intensity is given by:

$$\Delta p = \frac{2}{\pi\sqrt{F}} \times \text{FSR} \qquad (4.6)$$

This is the reflectivity halfwidth. The ratio of the FSR to the halfwidth of the transmission intensity is called the Finesse. Thus from (4.6) the reflectivity finesse $F_R$ of the FPP is simply given by

$$F_R = \frac{\pi\sqrt{F}}{2} \qquad (4.7)$$

In practice the finesse obtained is lower than the reflectivity finesse, $F_R$. This is because the transmission halfwidth depends on the flatness of the mirror surfaces

(the mirror surface number), the mirror losses and the parallelism of the mirror as well as the mirror reflectivity. Modern high precision engineering makes it possible to produce mirrors flat to $\lambda/200$. Absorption in the mirrors is minimized using multilayer dielectric coating (4). Experimentally the most important factor governing the instrumental linewidth is the prallelism of the mirror surfaces. This limits the working finesse to <100. The instrumental working finesse is defined as:

$$F_I = \frac{FSR}{\Delta f} \qquad (4.8)$$

where $\Delta f$ is the instrumental linewidth.

In our experiments it was necessary to use FPP's with different mirror separations. These were 30.07 mm and 50.01 mm, corresponding to FSRs of 4.985 GHz and 2.997 GHz respectively. The mirror spacers are made of quartz cylinders machined to $\lambda/50$ by Imperial College Optical Systems Company, and the mirrors and spacer are held together in a brass mounting. The mirror plates are pressed onto the spacer with spring loaded feet and screws. The brass mounting is shown schematically in Figure (4.7).

In our experimental set-up the FPP is set normal to the incident beam ($\theta = 0$ in equation 4.3) and the instrument is used in the 'central spot scanning' mode. The FSR of the instrument, in frequency, is then given by:

$$FSR = \frac{c}{2nd} \qquad (4.9)$$

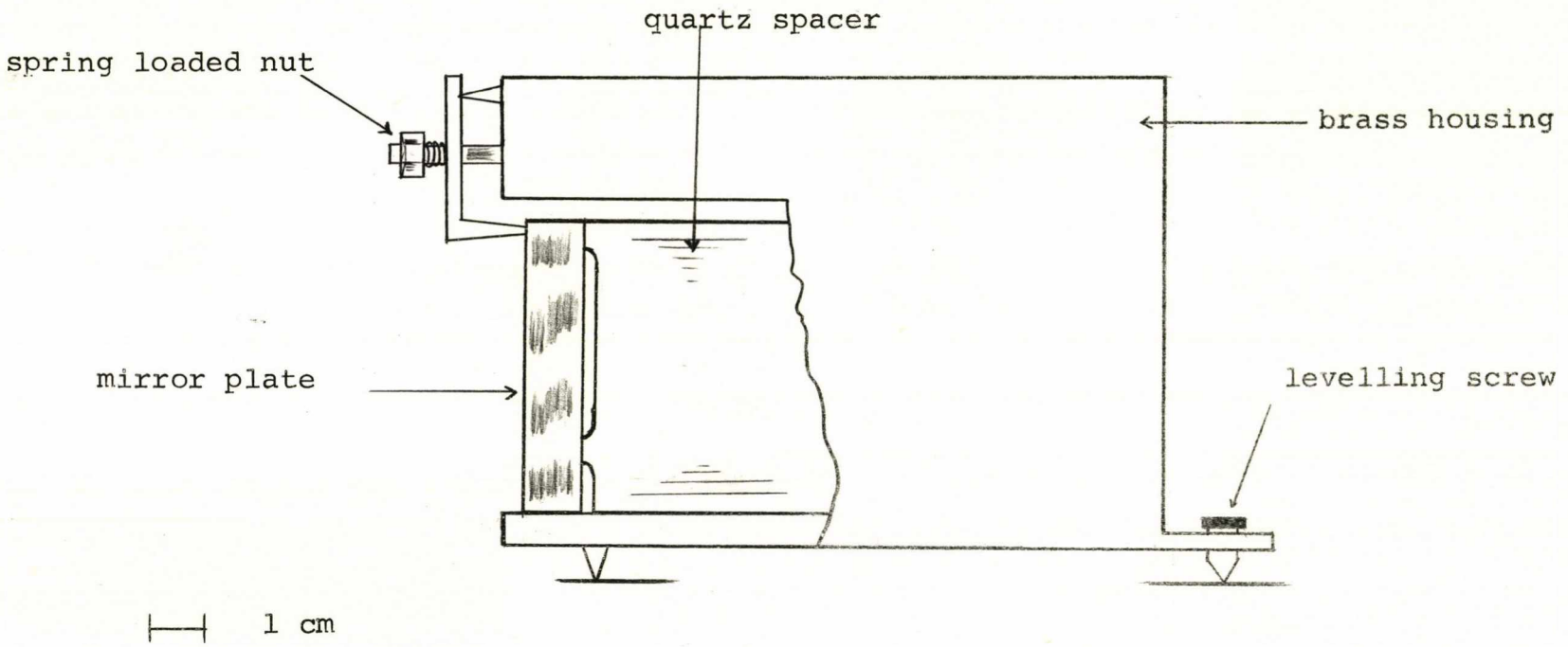


Figure 4.7: Exploded view of FPP etalon mounting

The FPP is used as an optical filter by sweeping its transmission peaks (n or d could be varied) and measuring the transmitted light intensity as a function of frequency. If the light source analysed is monochromatic the transmitted intensity will be just the instrumental profile given by equation (4.4). If the source has a spectral distribution G(f) the transmitted intensity will be the convolution of G(f) with the instrumental profile, M(f). Thus the transmitted intensity will then be given by:

$$I(f) \propto M(f) \otimes G(f) \qquad (4.10)$$

where $\otimes$ indicates convolution.

4.3.2. Pressure Scanning and Linearity

The resonant frequencies of the FPP are swept by changing the refractive index n of the gas in the cavity. This is achieved by changing the pressure of the gas. Writing $n-1 = \alpha P$ where P is the pressure of the gas and $\alpha$ is a proportionality constant we find

$$\frac{\Delta fN}{\Delta P} = - \alpha fN \qquad (4.11)$$

For air $\alpha = 3.84 \times 10^{-7}$/mm (5), and for $\lambda = 5145\text{Å}$ we have

$$\frac{\Delta fN}{\Delta P} = 0.224 \text{ GHz/mm} \qquad (4.12)$$

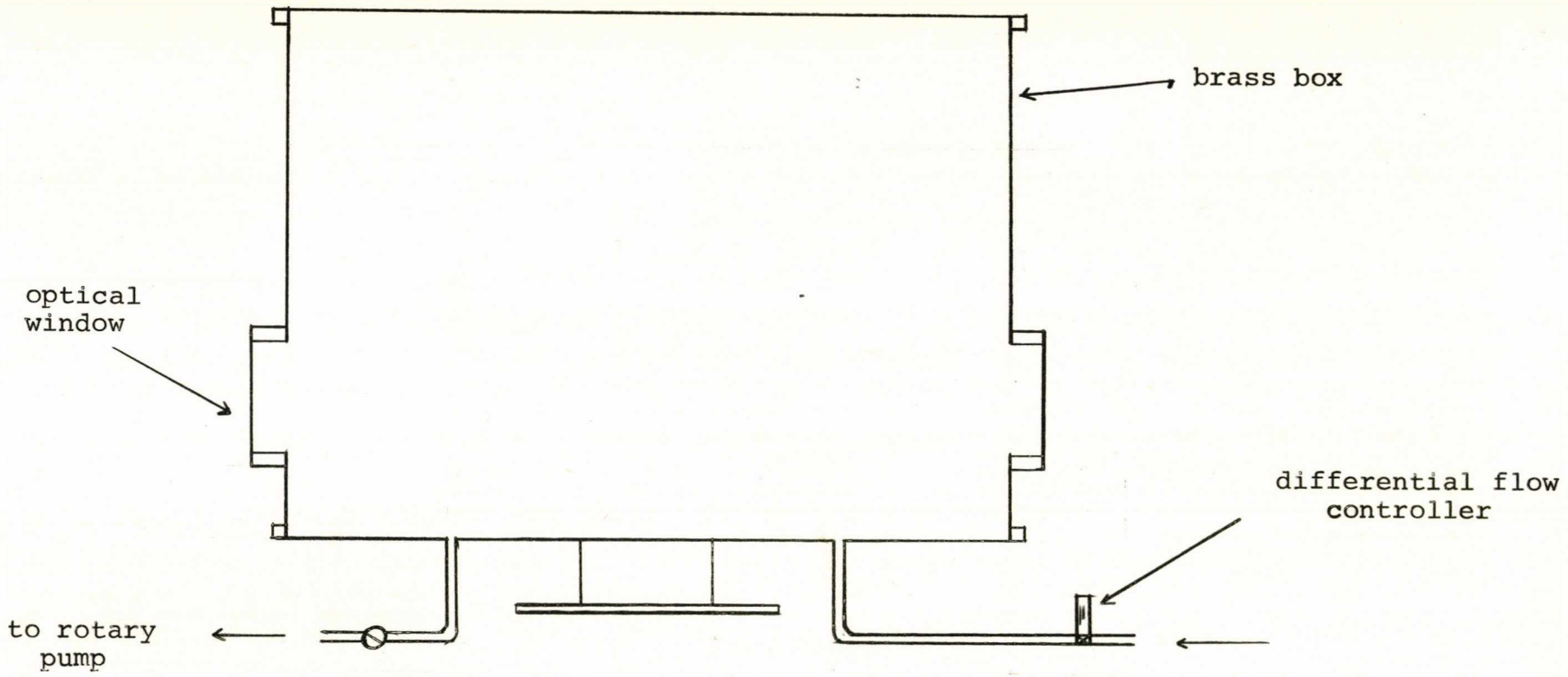


Figure 4.8: Vacuum chamber for the FPP

Figure 4.8: Access road for the new substation

Thus a FSR of 5 GHz is swept with a pressure change of $\Delta P \simeq 22.4$ mm at constant temperature.

Temperature variations in the gas and the parts of the FPP will cause the resonant frequency to fluctuate and drift. These fluctuations and drifts in the FPP combined with the long term frequency instability of the laser (as described in section 4.2.4.) will give rise to inaccuracies in the measurement of frequencies. We will now consider how these instabilities and drifts affect the accuracy of our measurements.

The pressure scanning system is shown schematically in Figure (4.8). It consists of an air-tight brass chamber with two connecting tubes, one for evacuation and the other for gas/air inlet. Optical windows on opposite sides are sealed with neoprene O-ring seals. The total capacity of the vacuum chamber is about 3.5 l. The inlet gas flow is set and controlled with a differential pressure flow controller supplied by Emerson Electrical Co., Hatfield, Pensylvania.

In operation, the vacuum chamber is evacuated and the FPP transmission peaks are swept by allowing air to flow into the chamber through the flow controller, thus changing the refractive index of the medium in the FPP cavity. The rate of air inflow can be set by opening the flow controller to the required controller setting. The relationship between the flow controller setting and the rate of frequency scanning is shown in Figure (4.9) for $\lambda = 5145\text{Å}$. For $\lambda = 4880\text{Å}$ the rate shown on the graph should be multiplied by 1.05.

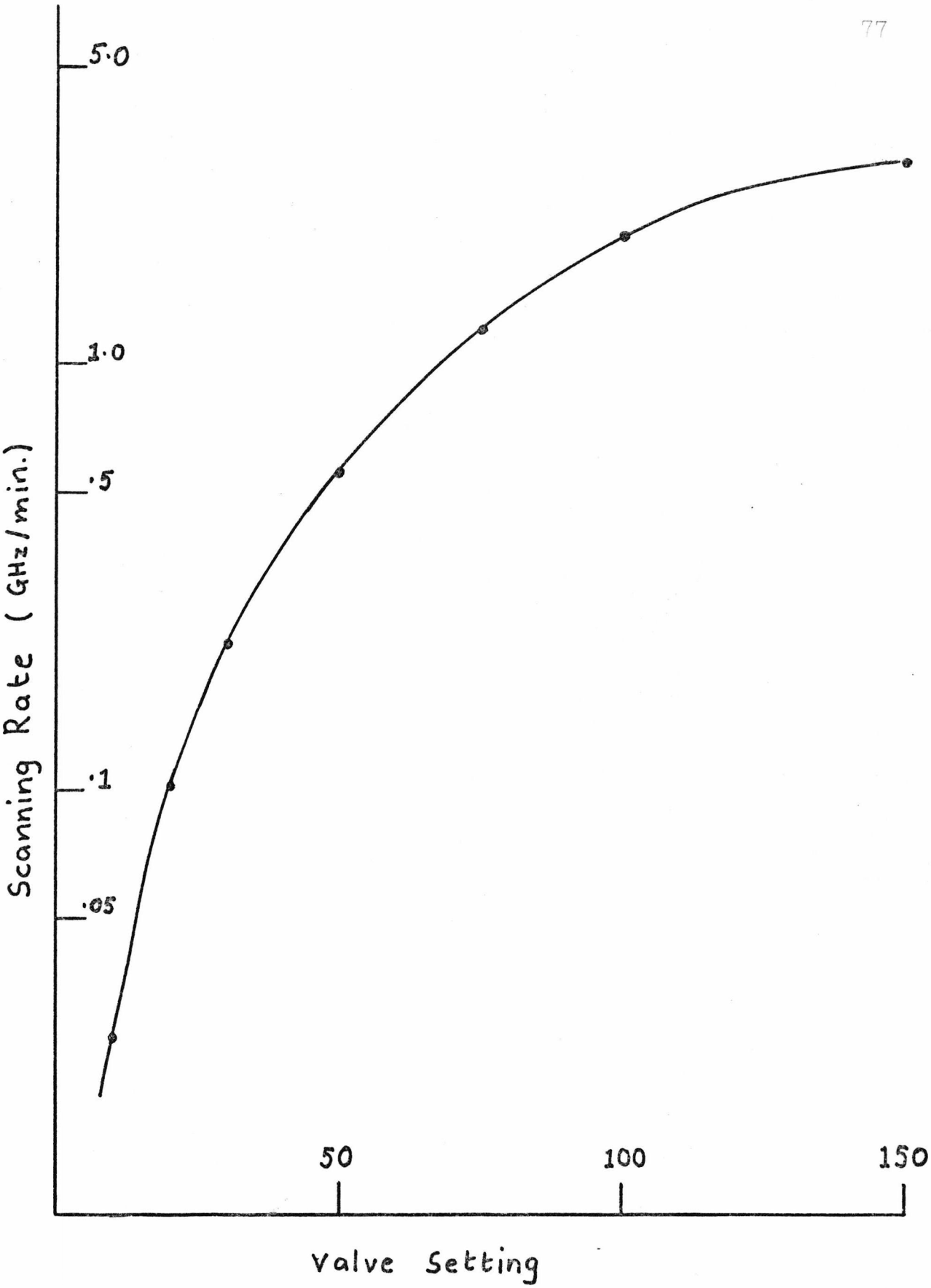


Figure 4.9: The pressure scanning rate as a function of valve setting. (flowvalve characteristic).

The linearity of the frequency sweep is tested by scanning the transmission peaks of the FPP for a monochromatic source and plotting the transmitted intensity as a function of time (effectively frequency) on an x - t chart recorder. The positions of the intensity peaks mark the frequencies (in units of the FSR) along the chart and the variation of the separation of successive adjacent peaks indicates the nonlinearity of the frequency scan. This result is shown in Figure (4.10) where $\Delta X_n$ is the distance along the chart of the interorder spacing of the peaks $n_p$ along the chart. It is found that there is no systematic drift in the interorder spacings when the FPP is swept up to 10 orders. In this case it is meaningful to take the mean $\overline{\Delta X}_n$ of the interorder spacings and calculate the accuracy of our measurements in terms of the standard deviation of the scatter of $\Delta X_n$ about this mean. The standard deviation of $\Delta X_n$ about $\overline{\Delta X}_n$ is $\pm$ 0.17%. Also the scatter of $\Delta X_n$ was found to be independent of the scanning rate for the rates of scanning used in the experiments. Because of this scatter in $\Delta X_n$ the accuracy of our measurements is affected to the extent that for a free spectral range of 3 GHz we have an ambiguity of about 5 MHz and for a free spectral range of 5 GHz the ambiguity is about 8.5 MHz.

The scatter in $\Delta X_n$, the interorder spacing of the frequency sweep, can be attributed to the long term laser frequency drifts, temperature fluctuations in the FPP and the small temperature changes in the air in the vacuum

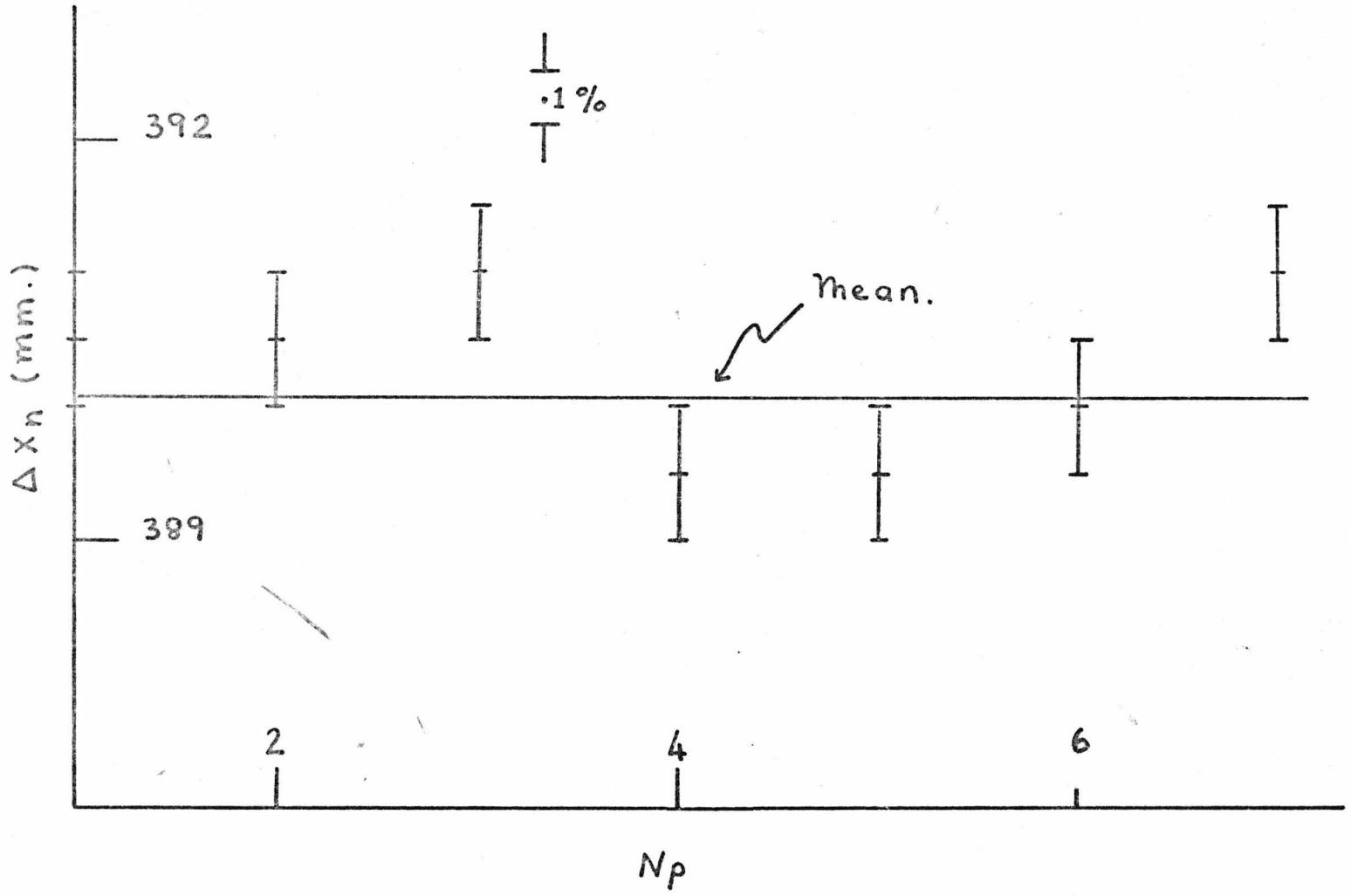


Figure 4.10: Linearity of the FPP frequency sweep.

chamber. The error introduced into our measurements of frequency due to these fluctuations is ± 0.17%.

4.3.3. Instrumental Profiles and Finesse

The instrumental profiles of the interferometers were obtained by scattering light off a solution of colloidal silica (Ludox ) in water. The scattering geometry and especially the optical collection arrangement was the same as in the actual experiment. This was done so that the instrumental profiles were taken with the same distribution of light in the interferometers as in the experiments.

The transmission function of the FPP is shown in Figure (4.11) and the instrumental profile in Figure (4.12). The instrumental profile was observably non-Lorentzian. In order to be able to use an analytic function for the numerical convolution of the theoretical spectrum, $S(K, \omega)$, with the instrumental function, $M(\omega)$, a least squares fit of the instrumental profile to a function of the form $(L(\omega))^n$ where $L(\omega)$ is a Lorentzian centered at $\omega = 0$ and $1.0 < n < 2.0$ was obtained. The best fit was found for $n = 1.40$.

The finesse of the FPP was measured from the recorded transmission functions. The working instrumental finesse of both interferometers was found to be 49, corresponding to instrumental line widths of 61 MHz and 102 MHz for free spectral ranges of 2.997 GHz and 4.985 GHz respectively. The characteristics of the FPP interferometers are listed in table (4.1).

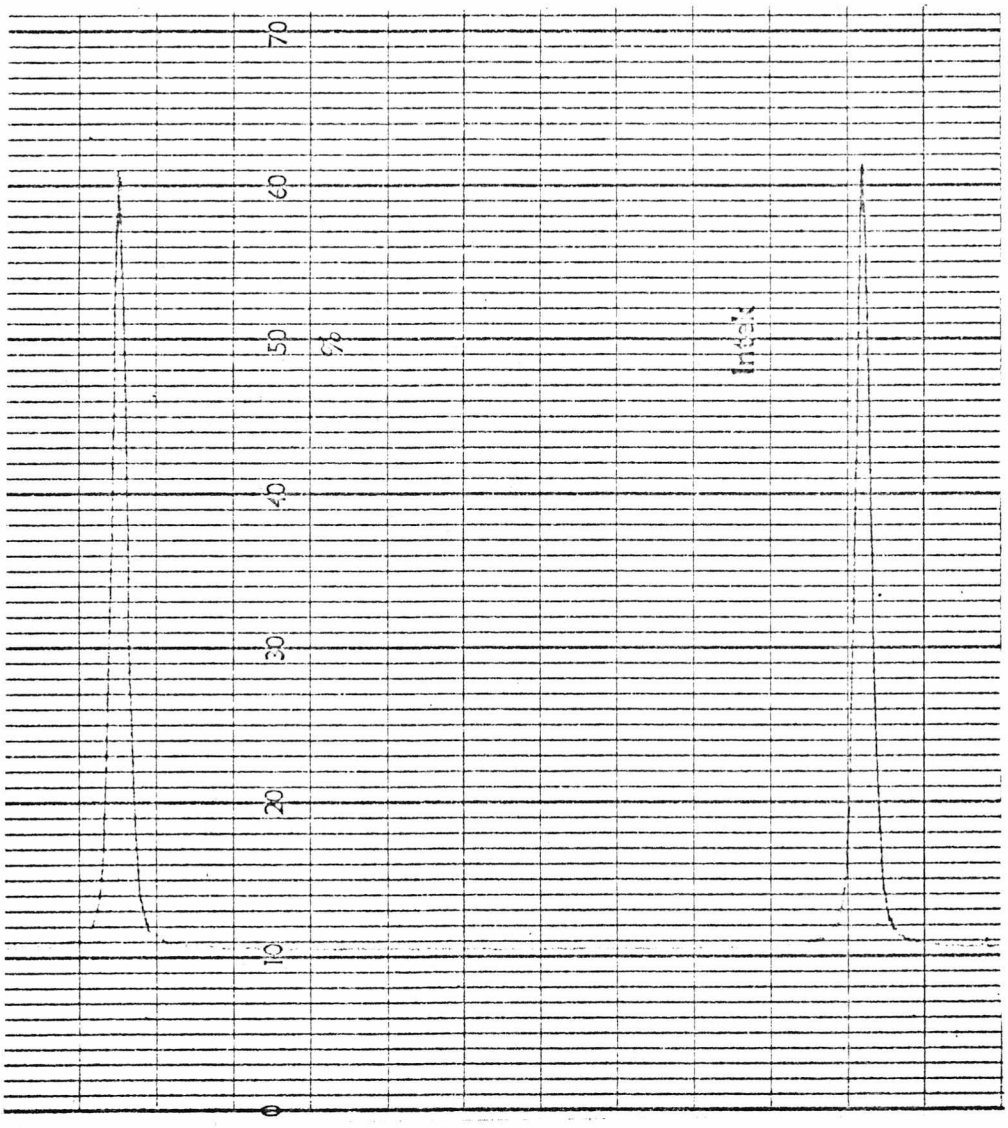


Figure 4.11: Transmission function of the FPP.

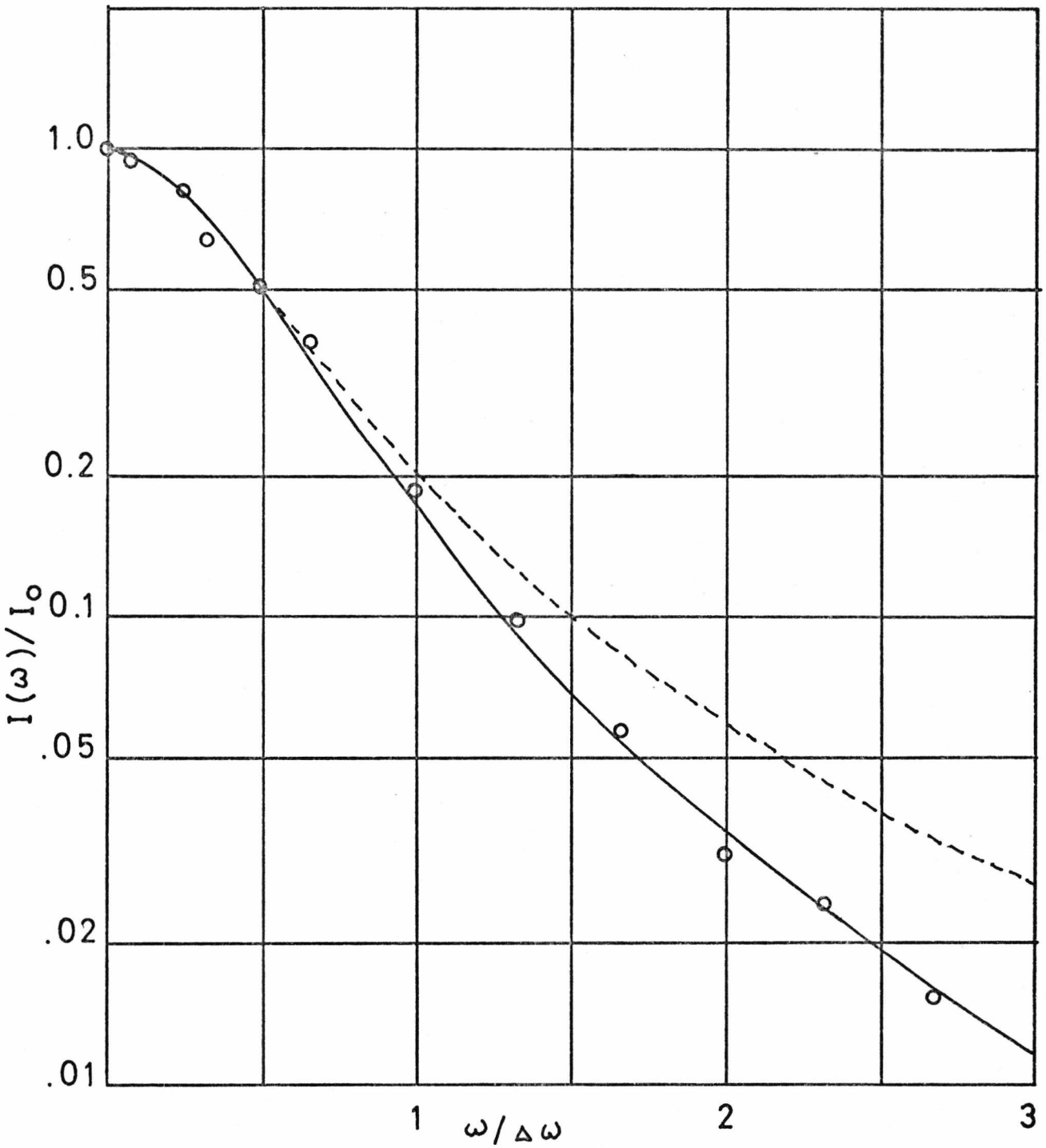


Figure 4.12: Transmission profile of the FPP: dashed curve is Lorentzian, smooth curve is $(L)^{1.40}$.

Table 4.1: Characteristics of the FPP Interferometers

| Spacer (mm) | FSR (GHz) | $\Delta f$ (MHz) | $F_I$ |
|---|---|---|---|
| 30.07 | 4.985 | 102 | 49 |
| 50.01 | 2.997 | 61 | 49 |

## 4.4. The Confocal Spherical Fabry-Perot (FPS) Interferometer

### 4.4.1. Introduction

The FPP's discussed in the previous section have a highly linear frequency sweep which makes them ideal for absolute frequency determination. However, the linewidths of the transmission functions of these inteferometers are $\gtrsim$ the linewidths of the spectral components in the scattered light from the liquids. Consequently it is difficult to extract accurate linewidth data from the

spectra obtained using these interferometers. To overcome this problem we have used a confocal spherical Fabry-Perot (FPS) interferometer.

4.4.2. The Operation of the FPS

The FPS is a resonant cavity (6) comprised of two identical high quality spherical mirrors confocally arranged, i.e. the mirrors are separated by a distance equal to their radius of curvature, as shown in Figure (4.13).

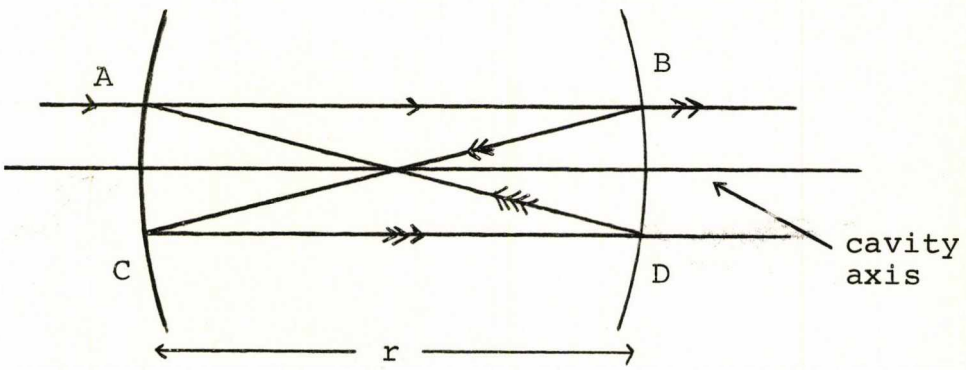


Figure 4.13: Schematic diagram of Confocal FPS

Paraxial rays incident on the cavity at A (Figure 4.13) are internally reflected in the cavity along the path B C D A B and retrace their initial path after traversing the cavity four times. Multiple interference is therefore produced in the transmitted light. The path length P after reflection in the cavity four times is $P = 4nr$, where r is the radius of curvature of the mirrors and n is the index of refraction of the medium between the mirrors.

Constructive interference in the transmitted light occurs for wavelengths $\lambda_N$ given by

$$\lambda_N = \frac{4nr}{N} \qquad N = 1, 2, 3 \ldots. \tag{4.13}$$

and the corresponding resonant frequencies are given by

$$f_N = \frac{Nc}{4nr} \tag{4.14}$$

The free spectral range (FSR) of the instrument is defined as the spacing in frequency between adjacent resonances and is given by:

$$FSR = f_{N+1} - f_N = \frac{c}{4nr} \tag{4.15}$$

The full width at half maximum of the transmitted intensity is given by (7):

$$\Delta f_R = \frac{c}{4\pi nRr} (1 - R^2) \tag{4.16}$$

From (4.15) and (4.16) we find that the reflectivity finesse $F_R$ is given by:

$$F_R = \frac{\pi R}{(1-R^2)} \tag{4.17}$$

In practice the instrumental profile of the FPS is determined by a number of factors. These include mirror reflectivity, mirror surface figure, mirror losses, spherical

aberration, mirror alignment and the aperture of the instrument.

The instrumental lineshape is affected most by spherical aberration and the size of the aperture of the FPS. Spherical aberration affects the lineshape by introducing a distribution of resonant frequencies $f_N$ over the area of the FPS, thus smearing out the transmission peak.

The effect of the aperture can be seen by considering the path length of a ray intersecting the mirror at a distance **x** from the FPS axis. The difference in the path length of a nonparaxial ray from 4nr (the paraxial path length) is (8)

$$\Delta P(x) \simeq \frac{x^4}{r^3} \tag{4.18}$$

Hence

$$\frac{\Delta P(x)}{P} = \frac{x^4}{4r^4} \tag{4.19}$$

This produces a deviation $\Delta f$ of the resonant frequency $f_N$:

$$\Delta f = f_N\left(\frac{x^4}{4r^4}\right) \tag{4.20}$$

To keep the deviation or spread of resonant frequencies $\Delta f$ small compared with the reflectivity halfwidth, $\Delta f_R = FSR/F_R$, we find the condition:

$$f_N\left(\frac{x^4}{4r^4}\right) < \frac{FSR}{FR}$$

or

$$x < r\left(\frac{\lambda}{rF_R}\right)^{\frac{1}{4}} \qquad (4.21)$$

This limitation on the size of the aperture limits the light gathering ability of the FPS. In practice the aperture of the FPS is much larger than the limit given by equation (4.21) in order to ensure reasonable signal collection.

The FPS has the advantage that it is easy to align and is extremely stable. Furthermore it is considerably easier with the FPS to obtain an instrumental finesse approaching the reflectivity finesse. The instrument could be operated with a finesse > 100; even with an aperture > than that set by (4.21) (the condition for optimum finesse).

### 4.4.3. Piezo electric Scanning and Linearity

The FPS used in the experiment was a commercially available coherent Optics Inc. model 470, with a FSR of 2.000 GHz. The resonant frequencies of the FPS were swept by changing the mirror spacing, d. This was achieved by mounting the mirrors on a ceramic cylinder and applying a linearly increasing (or decreasing) voltage to the ceramic cylinder. The spacing d could be varied over a region of $\sim 5\lambda$ about $d = r$ without any observable influence on the profile of the transmission function.

The rate of change of the frequencies with change in spacing, $\Delta d$, is given by:

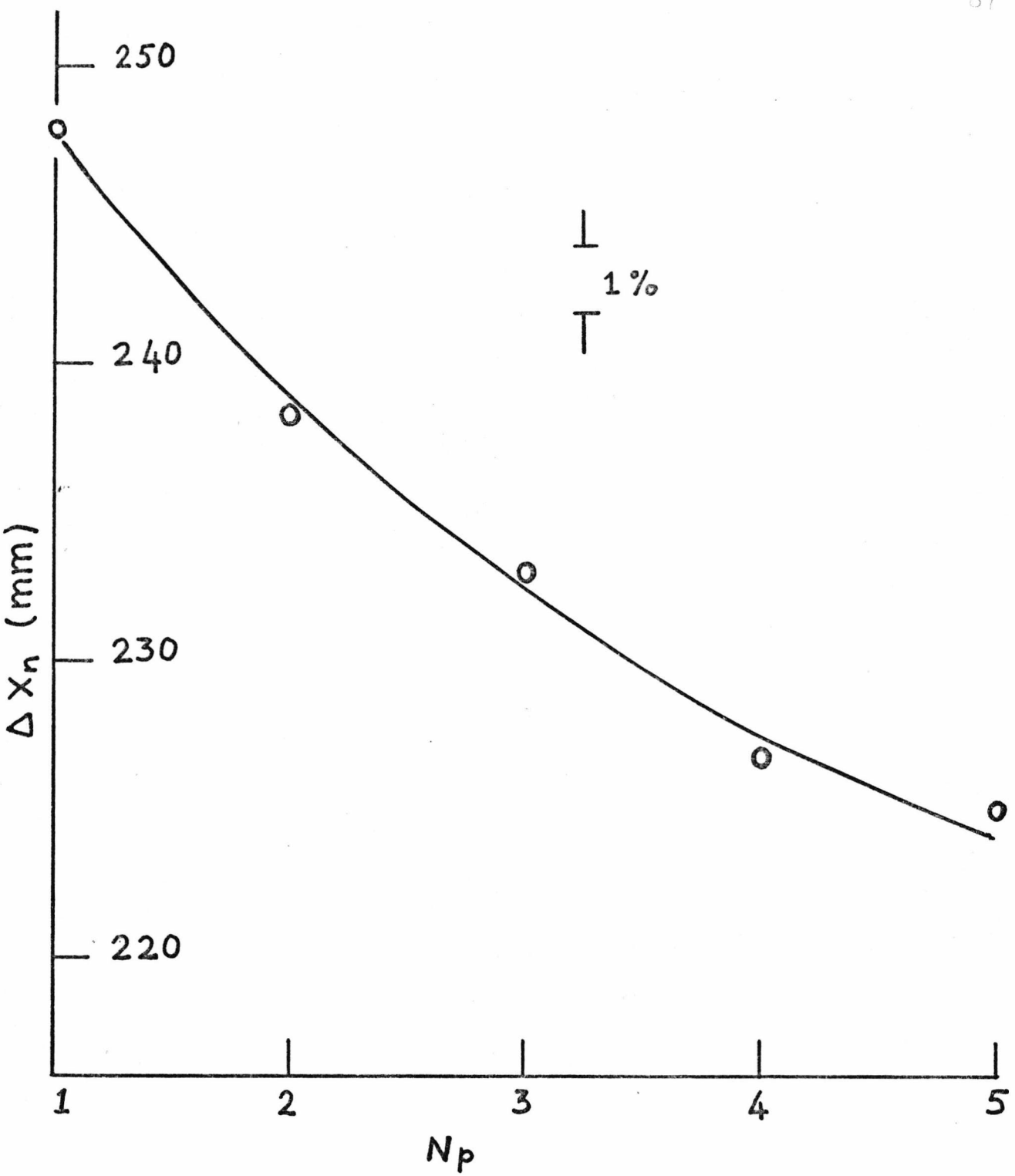


Figure 4.14: Confocal FPS sweep dispersion curve.

$$\Delta f_N = - \frac{FSR}{(\lambda/4)} \Delta d \qquad (4.22)$$

This means that a free spectral range is scanned for every $\lambda/4$ change in mirror spacing.

In our experiment the linearly increasing voltage used to sweep the resonant frequencies of the FPS was obtained from the ramp output of a Tektronix 531A oscilloscope. The sweep rate used during the measurement of a spectrum was generally of the order of three minutes per FSR.

The frequency sweep characteristics of the FPS is shown in Figure (4.14). This shows a dispersion of the interorder spacing, indicating a non-linear variation of the mirror separation with the applied voltage. However, since the FPS was used only for the measurement of the width of the Brillouin lines the effect of this dispersion is relatively small in absolute terms. This is because the frequency change $\Delta\omega$, across the width of the line is small and the errors in absolute frequency measurement introduced by the nonlinearity is proportional to $\Delta\omega_B/FSR$. (If the FPS were used for measuring the Brillouin shifts, $\omega_B$, the absolute error would be an order of magnitude greater since $\omega_B \gtrsim 10\Delta\omega_B$).

The transmission function of the FPS is shown in Figure (4.15). (A comparison of Figure (4.15) with Figure (4.11) gives an idea of the higher finesse that could be obtained with the FPS). The instrumental profile of the FPS fitted to a function of the form $(L(\omega))^n$, where

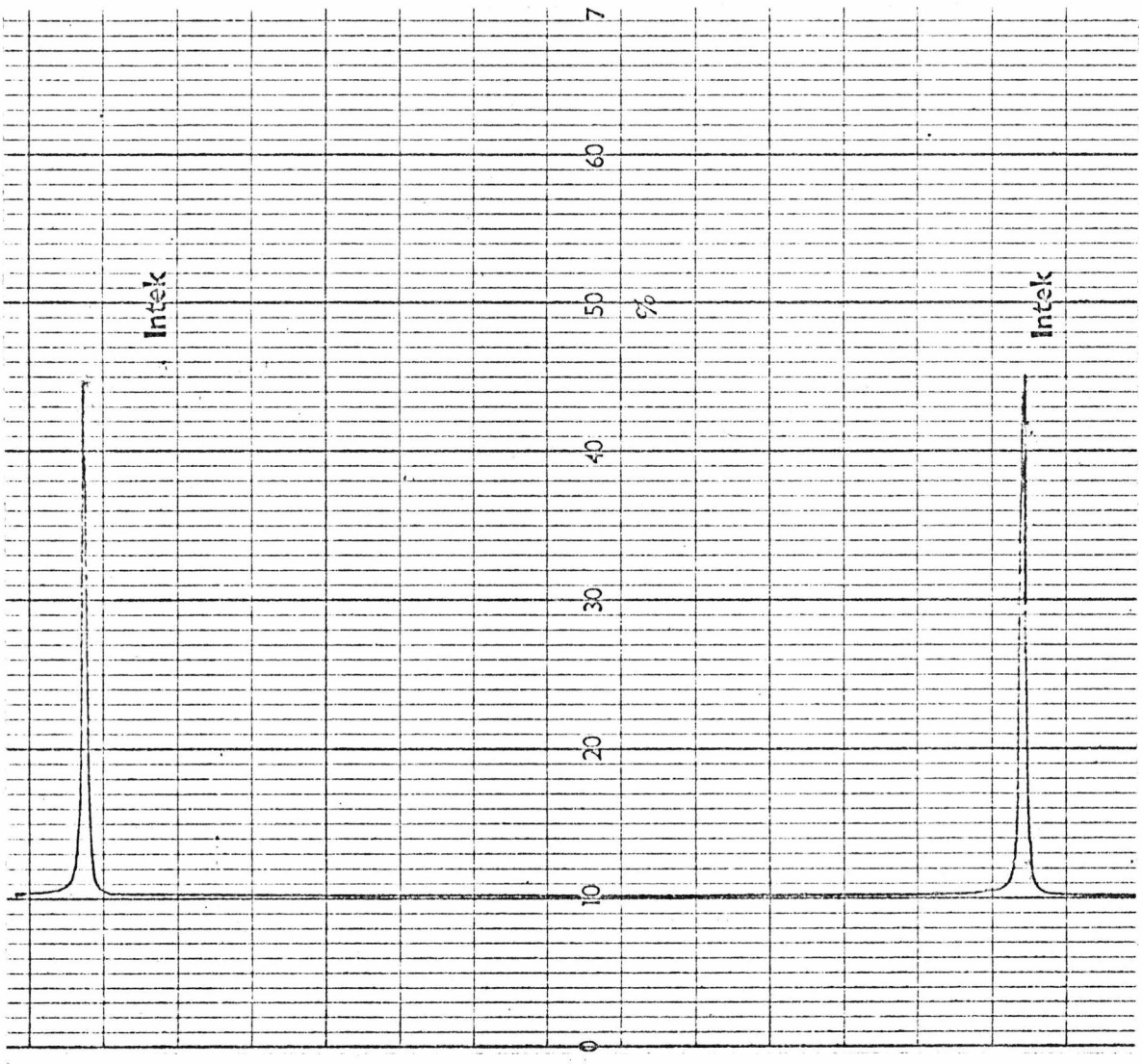


Figure 4.15: Transmission function of the FPS.

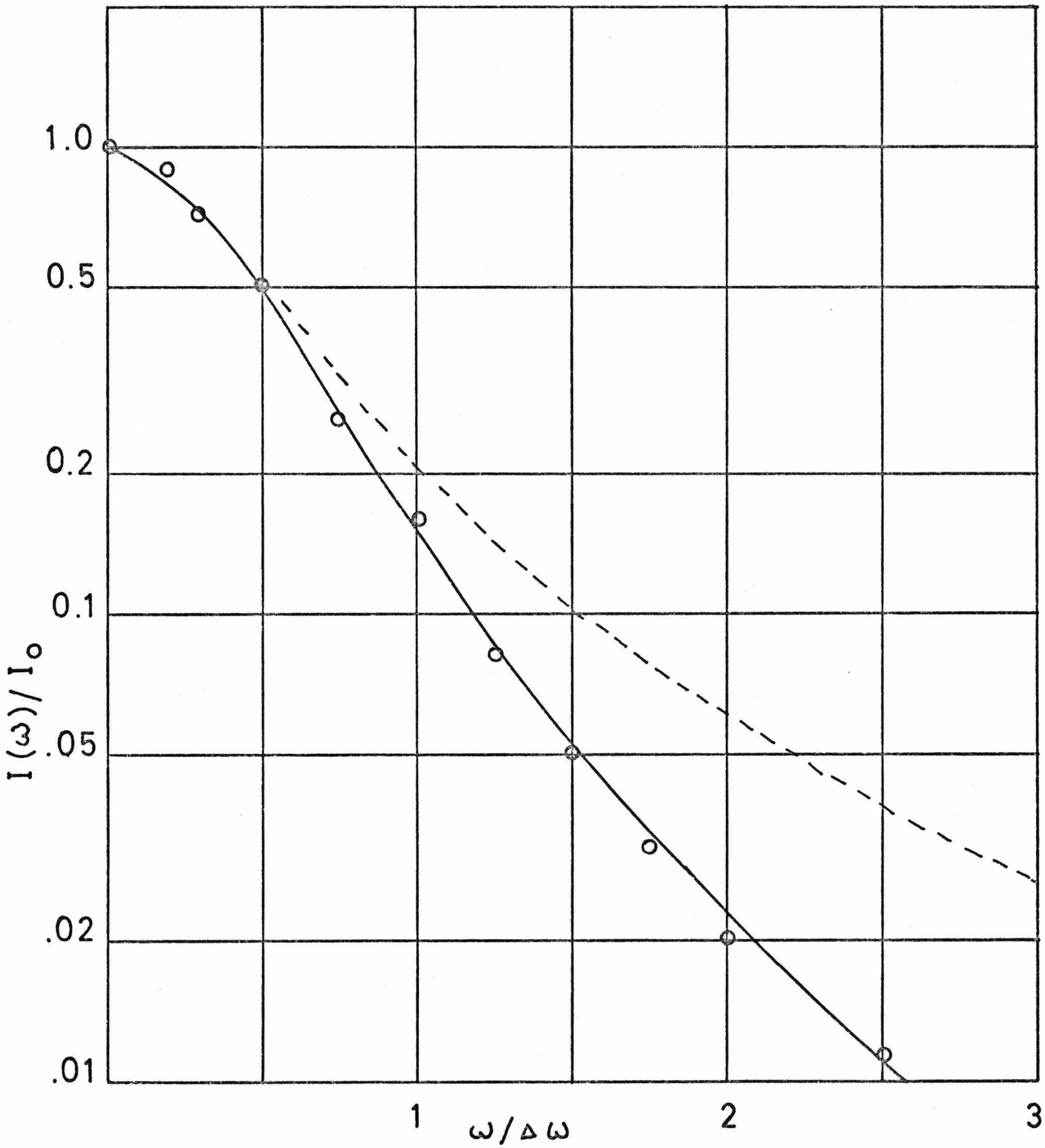


Figure 4.16: Transmission profile of the FPS: dashed curve is Lorentzian, smooth curve is $(L)^{1.75}$.

$L(\omega)$ is a Lorentzian centered at $\omega = 0$, is shown in Figure (4.16). The best value of n was found to be 1.75.

The characteristics of the FPS are listed in Table (4.2)

Table 4.2: Confocal FPS Parameters

| FSR (GHz) | $\Delta f$ (MHz) | $F_I$ | Aperture (mm) |
|---|---|---|---|
| 2.000 | 17.75 | 112 | 2 |

## 4.5. Light Detection System

### 4.5.1. Detection Techniques

The photons which arrive at the photomultiplier cathode produce current pulses at the anode with a distribution in magnitude due to the statistical nature of the amplification process. This output current can be measured in either of two ways:

(a) D.C. Detection. Here the integration time of the anode circuit is long so that the average current can be measured, by measuring the voltage developed

across a known resistor. This can be perfomed by using a d-c meter.

(b) Photon Counting. In this technique the integration time is short such that discrete pulses corresponding to the detection of each photon are produced. The output pulses of the PMT are standardized with a discriminator and then can eitherbe converted to d.c.voltage (representing the average counting rate) or stored in digital form.

A photon counting system is more efficient than a d.c.detection system because in a photon counting system the signal to noise ratio can be optimised by setting the discriminator level appropriately. This cannot be achieved with a d.c.detection system. Also with a photon counting system the data can be digitized. Hence the ease with which computer analysis of data may be made is greatly enhanced.

In this work a photon counting system was used because of the advantages mentioned above. In the following we outline the operation of this system.

### 4.5.2. The Photon Counting System

The photon counting system used to detect the light transmitted by the interferometers is shown schematically in Figure (4.2). The PMT was an EMI 6256 SA with a 10 mm diameter $Cs_3Sb$ cathode. In practice the optics of the

system governed the size of the cathode area utilised, which in this work was a diameter < 0.5 mm. The PMT dark current, when the discriminator level was set to accept ∿ 90% of the amplified pulses from the photoelectron emission, was 25 cts/S (counts/second). This could be reduced to ∿ 3 cts/S when the PMT was cooled to ∿ $0^{o}C$ by passing dry cold air through the PMT housing. Cooling the PMT is advantageous when the light signal is weak, as in the case of the gas mixtures where the signal was typically ∿ 300 cts/S. Thus cooling the PMT increased the signal to noise ratio (S/N) from ∿ 3.5 to ∿ 10.

To record a spectrum the output of the detection system is recorded as the interferometer is scanned in time.

### 4.5.3. The Recorded Spectrum

The signal from the PMT contains noise due to the statistical nature of the photoelectron emission. This statistical noise affects the signal to noise ratio (S/N), and hence the accuracy of the measurement. The S/N could be improved by introducing an RC filter into the system, thus integrating over a large period and 'smoothing' out the noise. (The RC filter was the ratemeter time constant).

The output current of the photon counting system is a sum of pulses of constant charge. The duration of these pulses is short compared with the duration of the impulse response, h(t), of the filter system. Writing the output of the PMT as $N_i(t)$ and the resultant output of

the filter system as $N_0(t)$ we have the input-output relation given by (9, 10):

$$N_0(t) = \int_{-\infty}^{\infty} h(\tau)\, N_i(t-\tau)\, d\tau \tag{4.23}$$

For the photoelectron emission process the autocorelation function, $C_0(t)$, of the output of the filter system is given by (11):

$$C_0(\tau) = \left[\bar{N} \int_{-\infty}^{\infty} h(t)dt\right]^2 + \bar{N} \int_{-\infty}^{\infty} h(t)\, h(t+\tau)\, dt \tag{4.24}$$

where $\bar{N}$ is the average rate of pulses.

Assuming the impulse response of the filter, $h(t)$, is that of an ideal filter, we have

$$h(t) = \begin{cases} \frac{1}{T} e^{-t/T} & t > 0 \\ 0 & t < 0 \end{cases} \tag{4.25}$$

where T is the filter time constant.

Using (4.25) in (4.24) we obtain the power spectrum of the system output as:

$$S_{\bar{N}}(\omega) = \bar{N}^2 (2\pi)^{\frac{1}{2}} \delta(\omega) + \frac{\bar{N}}{(2\pi)^{\frac{1}{2}}} \frac{(\frac{1}{T})^2}{(\frac{1}{T})^2+\omega^2} \tag{4.26}$$

which consists of a d.c. (signal) part which is proportional to $\bar{N}^2$ and a noise part which is a Lorentzian with

halfwidth $(\frac{1}{T})$. The signal to noise ratio (S/N) is the square root of the ratio of the integrated power:

$$S/N = \left(\frac{P_S}{P_N}\right)^{\frac{1}{2}} \tag{4.27}$$

where $P_S$ and $P_N$ are the integrated signal and noise power (from 4.26) respectively.

Integrating the two parts of (4.26) we find

$$S/N = (2\bar{N}T)^{\frac{1}{2}} \tag{4.28}$$

From (4.28) we see that the detectability of the signal is determined by the average count rate $\bar{N}$ and the system time constant, T. The S/N will vary with the transmitted light frequency since the average count rate is a function of the spectral information.

The choice of the value of the time constant T is important because the recorded spectrum, $S_R(t)$, is a convolution of the actual output current of the system, $S_i(t)$ with the filter response function, h(t):

$$S_R(t) = S_i(t) \circledast h(t) = \int_0^\infty d\tau S_i(t-\tau)h(\tau) \tag{4.29}$$

Thus in choosing the time constant T we have to compromise the signal to noise ratio against the distortion of the spectrum, given by (4.29). Experimentally it is found that the optimum value of T is given by:

$$T < \frac{1}{10} \times (\text{line halfwidth})/(\text{Scan rate}) \qquad (4.30)$$

This gives the upper limit of the value of T.

## 4.6. The Sample Holding System

### 4.6.1. Introduction

The experiments on the rare gas liquids required a cryostat which would satisfy several requirements. These requirements are:

(1) Large adjustable range of temperatures; the temperature range covered by the experiment was approximately from 85°K to room temperature,

(2) the temperature must be kept stable to $\lesssim \pm$ 0.05°K for long periods (hours),

(3) preferably with a large coolant capacity since each experiment takes several weeks to complete;

(4) the sample must be accessible for light scattering experiments, and

(5) it must be possible to move the cryostat into and out of the scattering region easily. This was necessary for:

   (a) setting up the optic axis of the interferometer and light detection system,

   (b) changing and measurement of scattering angles.

To fulfill requirements 1 - 4 a liquid Helium cryostat fitted with an optical tailpiece and a variable temperature insert was obtained from the Oxford Instrument Company. The optical tailpiece and variable temperature insert were manufactured according to our design. Efficient temperature control was achieved using a 'Fisher' proportional controller. Requirement (5) above was fulfilled by mounting the cryostat on a mobile mount with vertical and lateral moving parts adjustable to ± 1 mm.

4.6.2. General Description of the Cryostat

A schematic diagram of the cryostat is shown in Figure (4.17). It is an ordinary vacuum insulated double resevoir liquid Helium cryostat with an outer liquid Nitrogen (or liquid Air) tank enclosing an inner liquid Helium tank. (In our use the the inner tank was filled only with liquid Nitrogen or liquid Air). The outer tank has a capacity of 15 l and that of the inner tank is 20 l. The optical tailpiece and the variable temperature insert were bolted to the lower end of the coolant resevoires. The overall height of the cryostat was 59 in.* and the diameter

---

* The units of length used in this section are not standardized; large mechanical structures were built in Imperial measurements while most small parts were built in metric measurements. It was felt unnecessary to convert all measurements to the same units as this would only serve to intorduce complicated fractions.

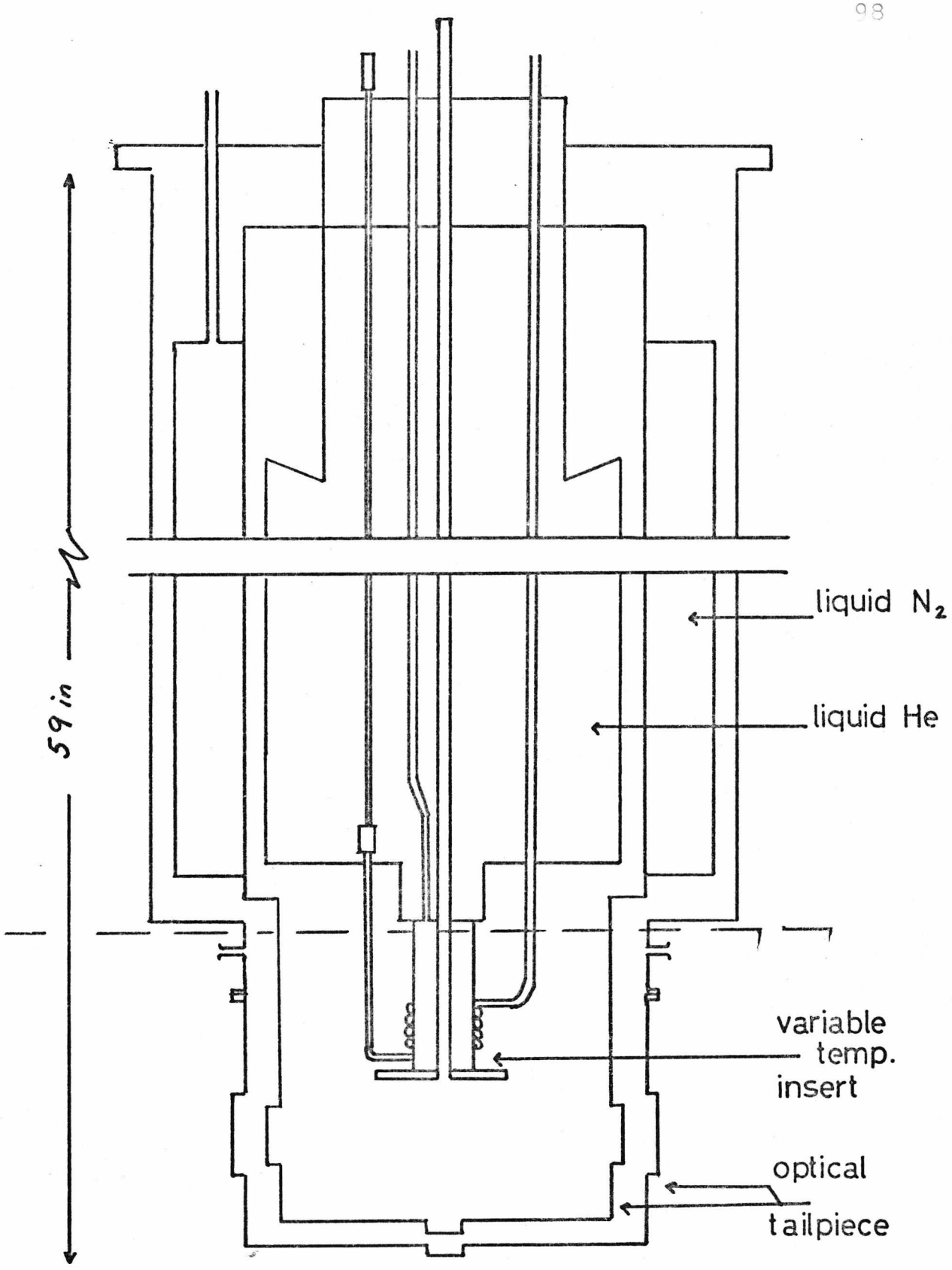


Figure 4.17: Schematic diagram of the cryostat.

of the cryostat body was 12.5 in.

The use of liquid Nitrogen in a liquid Helium cryostat had the advantage that the evaporation rate of coolant was much reduced. The large cryogenic liquid capacity of the cryostat was ideal for the extended period of refrigeration involved in these experiments.

As shown in Figure (4.17), the upper end of the outside wall of the cryostat ends in a shoulder from which the cryostat could be suspended from a platform.

### 4.6.3. The Optical Tailpiece

A schematic diagram of the optical tailpiece and the variable temperature insert with the sample cell clamp is shown in Figure (4.18). The optical tailpiece consists of the outer vacuum jacket (A) and the liquid Nitrogen heat shield (B). The vacuum jacket was fitted with two circular windows of 2½ in. diameter and a pair of ½ in. by 4½ in. rectangular windows. The liquid Nitrogen heat shield was fitted with a pair of circular windows of diameter 2 in. and similarly, a pair of rectangular windows, ½ in. by 3½ in. The circular and rectangular windows of the heat shield were arranged to correspond with the circular and rectangular windows on the vacuum jacket respectively. One optical window was constructed at the bottom of the vacuum jacket and heat shield for vertical illumination of the sample. All the windows were made of vitrisil. The vacuum jacket and heat shield envelop the variable temperature insert (D) and the sample cell, when

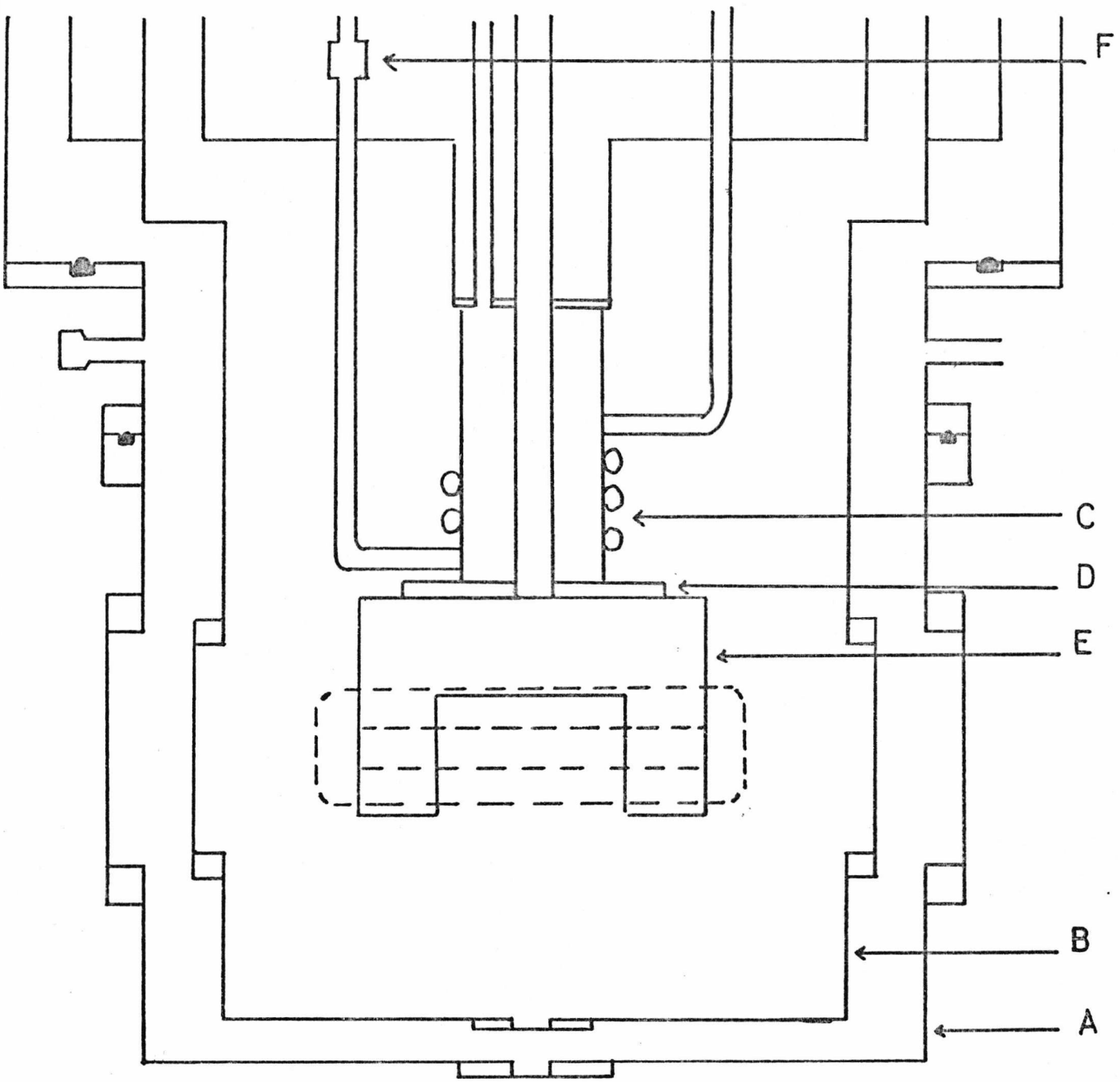


Figure 4.18: Details of the optical tailpiece and variable temperature insert; A: vacuum jacket, B: liquid $N_2$ heat shield, C: heat exchanger, D: variable temp. insert, E: sample cell clamp, F: needle valve.

it is fitted in the sample cell clamp (E).

4.6.4. The Variable Temperature Insert

The variable temperature insert consisted of a copper flange (D) (in Figure 4.18) suspended from the bottom of the liquid Helium resevoir via a thermal resistance (C) which consisted of a 2 in. diameter thin walled stainless steel tube. This stainless steel tube could be evacuated or filled with exchange gas as required. The sample cell clamp (E), made of high conductivity copper, was screwed to the bottom of the variable temperature flange. An additional coiled heat exchanger, for fast cooling of the sample cell, was wound round the stainless steel heat exchanger tube. This coiled heat exchanger enables cryogenic liquid to flow through it via a needle valve (F) in the liquid Helium resevoir operated from the top of the cryostat.

When the temperature of the sample cell was to be stabilised the needle valve was normally closed because the complex two-phase flow in the coil reduced the temperature stability of the system.

4.6.5. The Sample Cell

The sample cell, shown schematically in Figure (4.19) was made out of a rectangular block of copper 5 cm high, 6 cm wide and 12 cm long. Slits 0.5 cm wide and 4 cm long were drilled along the longitudinal faces. Similar

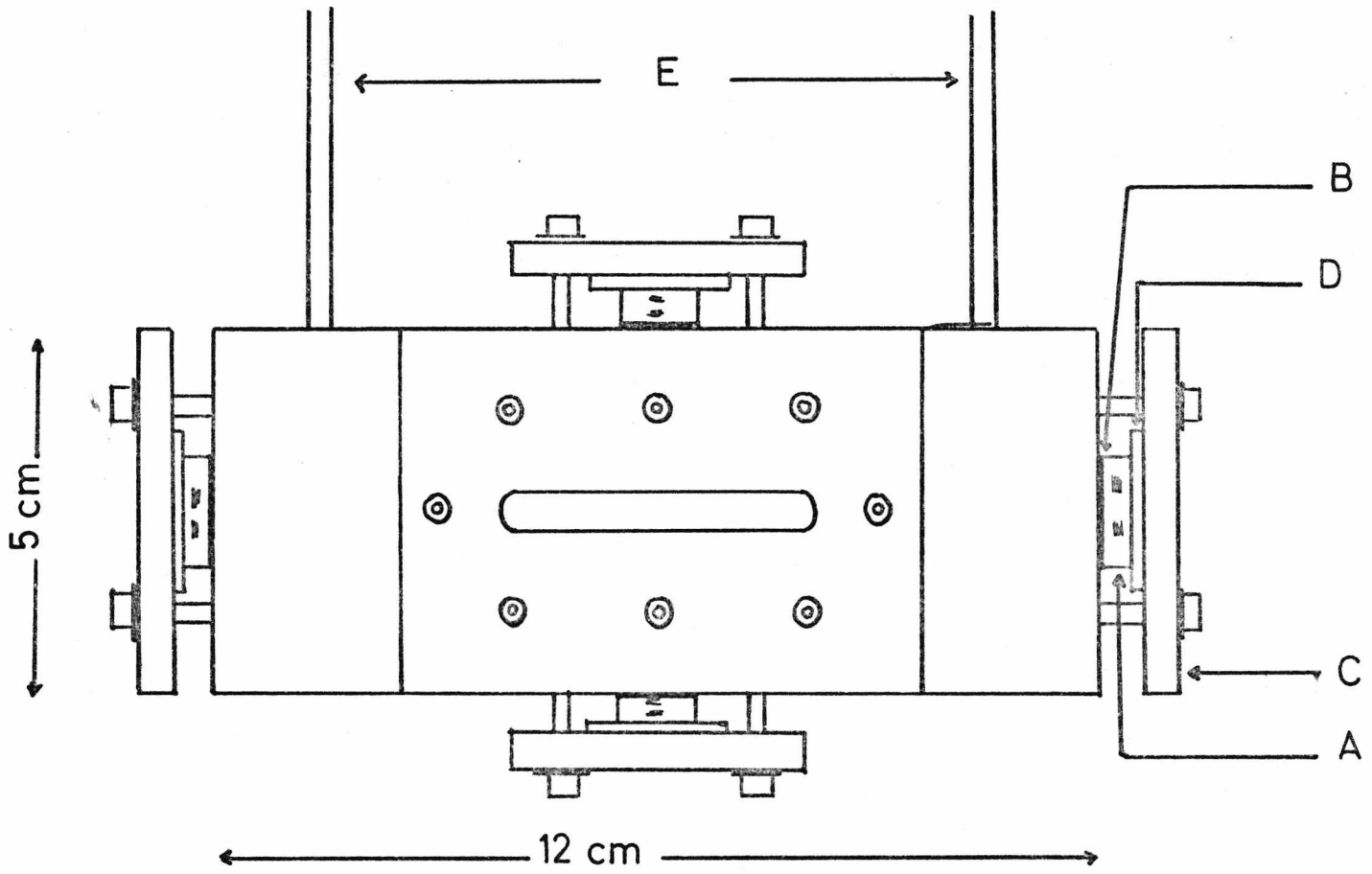


Figure 4.19: Schematic diagram of the sample cell; A: pyrex window, B: Indium seal, C: Copper flange, D: PTFE gasket, E: delivery tubes.

slits 0.5 cm wide and 3 cm long were drilled along the end faces. These slits meet in the interior of the block, thus forming the cell chamber. The volume of the cell chamber was ∿ 20 cc. The slit holes were closed with ¼ in. thick optically finished pyrex plates which form the cell windows, (A) (refer to Figure (4.19)). The window plates were vacuum-pressure sealed to the cell block with Indium wire (B) and clamped down with copper flanges (C). The copper flanges were screwed to the cell block, and they were layered with PTFE gaskets (D) to reduce mechanical strains on the window plates. Pressure measurement and filling of the sample chamber was via two ⅛ in. O.D. thick-walled stainless steel tubes (E) which were silver soldered into the top face of the cell.

The sample cell was held in place in the sample cell clamp by screwing the clamp faces onto the cell block. Heat transfer from the cell to the variable temperature insert was via the pressed contact between the cell clamp and the sample cell. For this reason the cell clamp was designed to obtain the maximum area of contact between the cell and clamp faces; care was taken to ensure that the contact was evenly distributed over the contact area. Low temperature grease was used for packing between the clamp and cell block. The grease packing helped to improve the thermal conduction between the cell block and the cell clamp. At temperatures below the freezing point of the grease its effect is probably somewhat reduced (12).

4.6.6. Electrical Wiring

The temperature of the sample cell was controlled by balancing the heat loss from the system with a pair of 75 w. heating elements embedded in the cell clamp. The power for the heaters was supplied from a 'Fisher' proportional temperature controller (described in the following section). Its sensing element was a thermistor probe embedded in a hole drilled in the cell clamp. Temperature measurement was carried out using a pair of platinum resistance thermometers, embedded in holes in the bottom and top of the sample cell respectively. These platinum resistance thermometers were separated by a distance of 3 cm. across the cell and could be used to indicate temperature gradients in the vertical direction across the cell.

The electrical leads to the heaters, thermistor and platinum resistance thermometers were made approximately 2 m. long and were wound many times round the bottom flange of the liquid Nitrogen tank before being taken out of the cryostat through pinseals. This minimised the transfer of heat from the room temperature ends of the wires to the sample cell.

4.6.7. Temperature Control and Measurement

The temperature of the sample cell was controlled using a 'Fisher' proportional temperature controller. The operation of the temperature controller can be described by looking at the simplified block diagram of

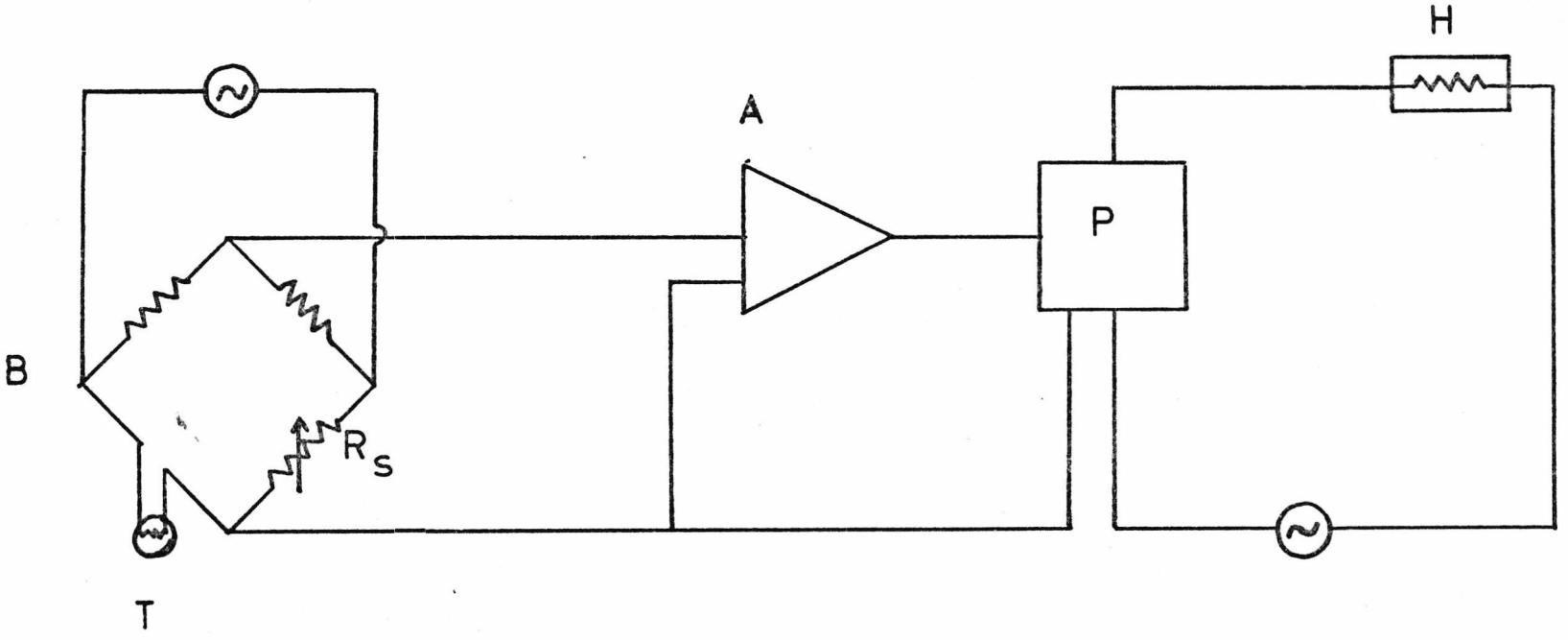


Figure 4.20: Simplified block diagram of the temperature controller circuit; A: proportional amplifier, B: a.c. bridge, H: heaters, P: power controller, T: thermistor probe.

the controller circuit shown in Figure (4.20). The temperature controller consisted of an a.c. bridge (B), a proportional amplifier (A) and a power controller (P). The thermistor probe (T) (Th 12 supplied by 'Conax') forms one arm of the a.c. bridge. The probe arm is balanced with the variable resistor $R_s$ whose value could be set for the required temperature. The required value of $R_s$ could be set by refering to the temperature-resistance characteristic of the thermistor, supplied by the manufacturer.

The off-balance signal from the a.c. bridge is amplified by the proportional amplifier which incorporates a high gain amplifier ($G \sim 2 \times 10^3$) and a demodulator. The output of the amplifier is proportional to the off-balance of the bridge, and this output is used to activate the power controller, supplying electrical power to the pair of heating elements (H) in the cell clamp.

The temperature of the sample cell was measured by measuring the resistances of a pair of calibrated platinum resistance themometers. One of these platinum thermometers was calibrated by 'Pitchcott Scientific Calibrations' and specified accurate to $\pm$ 0.005$^{o}$K. The other platinum thermometer was calibrated in this laboratory using the first one as the standard. To measure the resistance of the platinum resistance thermometers in the experiment, the thermometers were arranged in series with a standard 10 $\Omega$ ($\pm$ 0.001 %) resistor and a stable power supply. The voltages developed across the platinum thermometers were

compared with that across the standard resistor. The resistance of the platinum thermometer is then given by:

$$R_T = 10\left(\frac{V_T}{V_S}\right) \qquad (4.31)$$

where $R_T$ is the resistance of the platinum thermometer, $V_T$ and $V_S$ are the voltages measured across the platinum theromemeter and standard resistor respectively. (Contact emf's were eliminated in the usual way by reversing the supply voltage).

The current flowing through the system was maintained at $\sim$ 1mA to prevent any heating up of the platinum thermometers, giving rise to false temperature readings. The voltages across the resistors were measured with a 'Croydon Precision Instrument Company' (CROPICO) d.c. potentiometer Type P10, with a CROPICO precision d.c. Null Detector. A schematic diagram of the set-up used for the resistance measurement is given in Figure (4.21). The Null Detector has a full scale deflection of 1 μV. Thus, allowing for vibrations of the needle, measurements can be made accurate to ± 0.1 μV. With a current of 1 mA passing through the system resistances could therefore be measured to an accuracy of ± $1\times10^{-4}$ Ω (comparable with the accuracy of the standard resistor). The slope of the platinum thermometer calibration curve is approximately $10^{o}K/\Omega$. Thus the system is potentially capable of measuring temperatures accurate to ± $1\times10^{-3}{}^{o}K$. However, the accuracy of the temperature measurement was limited

by the long term temperature stability of the system which was better than ± 0.02°K over the whole range of temperatures.

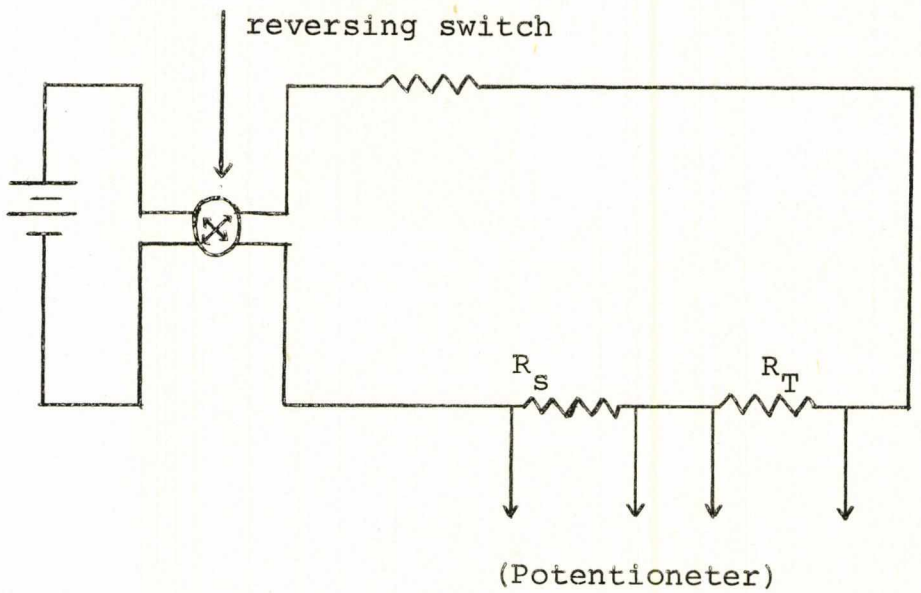


Figure 4.21: Circuit for Measuring Resistance of Platimun Thermometer

4.6.8. The Pressure Measuring System

We begin this section by distinguishing the different roles that pressure measurement played in the liquids and gas mixtures experiments. In the liquids experiments pressure readings (the saturated vapour pressure of the liquids) were used to indicate the temperature of the liquids, whereas in the gas mixtures experiments the pressure of the system indicated the concentration of the mixture. Because of the different uses made of the pressure

readings, the pressure measuring system (the pressure lines) in the two cases had slightly different designs to fulfill the different purposes.

A. Liquids

A schematic diagram of the pressure measuring system for the liquids experiments is shown in Figure (4.22). The pressure line was built of ¼ in. flexible copper tubes. Fixed joints were soft soldered and valves and variable joints were O-ring sealed. The valves used were high pressure O-ring sealed metal contact type supplied by 'Milne and Company', Catalogue No. HM80. The pressure measuring system consisted of a series of three standard test gauges and a mercury manometer. The test gauges cover the pressure ranges: 0-60, 0-300 and 0-1000 $lb/in^2$ respectively and were supplied by 'Budenberg Gauge Company Limited'. These test gauges were specified to be accurate to ± 0.5% of the maximum pressure reading. The mercury manometer was a closed tube type and could be used to cover pressures 0-1500 mm Hg; measurements could be made to ± 0.05 mm Hg.

The two low range test gauges and the mercury manometer were connected to the pressure line via high pressure valves; which enabled them to be isolated from the pressure line when the pressure reached the maximum tolerable sustained pressure of the gauges.

As shown in Figure (4.22) the pressure measuring instruments were joined to one of the two delivery tubes from

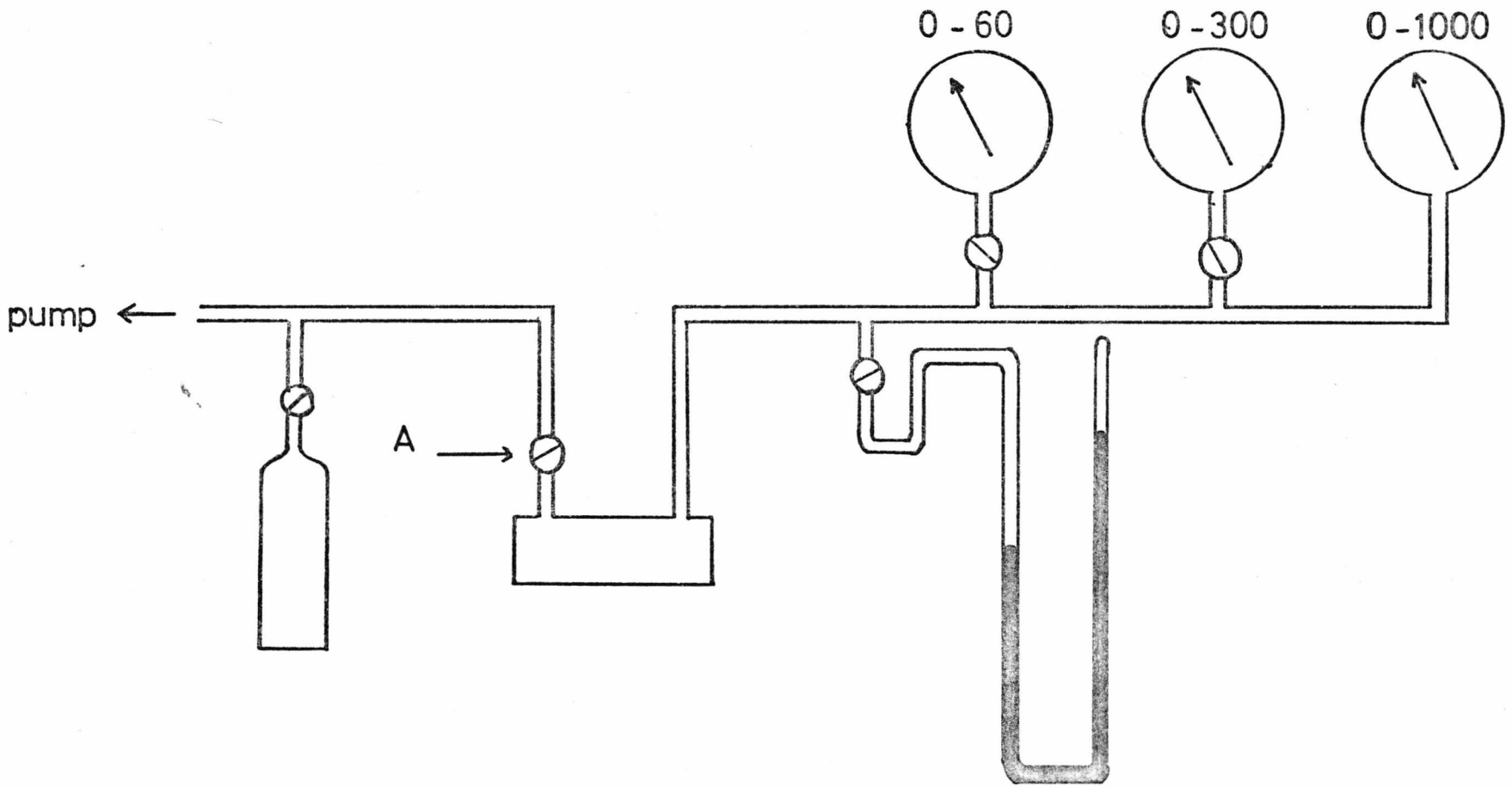


Figure 4.22: Pressure measuring system for the liquids experiments.

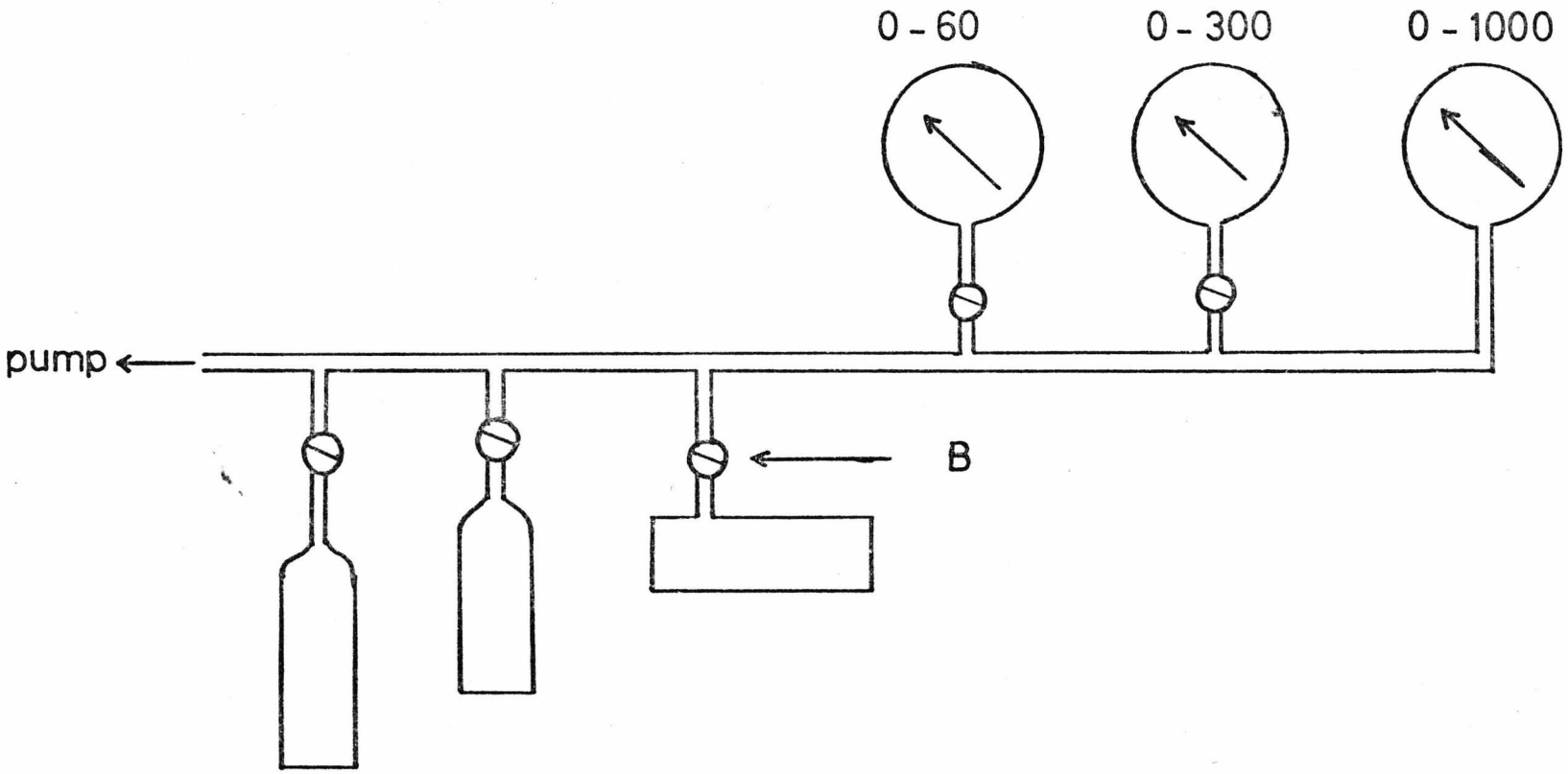


Figure 4.23: Preassure measuring system for the gas mixture experiments.

the sample cell, while the other delivery tube was connected to the gas cylinder and high vacuum pump.

B. Gas Mixtures

In the gas mixture experiments it was necessary to confine the sample to the scattering cell, when mixing the components (this is described in detail in section 4.8.2). This was achieved by modifying the pressure line such that only one of the delivery tubes of the sample cell was connected to the vacuum-pressure line. This is shown schematically in Figure (4.23).

## 4.7. The Cryostat Mounting System

The cryostat was mounted on a mobile stand. The purpse of the stand, apart from holding the cryostat upright, was to enable the sample cell to be positioned with high precision in the scattering region, and at the same time allow the cryostat to be moved out of the scattering region, whenever required.

The cryostat mount was constructed with both lateral and vertical adjustments. A schematic diagram of the mount is shown in Figure (4.24). It consisted of a vertical rig (A), 3 ft. wide and 7 ft. high, resting on a horizontal base (B), 3 ft. wide and 7.5 ft. long. The framework of the mount was made of 2 in. angle iron (2 in. square steel tube $\frac{1}{8}$ in. thick). The top of the vertical rig ended in a platform (C) on which the cryostat was suspended. This platform was constructed with

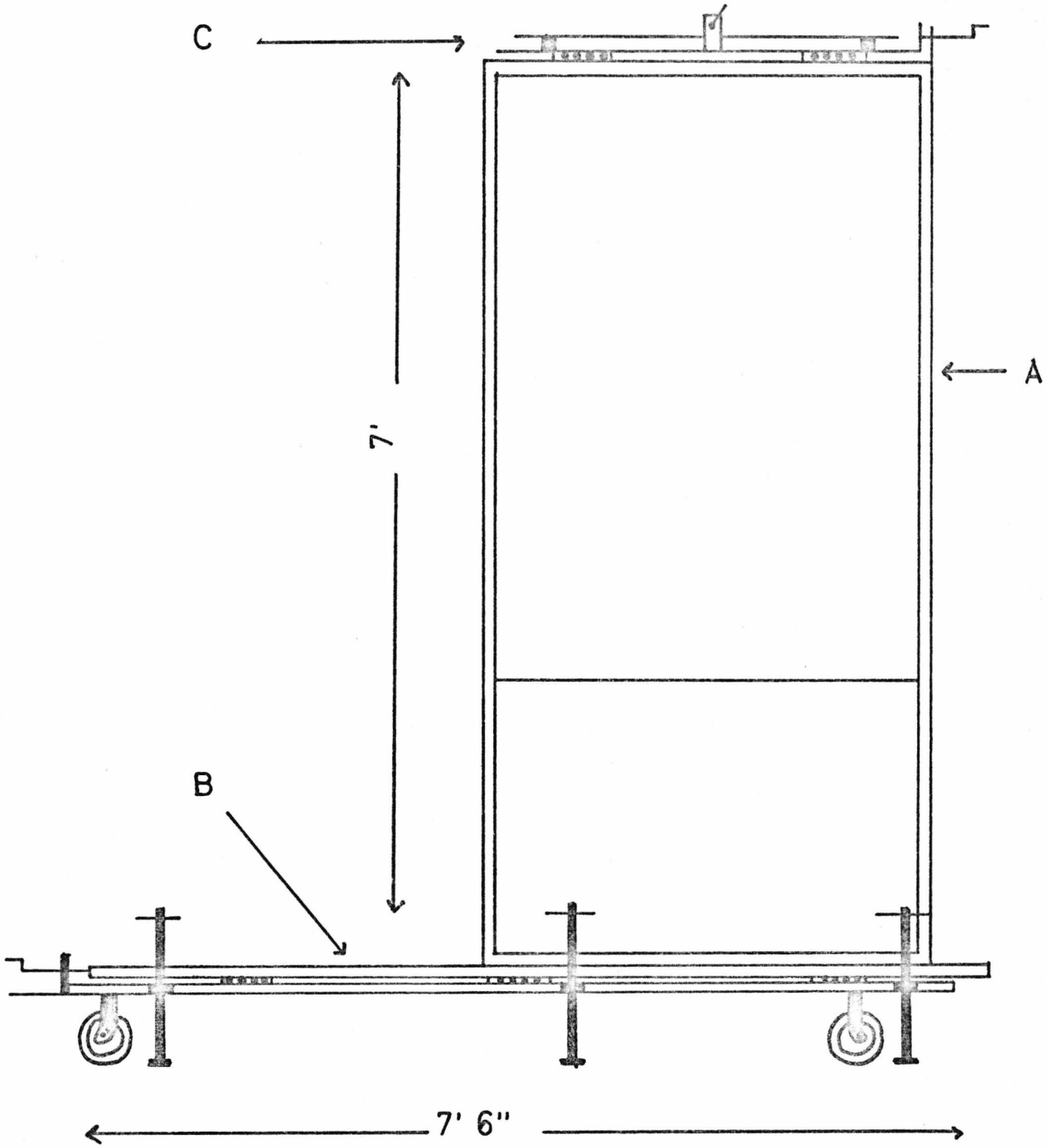


Figure 4.24: Schematic diagram of the cryostat mount; A: vertical rig, B: base platform, C: top platform.

translational movement in two mutually perpendicular directions.

Vertical adjustment and coarse lateral adjustments were facilitated by the base of the frame, while fine lateral adjustments were performed on the top platform. With these facilities adjustments accurate to better than ± 1 mm were possible.

## 4.8. Sample Handling

### 4.8.1. Rare Gas Liquids

Before cooling down the system the vacuum-pressure line and the sample cell were evacuated to $\sim 10^{-6}$ torr and flushed with the gas to be used at least twice. The gases used in these experiments were research grade gases supplied by the 'British Oxygen Company' (BOC) (Argon: 99.995 % pure and Krypton: 99.98 % pure) and were not further purified. Mass spectrometer analysis of the gases after use showed no increase in impurity content, insofar as the mass spectrum did not show the presence of elements other than those in the pure samples.

The gas was liquified directly into the sample cell. The procedure was to cool the sample cell and control its temperature at about $2^{o}K$ above the triple point of the gas and then allowing the gas to flow slowly into the cell using valve A (in Figure 4.22) to control the flow rate. Normally it took about a half of an hour to liquify enough gas to fill the cell to the required level. Care

was taken to make sure that the meniscus of the liquid was visible through the cell windows. This ensured that the liquid was not overpressurised, i.e. the pressure indicated by the pressure gauges was the saturated vapour pressure of the liquid. Since the gas to liquid volume ratio were about 1000 : 1 a standard twenty litre cylinder of the gas was sufficient to fill the cell with liquid to the required level.

To ensure that the liquid in the sample cell was not overpressurised and that the liquid was of acceptable purity the vapour pressure of the liquid was measured at various temperatures within the normal liquid range and above. These pressure-temperature readings were compared with SVP data of the gases available in the literature. Some of these measurments are given in Table (4.3) for liquid Argon (13) and Table (4.4) for liquid Krypton (14). From the tables it can be seen that the saturated vapour pressure measurements in the present work agree with the data refered to within ± 0.05$^{o}$K.

If the meniscus of the liquid was not visible through the window some of the liquid could be evaporated by opening the cylinder valve and valve A (Figure 4.22) after raising the temperature of the cell to the normal boiling point of the liquid or higher. At temperatures higher than its normal boiling point confirmation that the liquid was not overpressurised was obtained by letting off some of the gas and noting that the pressure stayed the same, after stabilisation. This is an indication that

Table 4.3: Saturated Vapour Pressure of Liquid Argon at some Temperatures

| $T_R$ ($^oK$) | P (atmosphere) | $T_P$ ($^oK$) | $\Delta T$ ($^oK$) |
|---|---|---|---|
| 85.54 | 0.826 | 85.53 | + .01 |
| 88.64 | 1.156 | 88.68 | - .04 |
| 90.19 | 1.340 | 90.16 | + .03 |
| 113.11 | 8.01 | 113.09 | + .02 |
| 130.04 | 19.86 | 130.02 | + .02 |
| 143.37 | 36.03 | 143.36 | + .01 |

$T_R$ = temperature measured by Platinum Resistance Thermometer
$T_P$ = temperature calculated from SVP data of reference (13)
$\Delta T = (T_R - T_P)$

Table 4.4: Saturated Vapour Pressure of Liquid Krypton at some Temperatures

| $T_R$ ($^oK$) | P (atmosphere) | $T_P$ ($^oK$) | $\Delta T$ ($^oK$) |
|---|---|---|---|
| 117.12 | 0.810 | 117.11 | + .01 |
| 120.69 | 1.076 | 120.67 | + .02 |
| 126.53 | 1.652 | 126.55 | - .02 |
| 132.35 | 2.42 | 132.33 | + .02 |
| 145.35 | 5.12 | 145.39 | - .04 |
| 162.19 | 11.26 | 162.23 | - .04 |
| 181.09 | 23.00 | 181.14 | - .05 |

$T_R$ is temperature measured by Pt. Resistance Thermometer
$T_P$ is temperature calculated from SVP curve (Ref.(14))
$\Delta T = (T_R - T_P)$

the liquid and vapour are under their equilibirum pressure.

4.8.2. Binary Gas Mixture

The gases used in these experiments were: research grade Argon (99.995 % pure), research grade Krypton and Neon (99.98 % pure) and industrial Helium (99.9 % pure). None of these gases were further purified.

The experiments on the gas mixtures were carried out at room temperature. The temperature was stable to $\pm 1^{\circ}K$ throughout the experiment.

As in the preparation of the liquid samples, the pressure system and the cell were evacuated to $\sim 10^{-6}$ torr and flushed at least twice with the componet #1 prior to commencement of the experiments. The cell was then filled with component #1 to a pressure > 3 atmosphere to ensure that the system could be classified as in the hydrodynamic region. This also ensured that the intensity of the scattered light was high enough for the spectrum to be easily detected. The hydrodynamic region is indicated by the characteristic distinct Brillouin Doublet and central Rayleigh lines in the spectrum of the scattered light. If the pressure was too low the scattered light spectrum was a single broad line due to the Boltzmann velocity distribution of the atoms in the scattering region. In the case of Krypton and Argon gases the scattered intensity was sufficiently strong to be easily detectable at pressures > 4 atmosphere.

For the preparation of the mixtures valve B (refer to Figure 4.23) was closed and the whole system was evacuated except for the sample cell. The system was then similarly flushed with the gas component #2, after which the pressure line was filled with component # 2 to the required pressure to obtain the concentration desired. This pressure was calculated assuming ideal gas conditions and the pressure P to which the system has to be filled up is given by,*

$$P = P_0(1 + C\frac{M1}{M2}) \qquad (4.32)$$

where M1 and M2 are the molecular weights of the component #1 and #2 respectively, C is the concentration, and $P_0$ is the original pressure of component #1 used.

Equation (4.32) does not take into account the volume of the pressure line and gauges. When this volume was considered we obtain (still assuming ideal gas conditions):

$$P_l = P + R(P - P_c) \qquad (4.33)$$

where $P_l$ is the pressure to which the pressure line needs to be raised to obtain a pressure P in the whole system (equation 4.32) when valve B was opened. R is the ratio of the volume of the sample cell to that of the pressure line and $P_c$ is the pressure of the mixture (or component #1) in the sample cell previously. In our system R = 2/7.

---

* See appendix 111.

The procedure outlined above gives the approximate pressure required to obtain a certain concentration C. The purpose of the procedure was just to simplify 'filling up' of the system. The true concentration of the mixture was then calculated from the pressures using the virial coefficients (15) for the components and mixture.

To obtain the mixture the pressure line was filled with the gas component #2 to the pressure given by euqations (4.32 - 33) above and the gas cylinder valve was shut. Then valve B was opened and the gas component #2 was allowed to flow into the cell slowly. Once the pressure had stabilised valve B was shut again. It was assumed that during the opening of valve B no back-flow of component #1 took place. The mixture was then allowed to reach equilibration of concentration (by diffusion) for 48 hours.

## 4.9. Setting Up and Measurement of Scattering Angles

The experiments, both on the liquids and the binary gas mixtures were performed at various scattering angles. To facilitate the variation and the measurement of the scattering angle the following procedure was adopted.

A permanent beam was set which defined the optical axis of the interferometer, light detection system and the scattering cell, shown schematically in Figure (4.25). Mirror M1 is coated with 96% reflectivity, thus allowing enough of the laser beam to pass through to form the optical-axis-defining beam. Mirror M2 is kept fixed throughout the experiment, while M3 was a 'floating' mirror

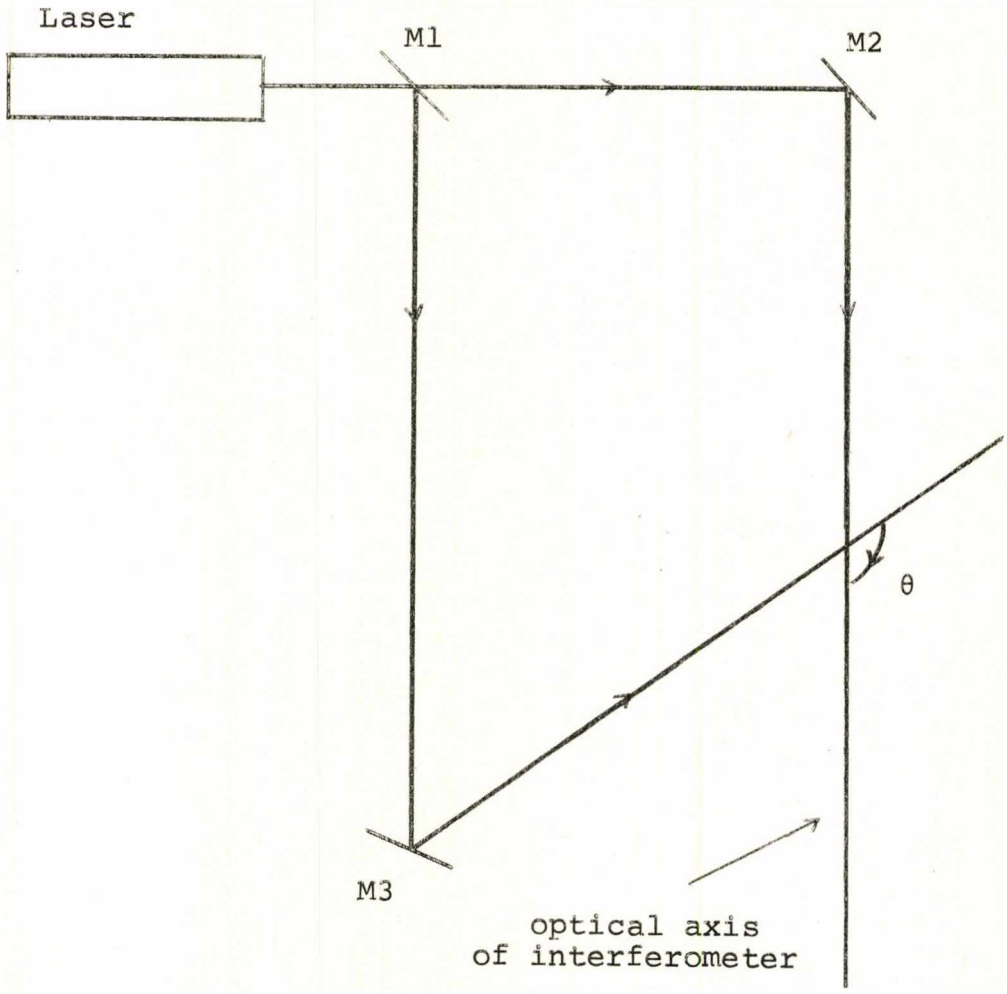


Figure 4.25: Experimental set-up for defining the scattering angle θ

whose position could be changed when the scattering angle was to be varied. The scattering angle, $\theta$, is defined by the angle between the directions of the incident beam and the axial beam, taken in clockwise direction (as shown in Figure 4.25). The axial beam was screened off during measurements of the spectra.

The scattering angle was measured by a method of reflections. This involved using a beam reflector fixed on a conventional spectrometer table. This had an angular vernier with markings of ½ minute of an arc. The reflector used was a microscope slide, fixed on the top of the spectrometer table.

To measure the angle between the axial beam and the incident beam (scattering angle) the spectrometer table was placed in the scattering region with its vertical axis (vertical axis of the rotating table) just below the point of intersection of the two beams. The reflector will then be at the intersection of the two beams. Three specific angular positions of the reflector were then obtained. These angular positions were:

(a) The axial beam reflected by the reflector back into the laser.
(b) The incident beam reflected back into the laser.
(c) The axial beam reflected back into the laser along the path of the incident beam and vice versa.

The difference in angular positions of (a) and (b) gives the full angle ($\theta$) between the beams; and the differences between (a) and (c) and (b) and (c) give the half angles ($\theta/2$) between the beams.

It was relatively easy to establish that the reflected beam reentered the laser co-axially since when this occurred the frequency stability of the laser altered drastically.

With the method outlined above angle measurements accurate to $\pm$ ½ minute of arc were achieved.

## 4.10. Data Analysis

### 4.10.1. The Measured Spectrum

The measured spectrum of the scattered light is distorted by two experimental factors: (1) the finite collection angle of the interferometer and (2) the instrumental profile of the interferometer. The effect of these factors is that the measured spectrum is not the "real" $S(K, \omega)$, but the convolution of $S(K, \omega)$ with the aperture function of the collection optics and the instrumental profile respectively.

Further, since $S(K, \omega)$ is the "sum" of the spectral densities of the central and Brillouin lines, the overlapping of the tails of the central line on the Brillouin lines results in the Brillouin lines being pulled in towards the central line. Consequently the

observed positions of the peaks of the Brillouin lines are shifted towards the central line. Accordingly the observed Brillouin shifts have to be corrected for this "line pulling".

We now present a simple analysis of the effects of the instrumental distortion and the "line pulling" and outline the methods for correcting these effects where necessary.

4.10.2 The Aperture Effect

The finite collection solid angle of the interferometer introduces a range of scattering vectors $\Delta k_s$ about $k_s$. The effect of this distribution of scattering vectors is to introduce a smearing $\Delta\omega_0$ to the Brillouin shift $\omega_0$:

$$\Delta\omega_0 = C_0 \Delta k_s \qquad (4.34)$$

The scattering geometry is shown in Figure (4.26) where we have drawn a two-dimensional projection of a three-dimonsional process. The scattering region is at the focus of the collecting lens which is stopped with the aperture, diameter a. It can be shown that to a first approximation the finite collection angle introduces a broadening of the Brillouin lines given by (16):

$$\Delta\omega_a = \omega_o (\alpha\Delta\theta) \cot(\tfrac{\theta}{2}) \qquad (4.35)$$

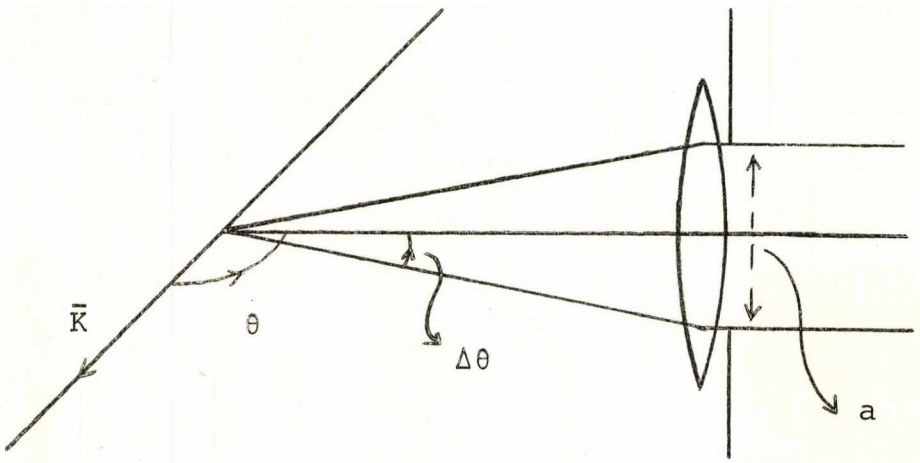


Figure 4.26: Geometry of Collection Optics

where $\Delta\omega_a$ is the linewidth due to the aperture alone, $\omega_0$ is the Brillouin frequency shift and $\alpha$ is a factor, $\frac{1}{2} < \alpha < 1$, characteristic of the aperture. Reference (16) quoted the factor for circular aperture as $\alpha = 4/5$.

Equation (4.35) shows that the broadening effect of the aperture diminishes for large scattering angles due to the $\cot(\theta/2)$ factor.

In our experiments the aperture diameter a = 0.5 cm and the focal length of the collecting lens, f = 100 cm. Thus $\Delta\theta \simeq 2.5 \times 10^{-3}$ rad.

As an illustration of the effect of the aperture broadening we take the case of the backward scattering in liquid argon ($\theta = 169^{\circ}51'$). Thus in this case equation (4.35) gives $\Delta\omega_a = 0.177 \times 10^{-3}\omega_o$. For liquid argon at $85^{\circ}$K, scattering angle $\theta = 169^{\circ}51'$, $\omega_o \simeq 4$ GHz. Hence $\Delta\omega_a \simeq 0.7$ MHz. The Brillouin linewidth of liquid argon at this scattering angle is $\sim$ 60 MHz. Hence the aperture broadening has a negligible contribution to the errors in our measurements of frequency shifts and linewidths*.

---

* The aperture broadening can be assumed to be symmetric, so that it does not affect the frequency shift. It is negligible in linewidth measurements because the accuracy of these measurements is only of the order of ± 3 MHz.

Table (4.5) shows the variation of $\Delta\omega_a/\omega_0$ for various scattering angles, calculated from equation (4.35).

Table 4.5: Variation of $\Delta\omega_a/\omega_0$ with Scattering Angle

| $\theta^o$ | $(\Delta\omega_a/\omega_o) \times 10^3$ |
|---|---|
| 10 | 22.86 |
| 90 | 2.00 |
| 170 | 0.174 |

4.10.3. The Effects of the Instrumental Profile and Line Overlapping

The degree of overlapping of the tails of the central line on the Brillouin lines depends on the Brillouin shift and linewidth and the resolution of the interferometer. The presence of significant line overlapping is indicated by the difference in the levels of the intensity minima on the high-frequency and low-frequency sides of the Brillouin line.* When line overlapping is present the minimun on the low-frequency side is higher than that on

---

* This is true only in atomic liquids. In molecular liquids the presence of molecular reorientation mode (Mountain Mode) can also give rise to this sympton.

the high-frequency side. A theoretical investigation into this effect has been carried out by La Macchia, et al. (17) for Lorentzian line shapes. However, the application of this method is quite complicated, and in this work an alternative procedure was adopted.

A numerical method of least squares was used to find the correct frequency shifts. In this procedure the recorded spectrum is assumed to consist of n Lorentzian lines of width either $\Gamma_C$ or $\Gamma_B$ depending on whether the line is a central (Rayleigh) line or a Brillouin line respectively. (Normally n = 6, i.e. for a FSR the spectrum contains two central lines and four Brillouin lines). An approximation $S_i$ to a data point $y_i$ on the spectrum is given by the sum of the contributions of the n lines. Thus we write:

$$S_i = \sum_j^n a_j L_i (\omega_i - \omega_j) \tag{4.36}$$

where

$$L_i(\omega_i - \omega_j) = \frac{(\Gamma_C)^2}{(\Gamma_C)^2 + (\omega_i - \omega_j)^2} \tag{4.37}$$

for a central line and

$$L_i(\omega_i - \omega_j) = \frac{(\Gamma_B)^2}{(\Gamma_B)^2 + (\omega_i - \omega_j)} \tag{4.38}$$

for a Brillouin line. $\omega_j$ is the centroid of the line.

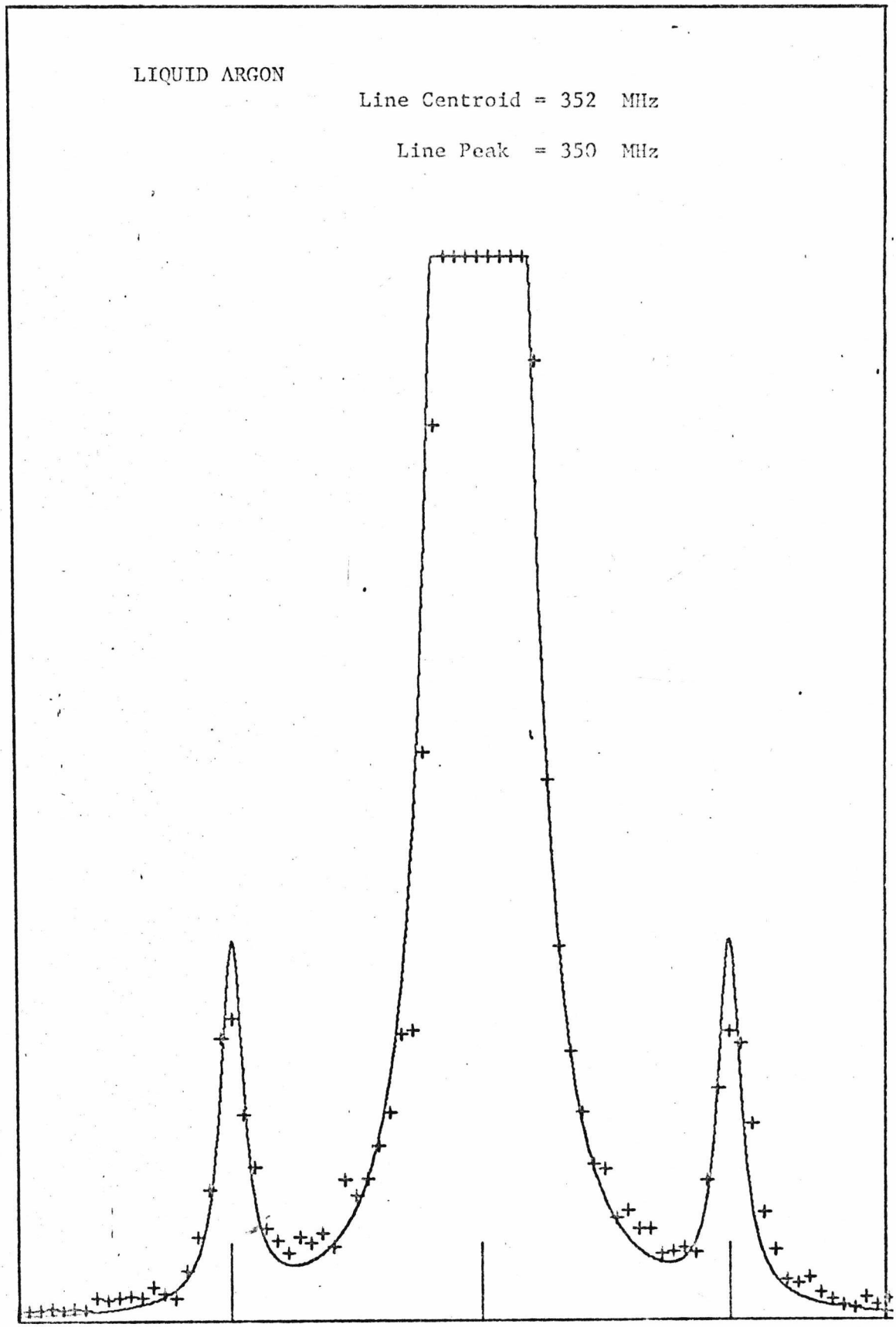


Figure 4.27: Lorentzian fit to a spectrum of light scattered from liquid Argon, (by computer)

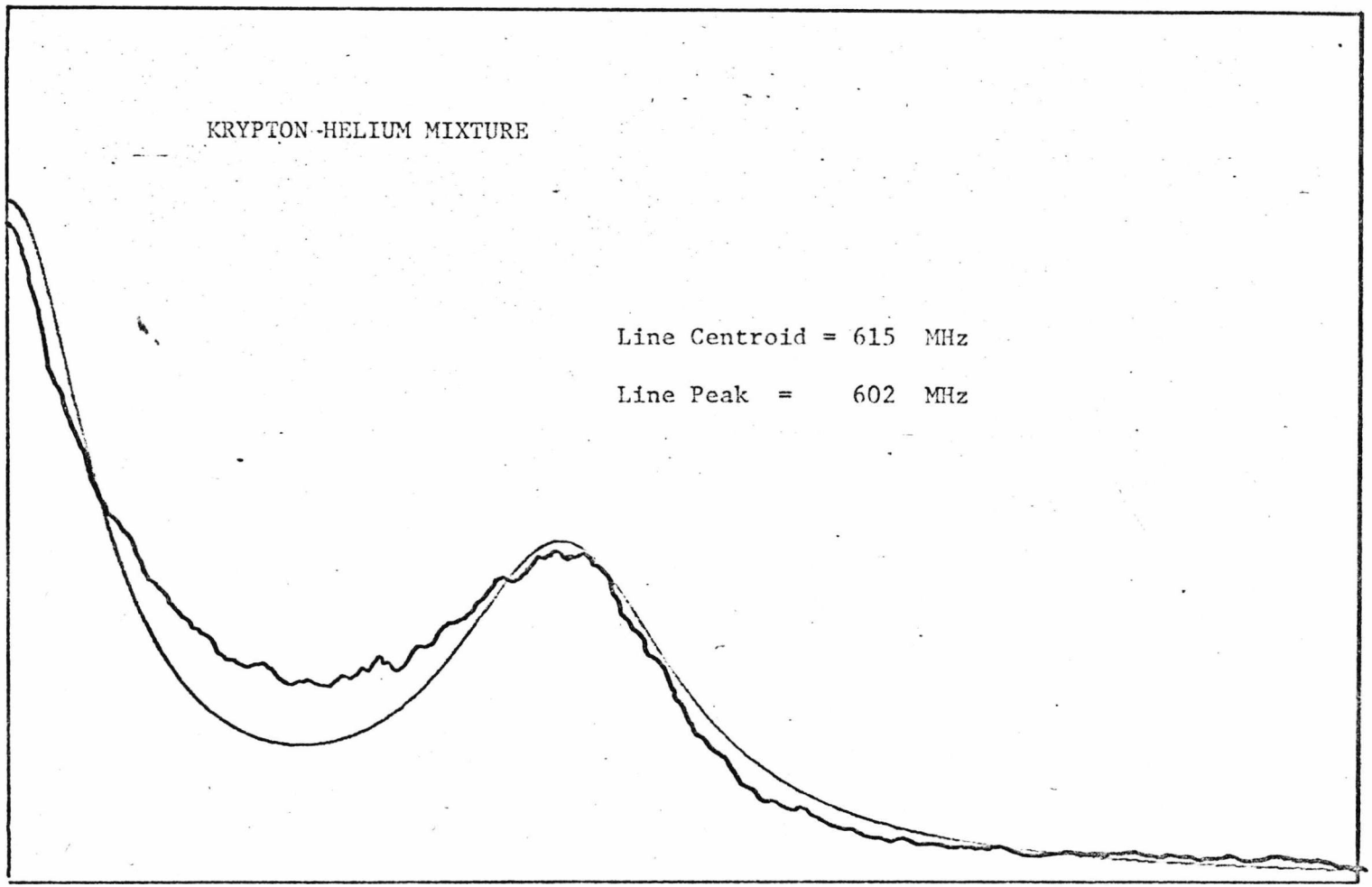


Figure 4.28: Lorentzian fit to a spectrum of light scattered from Kr-He mixture, (by computer).

The coefficients $a_j$ have the values 1 for a Rayleigh line and the ratio of average peak heights of Brillouin lines to Rayleigh lines for a Brillouin line.

The fitted points $S_i$ are then optimised iteratively by a least squares procedure (18, 19), i.e. by minimising

$$\sigma = \sum_{i}^{N} (S_i - Y_i)^2 \qquad (4.39)$$

with respect to the variables $\omega_j$'s, $\Gamma_C$ and $\Gamma_B$. (N is the number of data points in the recorded spectrum).

To overcome the ill-conditioned nature of the function $\sigma$ the iteration is restrained in such a way that the values of $\omega_j$'s, $\Gamma_C$ and $\Gamma_B$ are allowed to change with small steps only. This prevents the procedure from 'blowing up'. A listing of the programme is given in Appendix IV.

The initial values of the $\omega_j$'s, $\Gamma_C$ and $\Gamma_B$ are obtained from the recorded spectrum. Normally for N = 500 a satisfactory degree of convergence is obtained in five to eight iterations, which takes a maximum of 40 sec. of computing time. Typical results indicating the degree of fit are illustrated by Figures (4.27) and (4.28).

### 4.10.4. Measurement of Brillouin Linewidth

The convolution of the instrumental function with the spectral distribution of the scattered light introduces a broadening in the spectral lines. Hence in order to obtain the Brillouin linewidth the instrumental profile has to

be deconvoluted from the observed spectrum. The deconvolution can be performed in two ways:

(1) By direct deconvolution where the instrumental function is deconvoluted from the experimental data. This can be carried out using an interative procedure (20) or by the use of Fourier Transform (21, 22).

(2) By indirect deconvolution. In this method the instrumental function is convoluted with a function of standard form and finding one of the standard functions that convolutes with the instrumental function to give results similar to the observed spectrum.

The first method above is theoretically favoured but its application is difficult and complicated, while the second method is relatively simple and the accuracy of the results depends on using the right choice of standard function. In this work this latter method was used.

From the theoretical discussions of Chapters II and III it is justifiable to assume that the Brillouin lines are of Lorentzian shape. Thus a series of Lorentzian lines of varying linewidths were nemerically convoluted with the instrumental function of the FPS (see section 4.4.3.). A point $S(\omega)$ on the convoluted spectrum is given by

$$S(\omega) = \sum_{i}^{N} M(\omega_i) L\ (\omega - \omega_i) \qquad (4.40)$$

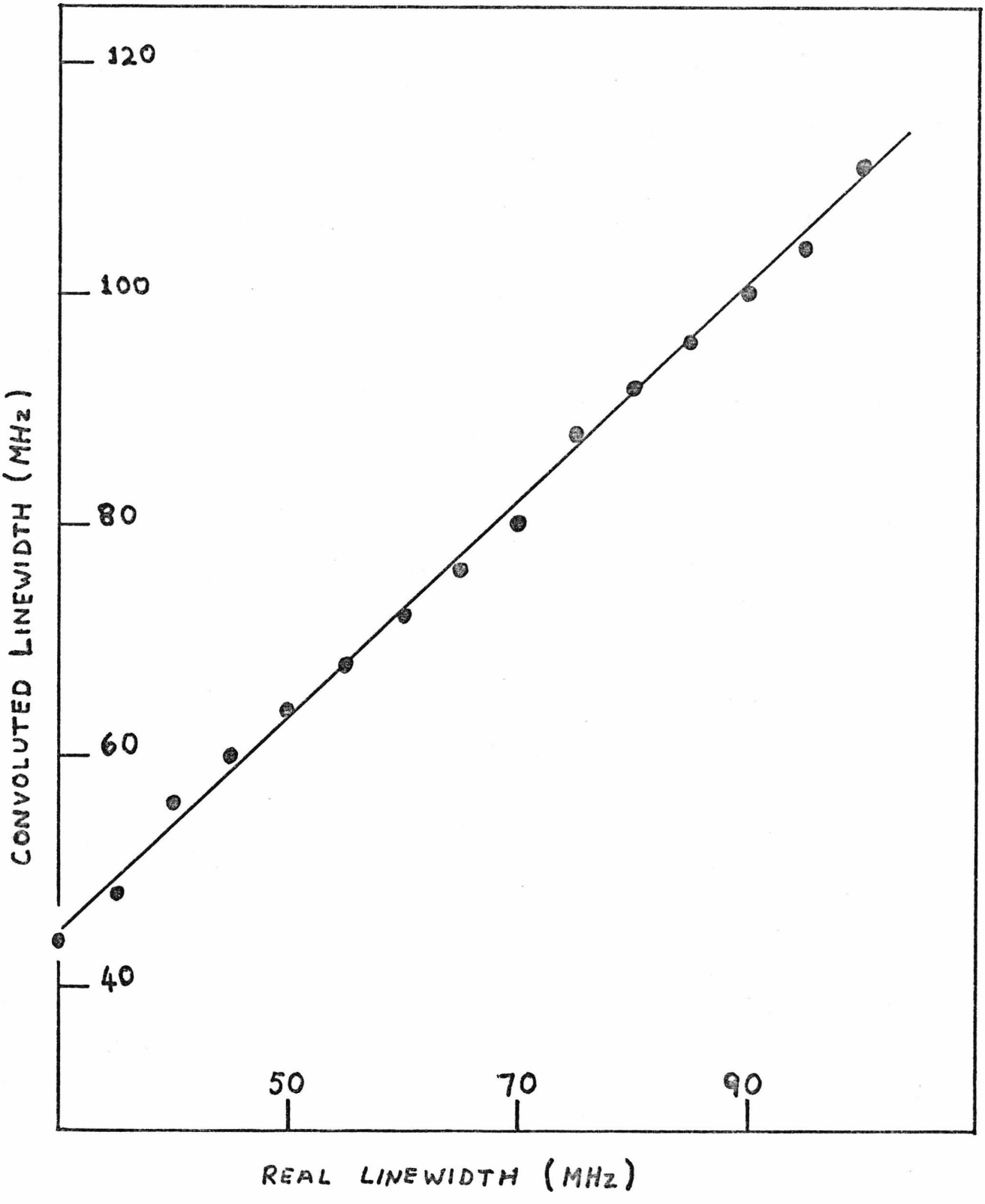


Figure 4.29: Instrumental broadening: relationship between convolved linewidth and real linewidth.

where $M(\omega)$ is the instrumental function,

$L(\omega)$ is a Lorentzian function, and

$N$ is an arbitrary number of points,

(in this case $N = 500$).

Figure (4.29) shows a linear relationship of the linewidth of $S(\omega)$, the convoluted linewidth, with that of $L(\omega)$, the real linewidth. This graph was used to convert measured linewidths to real linewidths.

4.10.5. Numerical Convolution of Theoretical Spectrum

In order to be able to compare the theoretical spectrum with the observed spectrum the theoretical spectrum has to be convoluted with the instrumental function. This introduces the instrumental broadening to the theoretical spectrum.

We have used a direct method of numerical convolution, where the theoretical spectrum, $S(K, \omega)$ is convoluted with the instrumental function, $M(\omega)$. The procedure is as follows:

The convolution is given by equation (4.40) which we rewrite as:

$$F(\omega) = \sum_{i}^{N} M(\omega_i)\ S(K, \omega-\omega_i) \qquad (4.41)$$

The range of $\omega_i$ is within $\omega_i = \pm$ FSR/2. $S(K, \omega)$ and $M(\omega)$ have the forms illustrated in Figure (4.30 (a)).

The instrumental function is periodic, with a periodicity of a free spectral range. In order to introduce the periodicity into equation (4.41) $S(K, \omega)$ is 'folded' in frequency by setting

$$S(K, \omega \pm FSR) = S(K, \omega) \tag{4.42}$$

This is illustrated in Figure (4.30 (b)). This procedure is is especially important when the Brillouin shifts, $\omega_B > FSR/2$ because in this case if the frequency extension (4.42) is not performed equation (4.41) will not produce the Brillouin lines.

We divide the frequency range of $\omega_i$ into 500 steps of $\Delta\omega_i$. Thus for a FSR = 3 GHz, the frequency steps $\Delta\omega_i$ = 6 MHz.

To perform the convolution the functions $M(\omega)$ and $S(K, \omega)$ were first stored in arrays and the convolution can then be carried out with maximum saving of computing time. Typical computing time for a spectrum is $\sim$ 1.5 minutes.

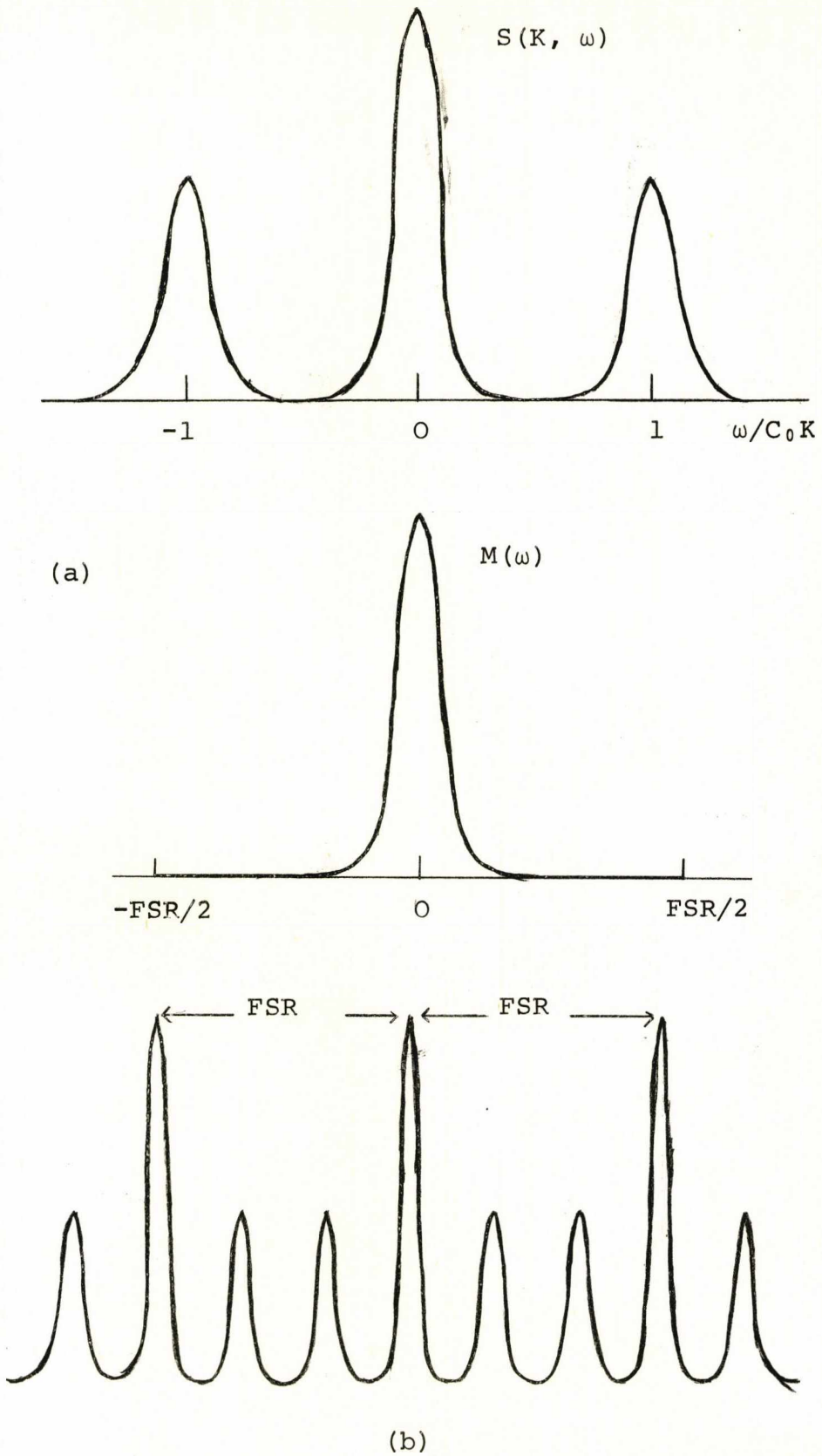


Figure 4.30: Numerical convolution (a) Theoretical spectrum and instrumental function to be convolved (b) 'Folded' theoretical spectrum.

References in Chapter IV

(1) Some of the many books dealing with the theory of the laser are:

(a) L. Allen; 'Principles of Gas Lasers', Butterworths (1967)

(b) A.A. Langyel; 'Introduction to Laser Physics', John Wiley and Sons, Inc. (1966)

(c) A.K. Levine; 'Lasers' Vol. 2, Edward Arnold Publishers, Ltd. (1966)

(d) Scientific American; 'Lasers and Light', Freeman (1969)

(e) D.C. Sinclair; 'Gas Laser Technology' Holt, Rinehart and Winston, Inc. (1969)

(2) H.G. Heard; 'Laser Parameter Measurments Handbook', John Wiley and Sons, Inc. (1968)

(3) See for example:

(a) M. Born, E. Wolf; 'Principles of Optics' Pergamon Press (1965) (third edition)

(b) R.S. Longhurst; 'Geometrical and Physical Optics', Longmans (1967) (second edition)

(c) F.G. Smith, J.H. Thomson; 'Optics', John Wiley and Sons, Inc. (1971)

(4) (a) E. Pelletier, P. Giacomo; Rev. Phys. Appl. 2, 52 (1967)

(b) I.J. Hodgkinson; Appl. Opt. 10, 396 (1971)

(5) G.W.C. Kaye, T.H. Laby; 'Tables of Physical and Chemical Constants', Longmans, Green and Co. Ltd. (1968, New impression)

(6) P. Connes; Rev. Opt. 35, 37 (1956)

(7) J.R. Johnson; Appl. Opt. 7, 1061 (1968)

(8) M. Hercher; Appl. Opt. 1, 951 (1968)

(9) J.S. Bendat; 'Principles and Applications of Random Noise Theory', John Wiley and Sons, Inc. (1958)

(10) W.B. Davenport, W.C. Root; 'An Introduction to the Theory of Random Signals and Noise', McGraw-Hill Book Company, Inc. (1958)

(11) H. Margenau, G.M. Murphy; 'The Mathematics of Physics and Chemistry, Vol. 2', D. Van Nostrand Company, Inc. (1964)

(12) M. Rechowicz, T. Ashworth, H. Steele; Cryogenics 7, 369 (1967)

(13) G.A. Cook; 'Argon, Helium and the Rare Gases', Interscience Publications (1961)

(14) C. Gladun, F. Menzel; Cryogenics 10, 210 (1971)

(15) J.O. Hirschfelder, C.F. Curtis, R.P. Bird; 'Molecular Theory of Gases and Liquids', John Wiley and Sons, Inc. (1964)

(16) H.G. Danielmeyer; J. Acous. Soc. Amer. 47, 151 (1970)

(17) H.W. Leidecker,Jr., T.T. La Macchia; J. Acous. Soc. Amer. 43, 143 (1968)

(18) W.A. Watson, T. Philipson, P.J. Oates; 'Numerical Analysis - The Mathematics of Computing, Vol. 2', Edward Arnold (1969)

(19) R.W. Hamming, 'Numerical Methods for Scientists and Engineers', McGraw-Hill Book Company, Inc. (1962)

(20) J. Szoke; Chem. Phys. Lett. 15, 404 (1972)

(21) V.G. Cooper; Appl. Opt. 10, 525 (1971)

(22) H. Schrijver; Physica 49 (1970)

# CHAPTER V

# EXPERIMENTAL RESULTS AND DISCUSSION

## 5.1. Pure Monatomic Liquids

### 5.1.1. Introduction

We have measured the spectra of light scattered from liquid Argon and liquid Krypton at various temperatures along the saturated vapour pressure curves of these liquids. The spectra were taken at various scattering angles: $\theta = 13^{\circ}\ 35'$, $102^{\circ}\ 47'$ and $169^{\circ}\ 51'$ in liquid Argon and $93^{\circ}\ 48'$ and $169^{\circ}\ 20'$ in liquid Krypton. (These were the angles of intersection of the incident beam with the optic axis of the interferometer in air. The actual scattering angles in the liquids were calculated by making corrections for the refractive index of the liquids).

From the measured values of the shifts, $\omega_B$ of the Brillouin lines we were able to calculate the sound velocities in these liquids at frequencies $\omega_B$. The accuracy of the measurement of the Brillouin shifts depends on the precision with which the Brillouin peak positions were determined and the accuracy of the frequency scale. The positions of the Brillouin peaks could be determined with an accuracy of $\pm$ 0.06%. The accuracy of the frequency scale (section 4.3.3.) is $\pm$ 0.17%. Thus the nett accuracy of the determination of the Brillouin frequency shifts is of the order of $\pm$ 0.18%.

By using a high resolution confocal spherical Fabry-Perot interferometer we were also able to measure the

Brillouin linewidths in the back-scattering geometry in these liquids. From the measured values of the Brillouin linewidths the sound absorption coefficient, $\alpha$, was calculated using the equation (1):

$$\alpha = \frac{\pi \Delta\omega_B}{V} \qquad (5.1)$$

where V is the sound velocity and $\Delta\omega_B$ is the Brillouin linewidth in Hz. The Brillouin linewidth, $\Delta\omega_B$ could be determined to an accuracy of about ± 8%.

We shall now present and discuss these results in liquid Argon and liquid Krypton.

### 5.1.2. Sound Velocity in Liquid Argon

The results of our measurements of Brillouin shifts in liquid Argon, obtained at the three scattering angles listed above are shown in Table (5.1). Because of the presence of a large amount of 'stray' light arising from flares on the potical windows of the cell and cryostat encountered in the forward- and back-scattering geometries, measurements at these angles were carried out only within a small range of temperatures.

In cases where the spectra showed a difference in the levels of the minima on the high- and low- frequency sides of the Brillouin lines, i.e. where there is marked appearance of overlapping of the tails of the unshifted central line on the Brillouin lines, the Brillouin shifts were corrected for 'line-pulling' in the manner described in chapter IV (Section 4.10.3).

Table 5.1: Brillouin Shift and Sound Velocity in Liquid Argon along the Saturated Vapour Pressure Curve

(b) calculated from polynomial fit in reference (4)

| T($^{o}$K) | n | $\theta$ ± 0.5' | $\omega_B$ (GHz) ±.006 | V($mS^{-1}$) Hypersonic ±2.0 | (b) Ultrasonic ±.08 |
|---|---|---|---|---|---|
| 85.25 | 1.2321 | 13°35' | 0.393 | 854.8 | 851.32 |
| 87.81 | 1.2284 | " | 0.383 | 832.9 | 833.79 |
| 89.28 | 1.2266 | " | 0.379 | 824.5 | 823.54 |
| 97.12 | 1.2188 | " | 0.353 | 766.7 | 767.73 |
| 104.05 | 1.2115 | " | 0.328 | 712.7 | 715.86 |
| 110.12 | 1.2038 | " | 0.308 | 668.8 | 667.96 |
| 85.28 | 1.2320 | 169°51' | 4.062 | 850.2 | 851.16 |
| 89.32 | 1.2266 | " | 3.922 | 824.6 | 823.31 |
| 92.12 | 1.2236 | " | 3.813 | 803.7 | 803.62 |
| 97.91 | 1.2180 | " | 3.598 | 762.0 | 761.90 |
| 101.06 | 1.2148 | " | 3.473 | 737.5 | 738.53 |
| 89.15 | 1.2267 | 102°47' | 3.033 | 827.8 | 824.26 |
| 90.72 | 1.2250 | " | 2.988 | 816.5 | 813.52 |
| 93.77 | 1.2219 | " | 2.896 | 793.4 | 791.92 |
| 96.50 | 1.2194 | " | 2.829 | 776.5 | 772.19 |
| 97.12 | 1.2188 | " | 2.802 | 769.5 | 767.72 |
| 98.21 | 1.2177 | " | 2.764 | 759.7 | 759.68 |
| 99.93 | 1.2160 | " | 2.720 | 748.4 | 747.01 |
| 100.20 | 1.2157 | " | 2.717 | 747.8 | 744.96 |
| 102.99 | 1.2127 | " | 2.627 | 724.7 | 723.88 |
| 104.09 | 1.2115 | " | 2.589 | 714.9 | 715.54 |
| 107.62 | 1.2075 | " | 2.492 | 690.5 | 687.95 |
| 113.11 | 1.1996 | " | 2.314 | 644.9 | 643.33 |
| 124.32 | 1.1830 | " | 1.930 | 544.9 | 543.99 |
| 130.04 | 1.1742 | " | 1.705 | 484.6 | 487.32 |
| 134.52 | 1.1666 | " | 1.534 | 438.6 | 438.39 |
| 139.26 | 1.1563 | " | 1.309 | 377.2 | 379.96 |
| 143.19 | 1.1442 | " | 1.111 | 323.4 | 323.81 |
| 149.11 | 1.1143 | " | 0.714 | 212.9 | 218.85 |

The calculation of the sound velocity from the measured value of the Brillouin shift ($V = \omega/K$) requires a knowledge of the refractive index of the liquid, since K is given by equation (2.9):

$$K = 2|k|\sin(\theta/2) \qquad (2.9)$$

In equation (2.9) both k, the wave vector of the incident light <u>in</u> the liquid, as well as the angle $\theta$ depend on the refractive index, n. By incorporating the refractive index data for liquid Argon reported by Abbis, et al. (2) and those of Sinnock and Smith (3) we obtained, by interpolation, the temperature dependence of the refractive index at $\lambda = 5145$ Å. These values are also tabulated in Table (5.1) for the specific temperatures of the measurements.

As can be seen from Table (5.1) the Brillouin shifts observed in the forward- and back-scattering differ by about one order of magnitude. However, the calculated sound velocity obtained at these frequencies at the same temperatures agree with each other within the limits of experimental accuracy. This is clearly shown in Figure (5.1) where the calculated values of sound velocity obtained from the different scattering angles are plotted as a function of temperature. The ultrasonic sound velocity, calculated froma polynomial fit to ultrasonic data given by Aziz, et al. (4) are also shown in Table (5.1). A comparison of these values with the present results at

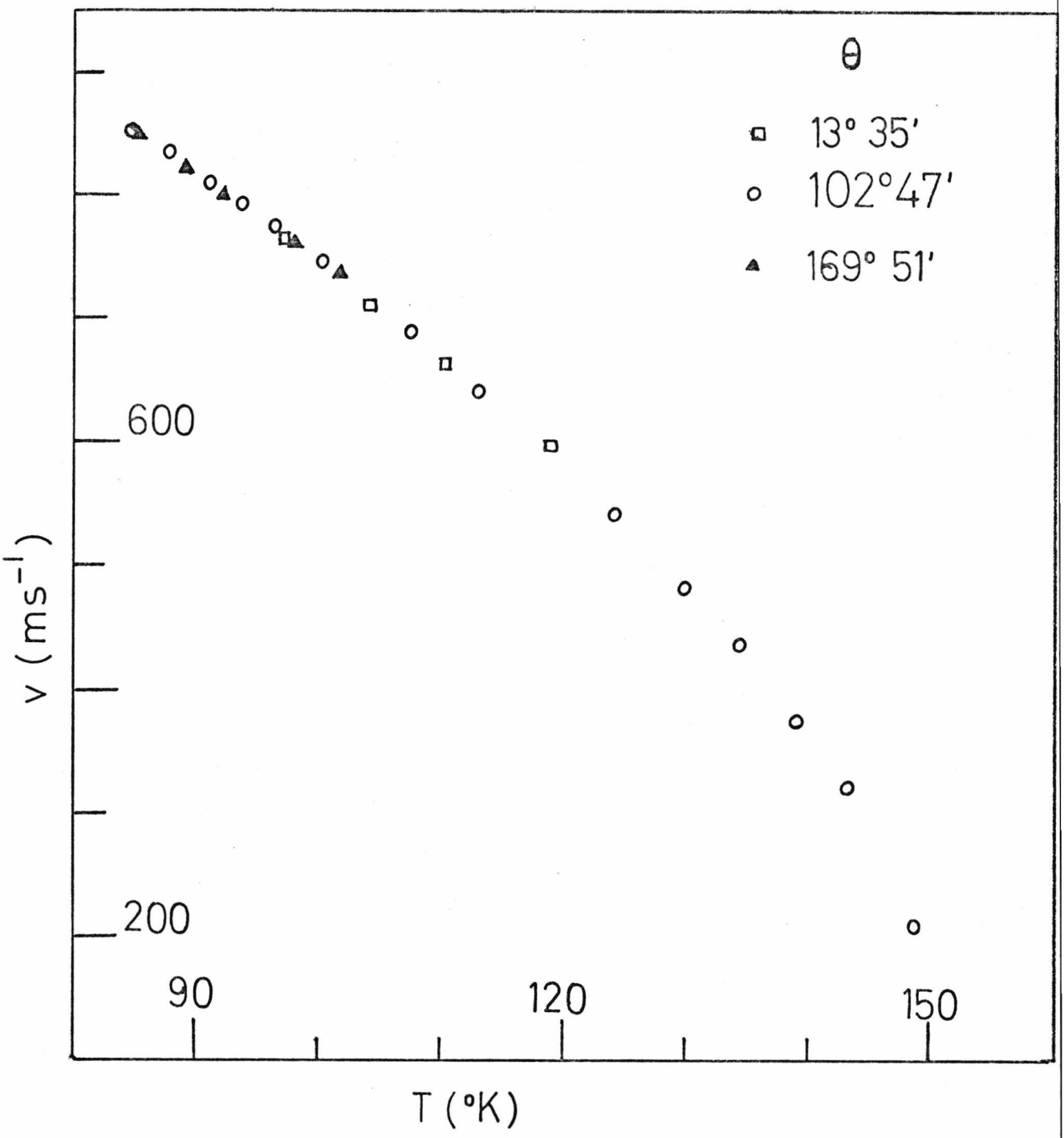


Figure 5.1: Velocity of hypersound in liqud Argon as a function of temperature. (error bars - comparable with point size).

given temperatures agree within the experimental errors.

A fifth order plynomial fit of the velocity data (in the least squares sense) as a function of temperature was obtained. The coefficients were as follows:

$$V(T) = 18968.778634 - (804.355632)\,T + (14.416540)T^2 - (1.295415 \times 10^{-1})T^3 + (5.794631 \times 10^{-4})T^4 - (1.035639 \times 10^{-6})T^5.$$

The function above fits the experimental data within the experimental accuracy over the whole range of the temperatures covered in the experiment.

5.1.3. Sound Attentuation in Liquid Argon

The results of measurements of the Brillouin linewidths in liquid Argon with the high resolution spherical Fabry-Perot (FPS) interferometer are shown in Table (5.2). The Brillouin linewidths were obtained by convoluting Lorentzian lineshapes of various widths with the instrumental profile of the FPS to match the widths of the observed Brillouin lines (Section 4.10.4). A deconvolution method peroposed by La Macchia, et al. (5) was also tried and was found to give the same results as the former method to within ± 3 MHz.

The sound attenuation coefficient, $\alpha$, is calculated using equation (5.1) and is tabulated in Table (5.2) in the usual form of $\alpha$ divided by the square of the frequency ($\alpha/f^2$). The values of $\alpha/f^2$ obtained in these experiments

Table 5.2: Brillouin Linewidth and Sount Attenuation Coefficient in Liquid Argon

| $T(^{o}K)$ ± .02 | $\omega_B$(GHz) ± .010 | $\Delta\omega_B$(MHz) ± 5 | $V(ms^{-1})$ ±2.0 | $\alpha/f^2 x10^{16}$ ($cm^{-1}$ $s^2$) ±10% |
|---|---|---|---|---|
| 85.68 | 4.050 | 61 | 848.4 | 1.42 |
| 89.32 | 3.915 | 63 | 823.3 | 1.56 |
| 92.12 | 3.812 | 62 | 803.6 | 1.67 |
| 97.91 | 3.597 | 56 | 761.9 | 1.77 |
| 99.08 | 3.553 | 59 | 753.3 | 1.93 |
| 101.06 | 3.478 | 58 | 738.5 | 2.01 |
| 107.78 | 3.212 | 57 | 686.7 | 2.51 |
| 108.53 | 3.181 | 57 | 680.7 | 2.59 |
| 109.60 | 3.138 | 58 | 672.1 | 2.69 |

Table 5.3: Bulk Viscosity in Liquid Argon

| $T(^{o}K)$ | $(\alpha/f^2)^{o} x10^{16}$ ($cm^{-1}$ $s^2$) ±10% | $(\alpha/f^2)^{cl} x10^{16}$ ($cm^{-1}$ $s^2$) ±10% | $\eta_s x10^3$ (gm $cm^{-1}$ $s^{-1}$) ±5% | $\eta_B x10^3$ (gm $cm^{-1}$ $s^{-1}$) ±12% | $\eta_B/\eta_s$ ±15% |
|---|---|---|---|---|---|
| 85 | 1.43 | 1.14 | 2.73 | 1.15 | 0.42 |
| 90 | 1.55 | 1.16 | 2.32 | 1.53 | 0.66 |
| 95 | 1.72 | 1.23 | 1.99 | 1.68 | 0.84 |
| 100 | 1.95 | 1.30 | 1.70 | 1.89 | 1.11 |
| 105 | 2.28 | 1.42 | 1.48 | 2.15 | 1.45 |
| 110 | 2.75 | 1.54 | 1.30 | 2.32 | 1.79 |

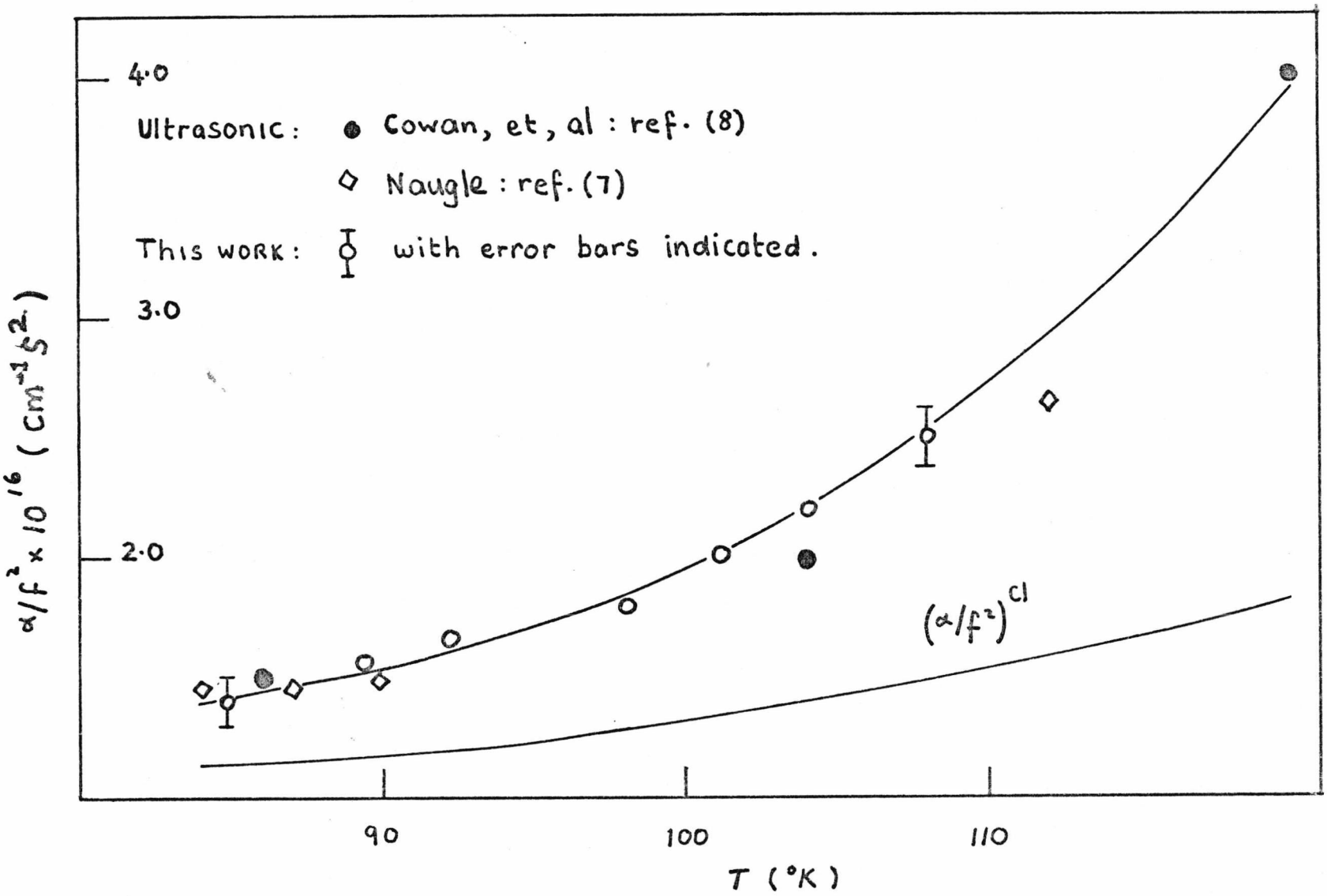


Figure 5.2: Sound attenuation coefficient in liquid Argon.

are accurate to ± 10%.

A comparison of the observed sound attenuation coefficient with the so-called classical attenuation coefficient is shown in Figure (5.2). The classical attenuation coefficient was calculated using equation (1.7) and the various thermodynamic parameters in the equation were obtained from the available data in the literature (6). Also shown in Figure (5.2) are the sound attenuation coefficients in liquid Argon obtained by ultrasonic methods reported by Nangle (7) and Cowan (8). As can be seen from the graph the values obtained in the present work agree with these ultrasonic values within the experimental errors.

The excess attenuation is usually attributed to the bulk viscosity of the medium (9). Thus the bulk viscosity of the liquid could be calculated from the difference between the observed and theoretical classical attenuation coefficients according to the equation:

$$\eta_B = (\rho V^3/2\pi^2) \left[(\alpha/f^2)^0 - (\alpha/f^2)^{cl}\right] \qquad (5.2)$$

where the superscripts $^0$ and $^{cl}$ indicate the observed and classical values respectively. Values of the bulk viscosity of liquid Argon, thus calculated, are shown in Table (5.3) for various temperatures from 85°K to 110°K. The accuracy of the values of $\eta_B$ is estimated to be about ± 12%.

5.1.4. Sound Velocity in Liquid Krypton

The results of measurements of the observed Brillouin shifts of the spectra of light scattered from liquid Krypton, measured at the two scattering angles, are shown in Table (5.4). Because of progressive deterioration of the long-term laser frequency stability by the time these experiments were performed the accuracy of the measured Brillouin shifts in this case was slightly lower than that obtained in the liquid Argon experiments. However, the absolute accuracy of the measured frequency shifts obtained was still better than ±10 MHz.

Available data on the refractive index of liquid Krypton are not as extensive as those of liquid Argon, especially at the higher temperatures. Most measurements have been carried out only within the normal liquid range of the substance. Assuming that the index of refraction is a function of the density only $[n = n(\rho)]$ we have used the data of Sinnock and Smith (3) and Marcoux (10) to extrapolate n to higher temperatures to cover the whole range of temperatures of the experiment. Inevitably this extrapolation is prone to systematic errors, especially towards the upper limit of the temperature range. These calculated values of n, (at the temperatures the spectra were recorded) are also given in Table (5.4). It is expected that there is uncertainty in the last decimal figure in the tabulated values of n.

The hypersonic sound velocity, calculated from the Brillouin shifts, are shown in Table (5.4). Ultrasonic

Table 5.4: Brillouin Shifts and Sound Velocity in Liquid Krypton along the Saturated Vapour Pressure curve

(a) calculated from polynomial fit in reference (4)

| $T(^{o}K)$ ±.02 | n Calc. | $\theta$ ± .5' | $\omega_B$ (GHz) ±.010 | V ($ms^{-1}$) (a) Hypersonic ±4.0 | Ultrasonic ±.06 |
|---|---|---|---|---|---|
| 117.12 | 1.3026 | $169^{o}20'$ | 3.526 | 693.3 | 695.53 |
| 120.44 | 1.2987 | " | 3.423 | 679.8 | 682.25 |
| 121.71 | 1.2974 | " | 3.400 | 675.9 | 677.11 |
| 123.69 | 1.2954 | " | 3.329 | 665.3 | 669.05 |
| 125.26 | 1.2938 | " | 3.307 | 659.1 | 662.61 |
| 129.07 | 1.2902 | " | 3.256 | 650.8 | 646.80 |
| 131.13 | 1.2883 | " | 3.214 | 643.4 | 638.15 |
| 117.97 | 1.3016 | $93^{o}48'$ | 2.536 | 691.4 | 692.15 |
| 120.69 | 1.2984 | " | 2.485 | 679.3 | 681.24 |
| 126.53 | 1.2926 | " | 2.383 | 654.1 | 657.37 |
| 132.35 | 1.2871 | " | 2.289 | 631.0 | 632.99 |
| 139.39 | 1.2798 | " | 2.178 | 603.8 | 602.66 |
| 145.35 | 1.2728 | " | 2.072 | 577.3 | 576.11 |
| 151.10 | 1.2654 | " | 1.953 | 547.1 | 549.60 |
| 157.42 | 1.2567 | " | 1.828 | 515.7 | 519.31 |
| 162.19 | 1.2501 | " | 1.732 | 491.1 | 495.55 |
| 167.99 | 1.2420 | " | 1.613 | 460.4 | 465.44 |
| 174.27 | 1.2334 | " | 1.486 | 427.1 | 431.07 |
| 181.09 | 1.2236 | " | 1.331 | 394.4 | 391.05 |
| 185.65 | 1.2163 | " | 1.225 | 356.9 | 362.20 |
| 191.58 | 1.2047 | " | 1.072 | 319.9 | 321.23 |
| 197.19 | 1.1901 | " | 0.916 | 272.6 | 272.53 |
| 201.48 | 1.1751 | " | 0.847 | 255.2 | (239.70) |

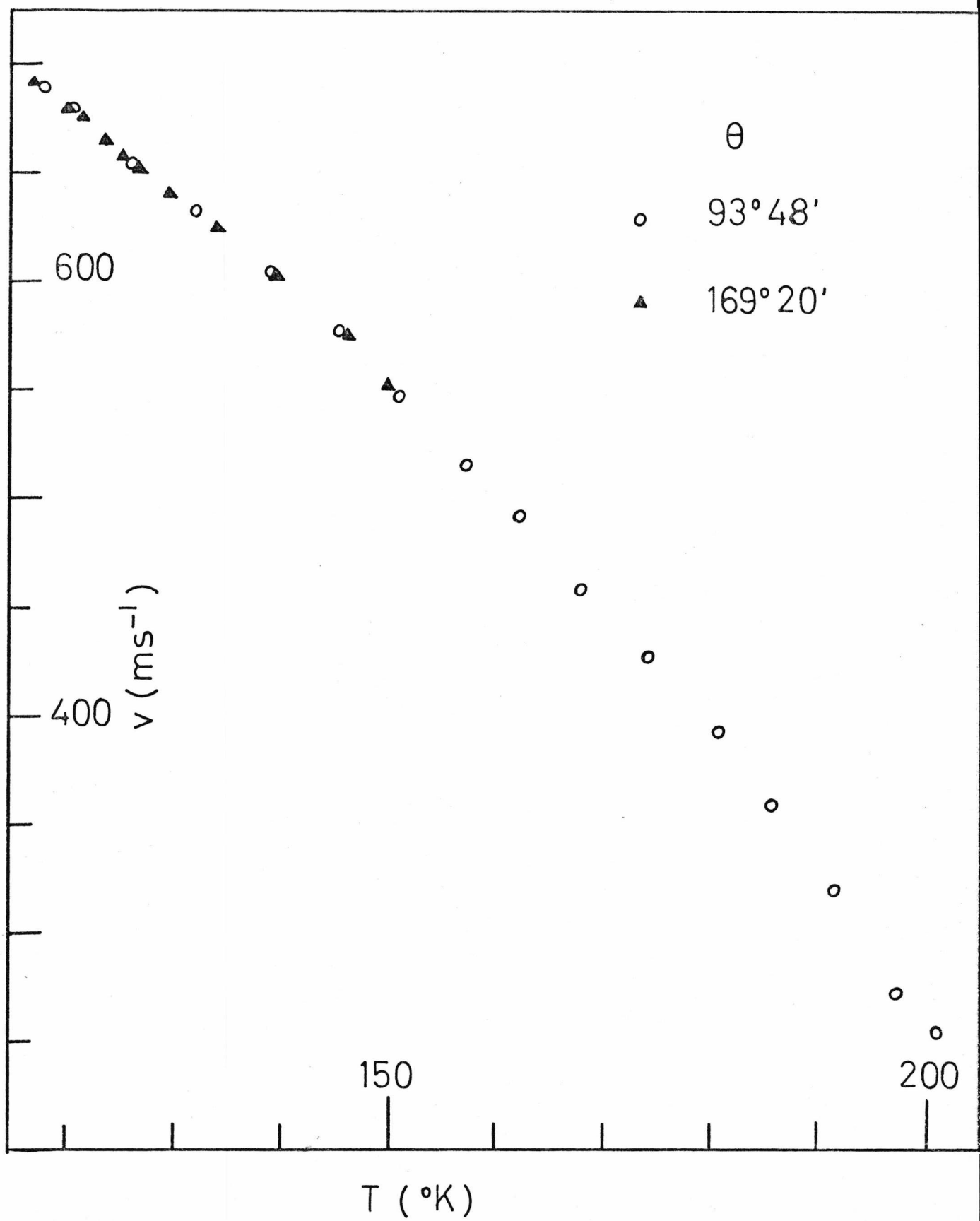


Figure 5.3: Velocity of hypersound in liquid Krypton as a function of temperature. (error bars are comparable with point size).

sound velocity calculated from a polynomial fit given in reference (4) are also given in Table (5.4) for comparison. It can be seen from the table that the hypersonic and ultrasonic data agree within the accuracy of the experiment.

The hypersonic data obtained from the two scattering angles are plotted as a function of temperature in Figure (5.3). This figure illustrates the degree of internal consistency of the two sets of data obtained in this experiment.

A fifth order polynomial fit to the hypersonic data as a function of temperature was obtained. This had the form:

$$V(T) = -843.063454 + (303.092729)T$$
$$-(3.908587)T^2 + (2.473525 \times 10^{-2})T^3$$
$$-(7.771665 \times 10^{-5})T^4 + (9.651464 \times 10^{-8})T^5$$

Table 5.5: Brillouin Linewidth and Sound Attenuation Coefficient in Liquid Krypton

| $T(^{o}K)$ ±.02 | $\omega_B$(GHz) ±.010 | $\Delta\omega_B$(MHz) ± 5 | $V(m\ s^{-1})$ ± 4.0 | $\alpha/f^2 \times 10^{16}$ $(cm^{-1}s^{2})$ ± 10% |
|---|---|---|---|---|
| 117.12 | 3.501 | 62 | 693.0 | 2.32 |
| 120.44 | 3.423 | 63 | 679.8 | 2.49 |
| 121.71 | 3.400 | 62 | 675.9 | 2.48 |
| 125.26 | 3.307 | 62 | 659.1 | 2.70 |
| 126.71 | 3.276 | 62 | 653.8 | 2.78 |
| 129.07 | 3.256 | 63 | 650.8 | 2.85 |
| 131.13 | 3.214 | 63 | 643.4 | 2.99 |

5.1.5. Sound Attenuation Coefficient in Liquid Krypton

Table (5.5) shows the measured Brillouin linewidths of the back-scattering spectra which were frequency analysed with the high resolution FPS. The method of obtaining the linewidths from the spectra was the same as that used in the case of the liquid Argon. The sound attenuation coefficients at various temperatures in liquid Krypton, calculated using equation (5.1) are also shown in Table (5.5). A comparison of the observed sound attenuation coefficient with the 'classical' one is shown in Figure (5.4) (6). At the time of writing, as far as the author could ascertain, there is no previous report of measurements of the sound attenuation coefficient in liquid Krypton either by ultrasonic or light scattering method. Thus there is no comparison available for the present data.

The bulk viscosity of liquid Krypton at various temperatures from 116$^{o}$K to 130$^{o}$K was calculated from the observed 'excess' attenuation using equation (5.2). These are shown in Table (5.6).

5.1.6. Discussion

We have analysed the spectra of light scattered inelastically from liquid Argon and liquid Krypton in terms of the first order approximation as discussed in Chapter II. In this approximation the Brillouin shift is a linear function of the scattering vector, $\omega_0 = KV$; and using

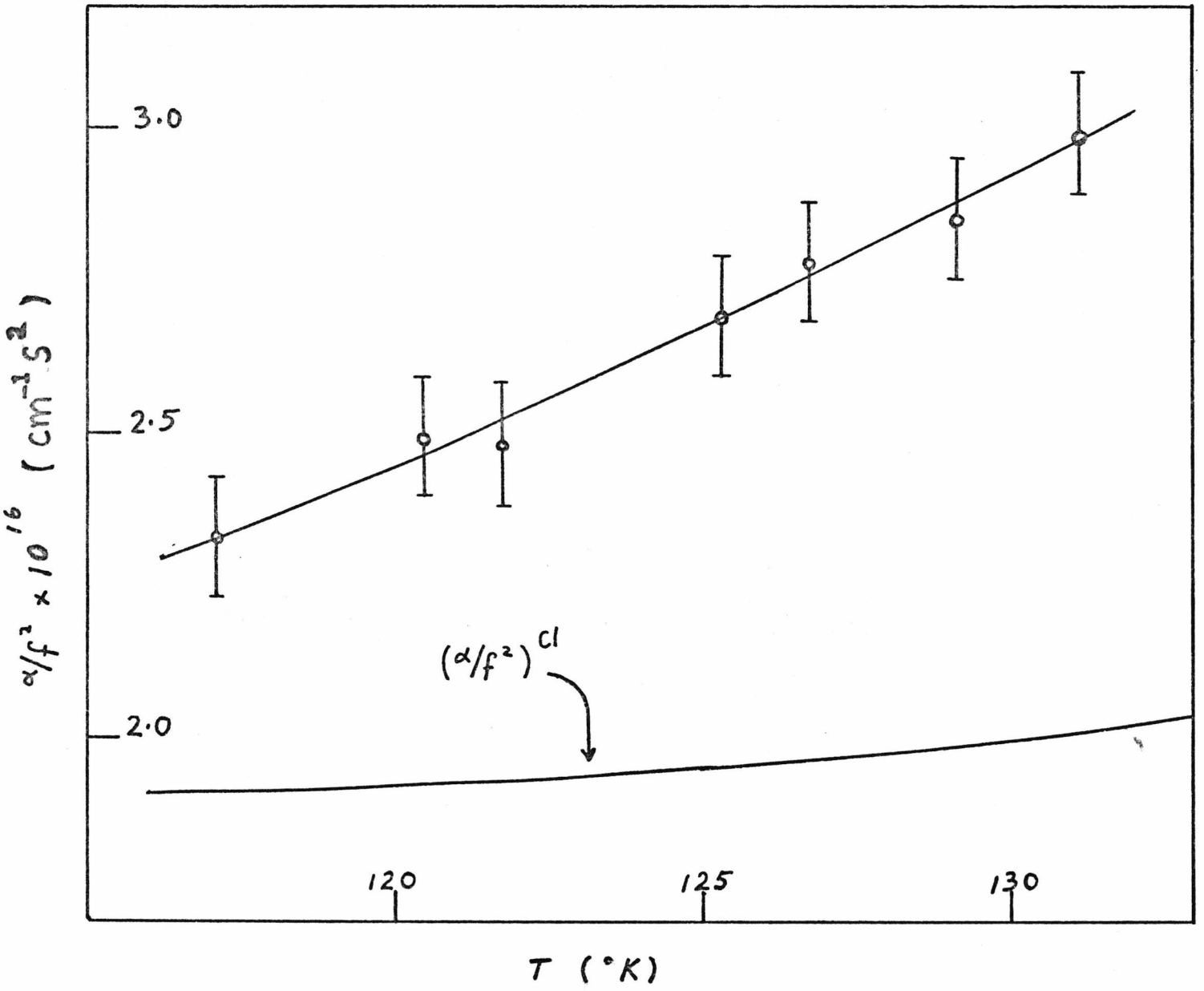


Figure 5.4: Sound attenuation coefficient in liquid Krypton.

Table 5.6: Bulk Viscosity in Liquid Krypton

| T ($^{o}$K) | $(\alpha/f^2)^{0} \times 10^{16}$ ($cm^{-1}$ $s^2$) ±10% | $(\alpha/f^2)^{Cl} \times 10^{16}$ ($cm^{-1}$ $s^2$) ±10% | $\eta_s \times 10^3$ ($gcm^{-1}s^{-1}$) ±5% | $\eta_B \times 10^3$ ($gcm^{-1}s^{-1}$) ±10% | $\eta_B/\eta_s$ ±15% |
|---|---|---|---|---|---|
| 116.0 | 2.29 | 1.83 | 4.47 | 1.94 | 0.43 |
| 118.0 | 2.36 | 1.84 | 4.23 | 2.13 | 0.50 |
| 120.0 | 2.44 | 1.85 | 4.04 | 2.27 | 0.56 |
| 125.0 | 2.67 | 1.92 | 3.67 | 2.62 | 0.71 |
| 130.0 | 2.93 | 2.00 | 3.37 | 2.93 | 0.87 |

this approximation we calculated the sound velocity in these liquids from the measured frequency shifts. The frequency shift $\omega_0$ is taken to be the position of the peak of the Brillouin line on the frequency scale. In cases where there is visible appearance of line overlapping the frequency shift $\omega_0$ is taken to be the corrected position of the peak. Our results show that within the limits of experimental accuracy there is no dispersion of the sound velocity in these liquids in the frequency range from about 1MHz to about 3 to 4 GHz, as evidently shown by the agreement between the hypersonic and ultrasonic velocity data. However, it should be emphasised that theoretical calculations by Boon and De Guent (11) showed that the expected dispersion of the sound velocity in liquid Argon at frequencies of the order

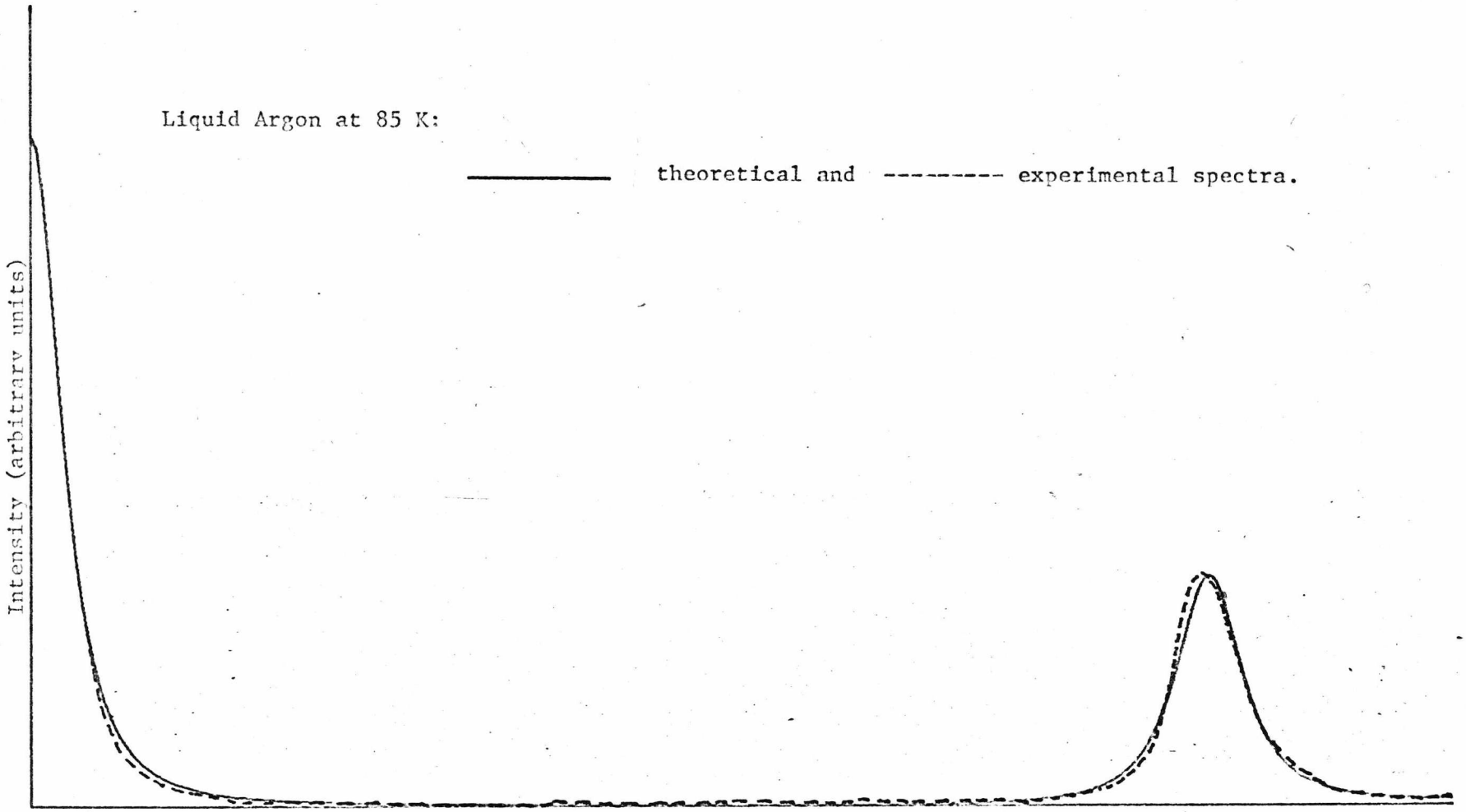


Figure 5.5: Typical comparison of theoretical and experimental spectra of light scattered from liquid Argon.

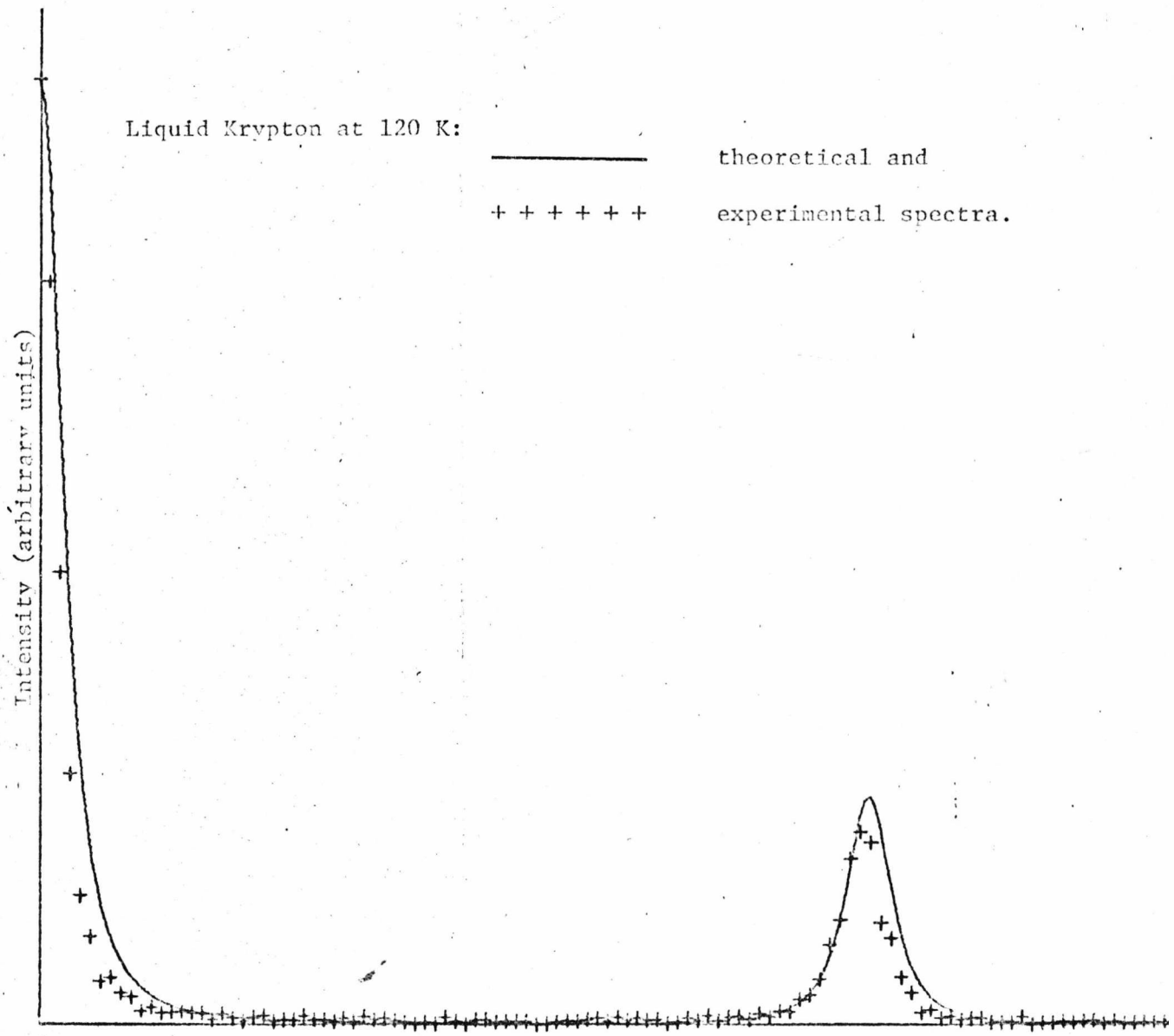


Figure 5.6: Typical comparison of theoretical and experimental spectra of light scattered from liquid Krypton.

of 3 GHz to be about .001%. This magnitude of dispersion is not measurable with the present instrumental technique (12).

We have also calculated theoretical spectra, according to equation (2.44), for these liquids and compared them with the experimentally observed spectra. These are shown in Figures (5.5) and (5.6) for liquid Argon and liquid Krypton respectively. The theoretical spectra has been convoluted with the transmission function profile, $M(\omega)$ of the FPP, which was discussed in Section (4.3.3.) These figures show that the agreement between the theoretical and experimental spectra is quite reasonable, apart from the slightly broader central line in the theoretical spectra. This can be attributed to an error in the representation of the instrumental profile, $M(\omega)$. The shift of the Brillouin line of the theoretical spectra and that of the observed agree within the accuracy of the experiment. Thus we can conclude that the spectrum of light scattered from these simple monatomic liquids can be described adequately by the first order approximation to the solution of the dispersion equation, $D(s)$.

The bulk viscosities of liquid Argon and liquid Krypton increase with temperature, as compared with the shear viscosities which decrease with temperature. Thus the ratio of bulk to shear viscosities in these liquids increases with temperature. In liquid Argon this varies from 0.42 at $85^{o}K$ to 1.79 at $110^{o}K$, while in liquid Krypton it varies from 0.43 to 0.87 in the temperature range $116^{o}K$ to $130^{o}K$.

Kinetic theory calculation for a system of hard spheres show the ratio of bulk to shear viscosity to be 5/3 (13). Rice and Gray have calculated the ratio of bulk to shear viscosity in liquid Argon using the Rice-Allnatt theory of transport coefficients and they found this value to be 1.33 (13). Thus quantitative agreement between the theoretical and experimental values of the bulk viscosity is fairly good.

The principle of corresponding states could be used to compare the properties of these liquids. According to the principle of corresponding states similar properties of substances which interact with similar forces of interaction should lie on the same line when expressed in reduced form. These monatomic liquids have been known to obey closely the Lennard-Jones interaction. In Figure (5.7) we have plotted the ratio of bulk to shear viscosity of liquid Argon and Krypton as a function of the reduced density,

$$\rho^* = \left(\frac{\sigma^3}{m}\right)\rho \qquad (5.3)$$

where $\sigma$ is the radius parameter of the Lennard-Jones potential and m is the atomic mass of the liquid. Figure (5.7) shows that the data for Argon and Krypton do not lie on the same line but they do lie in approximately parallel lines. This discrepency could perhaps be attributed to 'quantum effects'. We have also

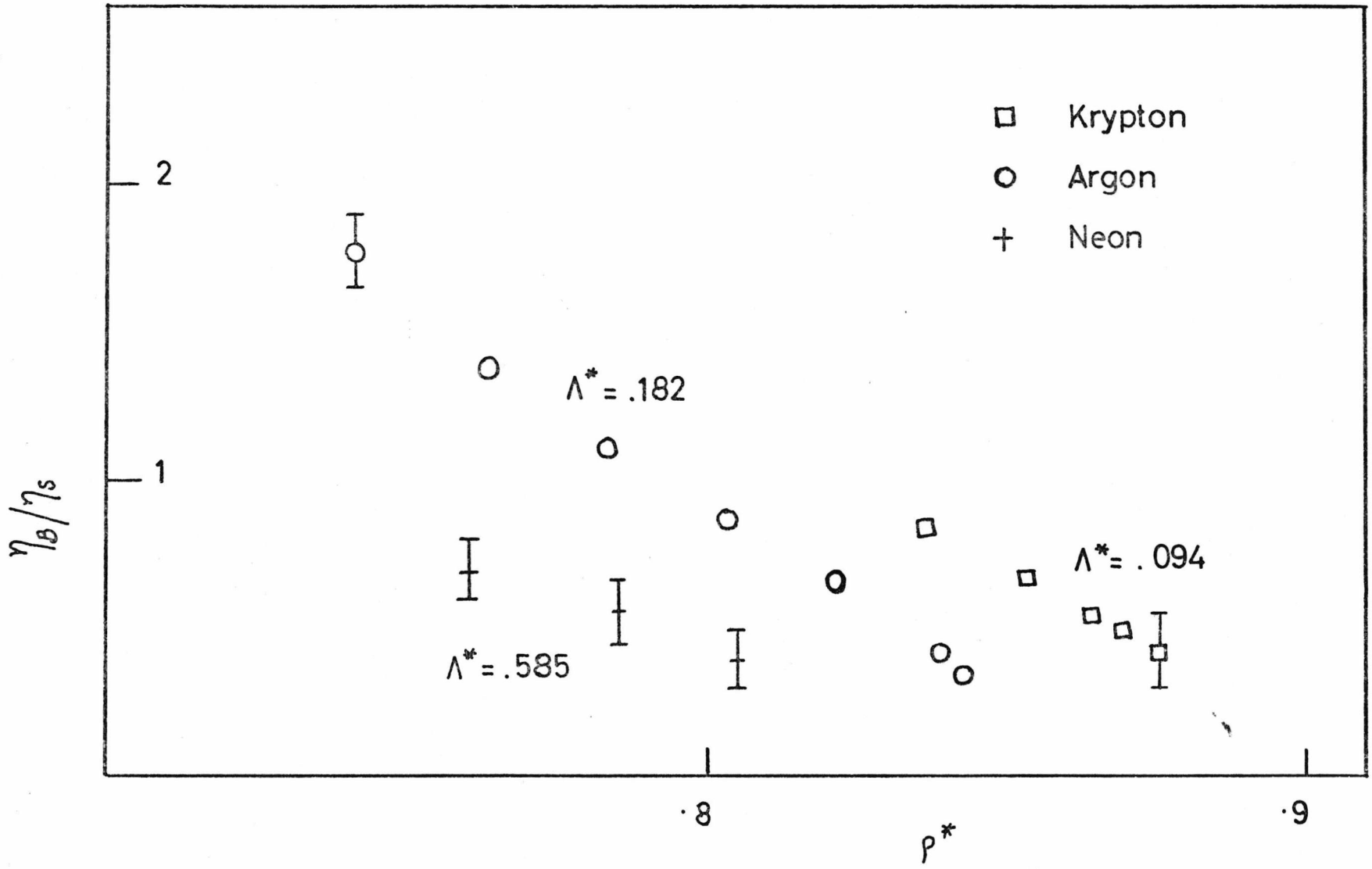


Figure 5.7: Ratio of bulk to shear viscosity in liquids Neon, Argon and Krypton as a function of the reduced density, $\rho^*$. ( $\Lambda^*$ is the 'Quantum parameter' of the respective element).

plotted in Figure (5.7) the values of the bulk to shear viscosity ratio of liquid Neon obtained by Larson, et al. using ultrasonic technique (14). The inclusion of these results seems to indicate a tendency for the ratio of bulk to shear viscosity to decrease with increase in the so called quantum parameter, $\Lambda^*$. $\Lambda^*$ here is given by

$$\Lambda^* = \frac{h}{\sigma (m\varepsilon)^{\frac{1}{2}}} \qquad (5.4)$$

where h is the Planck's constant and $\varepsilon$ is the potential well energy parameter. The values of $\Lambda^*$ for Neon, Argon and Krypton are indicated adjacent to the corresponding points on the graph (Figure 5.7)

## 5.2. Binary Gas Mixtures

### 5.2.1. Introduction

We have observed Brillouin scattering of light in two binary monatomic gas mixtures: Krypton-Helium and Argon-Neon. In the Kr-He mixture the maximum mass concentration of He in the mixture was 0.03 while for the A-Ne mixture the maximum Ne concentration was 0.3.

In the case of the Kr-He system we have investigated the scattering of light both as a function of the concentration of the lighter component as well as a function of the scattering vector, $\bar{K}$. This involved two sets of experiments:

(a) measurements were made at a fixed scattering angle ($\theta = 88^{o}37' \pm 0.5'$) while the He concentration was varied, and

(b) measurements were made at a fixed concentration ($C = 0.01$) at various scattering angles.

In the latter case the wavelength of the laser light was also varied. This enabled data to be collected over a slightly larger range of scattering vectors. The 4880 $\mathring{A}$ and 5145 $\mathring{A}$ lines of the Argon ion laser were used. This procedure minimised the need to change the scattering angles. The overall range of scattering vectors covered was from 0.64 to 2.02 ($x10^{5}$ $cm^{-1}$).

Measurements on the A-Ne mixture were performed only at one fixed scattering angle, $\theta = 104^{o}55'$ ($\pm$ 0.5). This was because theoretical calculations predicted that the dispersion of the sound velocity in this system to be very small (refer to Chapter III), Section 3.5).

The accuracy of measurements of the Brillouin frequency shift is $\pm$ 1% and the linewidth $\pm$ 10%.

### 5.2.2. Measurements on Kr-He Mixture

The results of measurments of Brillouin shifts and linewidths from the Kr-He mixture as a function of concentration are shown in Table (5.7). The velocities of sound in the mixture were calculated from the measured frequency shifts. These are compared with the adiabatic,

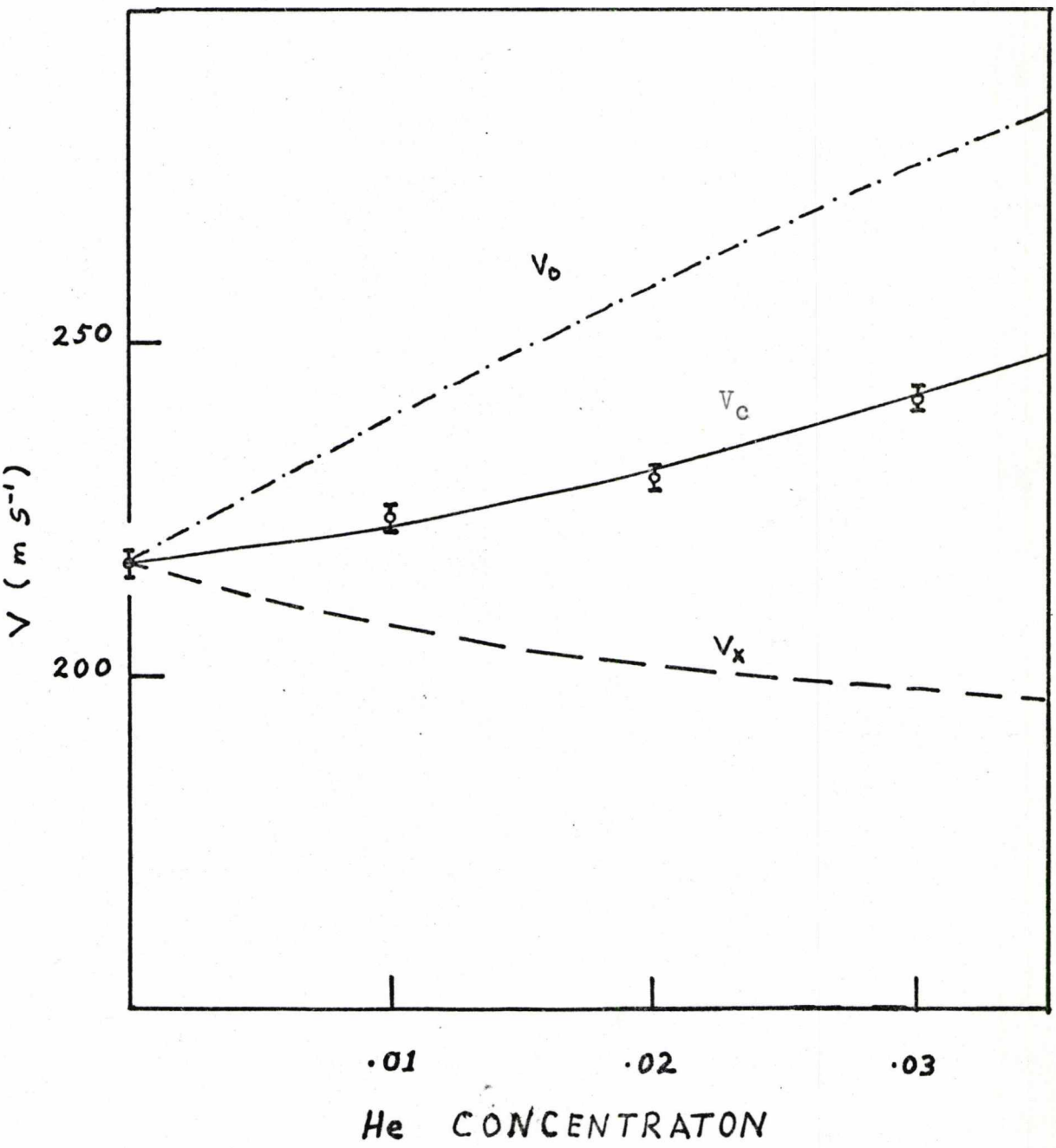


Figure 5.8: The velocity of sound in Kr-He mixture as a function of concentration.

$V_0$ and theoretical, $V_c$, sound velocities in Table (5.7) and Figure (5.8). The theoretical sound velocity, $V_c$ is obtained by solving the dispersion equation (3.47) numerically and setting:

$$V_c = \text{Im}\ (s)\ K^{-1} \tag{5.5}$$

As can be seen from Figure (5.8) the experimental sound velocity data agree with the calculated $V_c$ within experimental errors.

Table 5.7: Brillouin Shifts and Sound Velocity in Kr-He mixture as a function of concentration

| Krypton Pressure = 5.21 atm.; $K = 1.705 \times 10^5 cm^{-1}$ | | | | | |
|---|---|---|---|---|---|
| He concentration | $\omega_B$ (MHz) ± 10 | $\Delta\omega_B$ (MHz) ± 5 | $V(ms^{-1})$ ± 4 | $V_c(ms^{-1})$ (calculated) | $V_0(ms^{-1})$ (calculated) |
| 0.00 | 591 | 37 | 218 | 220 | 220 |
| 0.01 | 615 | 96 | 224 | 223 | 239 |
| 0.02 | 623 | 115 | 230 | 231 | 258 |
| 0.03 | 657 | 137 | 242 | 242 | 277 |

The measured linewidth data in Table (5.7) are plotted as a function of concentration in Figure (5.9). The broken line through the data points is drawn to

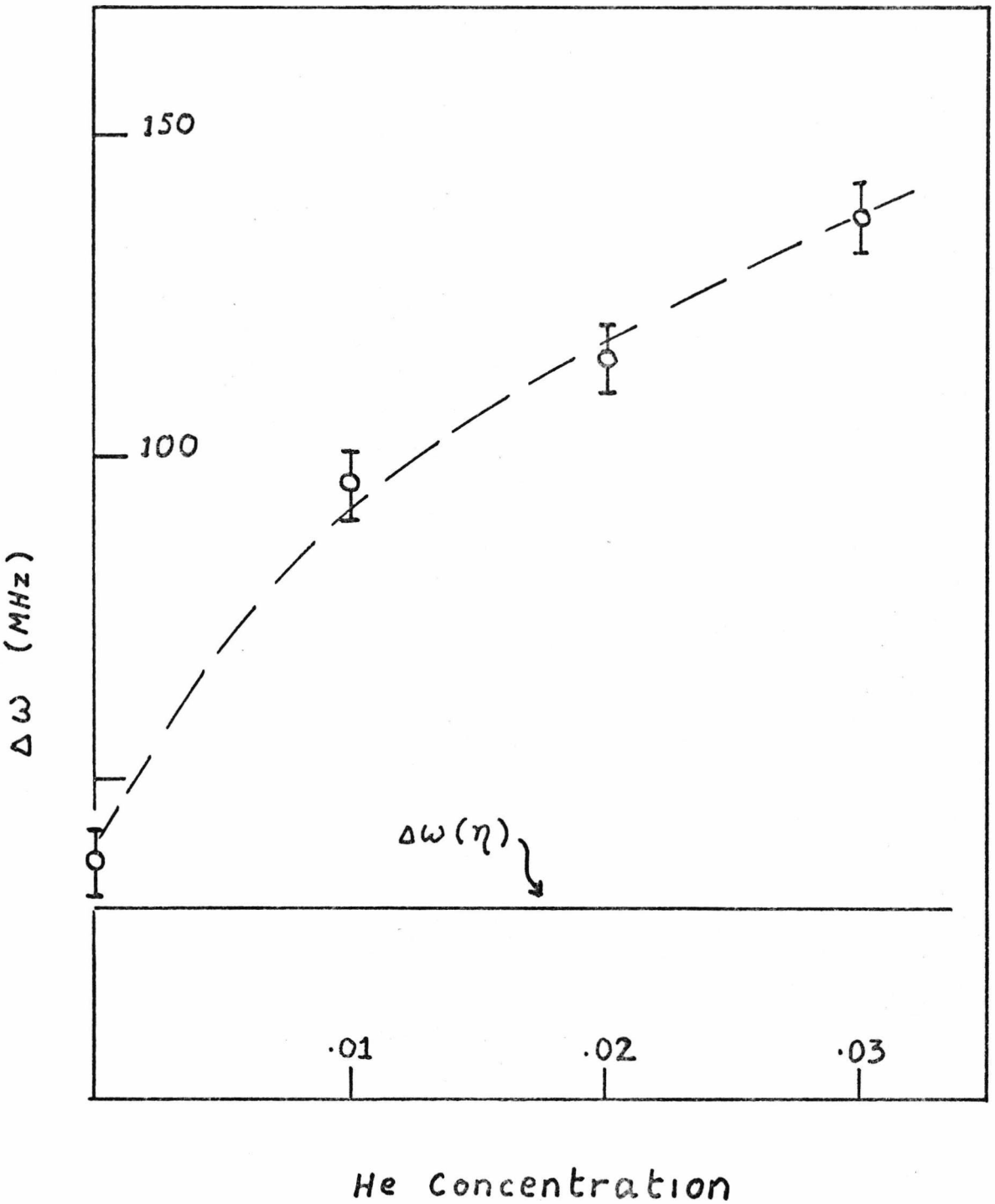


Figure 5.9: Brillouin linewidth of light scattered from Kr-He mixture as a function of concentration.

guide the eye. The contribution of viscous damping to the linewidth, $\Delta\omega(\eta)$ (refer to equation 3.25) is represented by the continuous line. The viscosity data of Kestin, et al. (15) were used to calculate this contribution. The diffusion contribution to the linewidth can be obtained by subtracting from the observed linewidth, $\Delta\omega^0$, the viscosity contribution, $\Delta\omega(\eta)$. (This is possible because the thermal conductivity contribution can be assumed to be small.)

From the calculated values of the diffusion broadening we have estimated themutual diffusion coefficient, $D_{12}$, for the mixture using the equation:

$$D_{12} = 4\pi\left\{\Delta\omega^0 - \Delta\omega(\eta)\right\}\frac{\rho_0^2}{V^2}\,\frac{(\partial\mu/\partial C)}{(\partial\rho/\partial C)^2}\,K^{-2} \qquad (5.6)$$

where $\rho_0$, $(\partial\mu/\partial C)$ and $(\partial\rho/\partial C)$ are calculated from the definitions (3.7) and equations (3.35) and (3.36). The values of $D_{12}$ obtained from this procedure are shown in Table (5.8) and these are compared with $D_{12}$ (calc.), where $D_{12}$ (calc.) is the theoretical value of the mutual diffusion coefficient for the Lennard-Jones potential, given by the equation (16):

$$D_{12}\ (\text{calc.}) = 0.002680\,\frac{\sqrt{T^3(M_1 + M_2)/2M_1 M_2}}{P\ \sigma_{12}^2\ \Omega_{12}^{(1,1)*}\ (T^*)} \qquad (5.7)$$

where T is the temperature,

$M_i$ is the molecular weight of component i

P is the pressure in atmospheres,

$\sigma_{12}$ is the averaged radius parameter of the interaction potential in $\mathring{A}$

$\Omega_1^{(1,1)*}$ is a function of the interaction potential of the atoms. These are tabulated in Table I-M in reference (16)

T* is the reduced temperature $= Tk_B/\varepsilon_{12}$

Table 5.8: Mutual Diffusion Coefficient ($D_{12}$) of Kr-He mixture

| He Concentration | $D_{12}$ (calc.) ($cm^2\ s^{-1}$) | $D_{12}$ (Expt.) ($cm^2\ s^{-1}$) $\pm .02$ |
|---|---|---|
| 0.01 | .100 | .17 |
| 0.02 | .085 | .09 |
| 0.03 | .074 | .07 |

The experimental and theoretical values of $D_{12}$ agree in magnitude and corresponding concentration dependence, as can be seen from Table (5.8).

The results of the measurements from the Kr-He mixture at various scattering vectors are shown in Table (5.9) and plotted in Figure (5.10). The smooth line in Figure (5.10) is that of the theoretical values of $V_c$,

Table 5.9: Brillouin Shift and Sound Velocity in Kr-He Mixture as a function of K

| C = 0.01 | | |
|---|---|---|
| $Kx10^{-5}$ ($cm^{-1}$) | $\omega$(MHz) ±10 | $V(ms^{-1})$ ±4 |
| 0.64 | 240 | 236 |
| 0.67 | 254 | 235 |
| 1.11 | 401 | 228 |
| 1.28 | 459 | 224 |
| 1.44 | 507 | 222 |
| 1.52 | 536 | 222 |
| 1.71 | 597 | 219 |
| 1.92 | 660 | 217 |
| 2.02 | 697 | 216 |

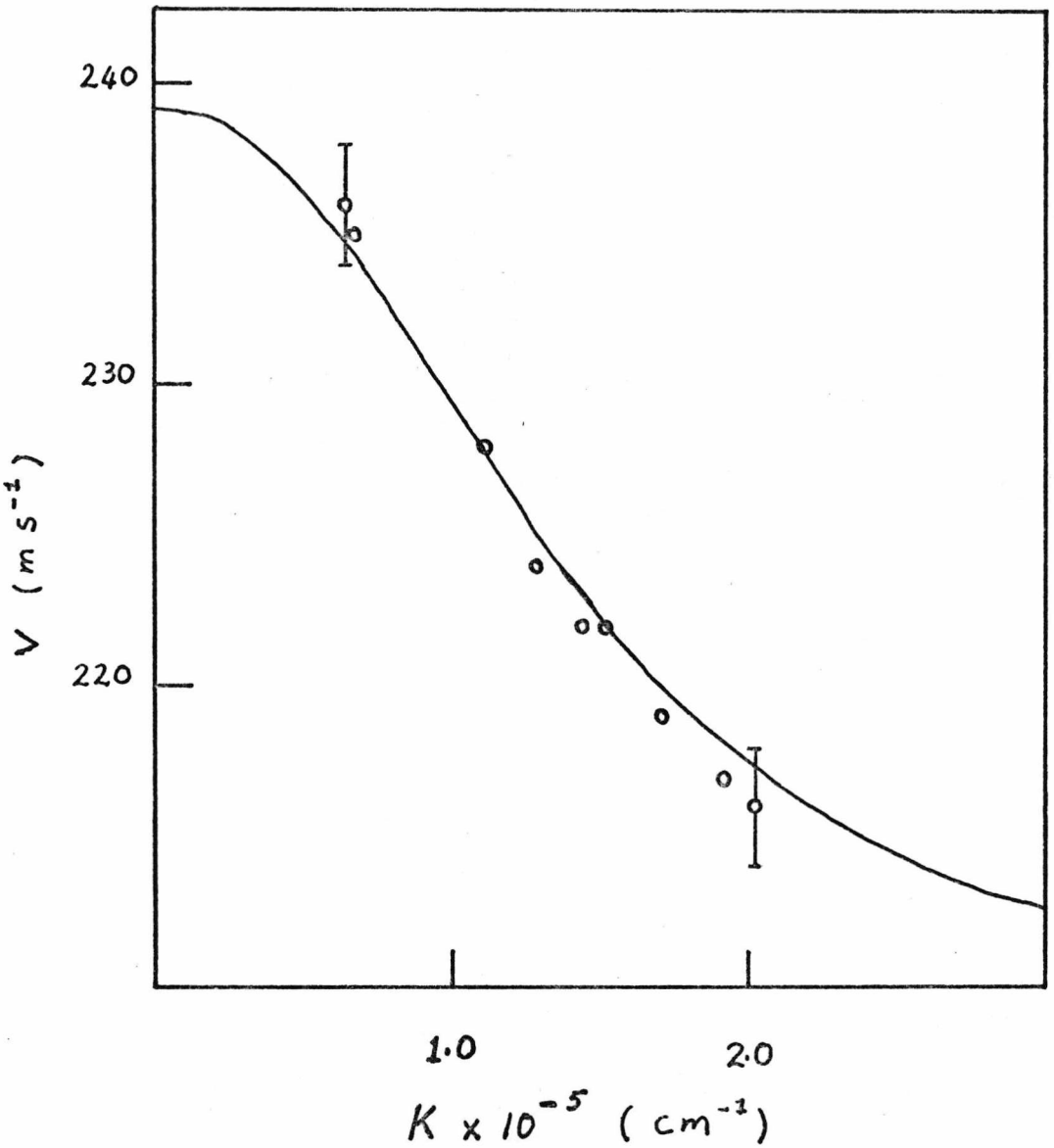


Figure 5.10: Sound velocity in Kr-He mixture as a function of the scattering vector.

calculated in the way described before (equation 5.5).

As can be seen from Figure (5.10) the observed sound velocities agree with $V_c$ within the experimental errors.

### 5.2.3. Measurements on A-Ne Mixture

Table (5.10) shows the results of measurements on the A-Ne mixture. The experimental results were treated in the same way as were the results from the Kr-He mixture, described in the previous section. The data from the sound velocity calculations are plotted in Figure (5.11).

Table 5.10: Brillouin shifts and sound velocity in A-Ne mixture as a function of concentration

| Argon Pressure = 6.45 atm.; $K = 1.915 \times 10^5$ cm$^{-1}$ | | | | | |
|---|---|---|---|---|---|
| Ne Concentration ±.05 | $\omega_B$ (MHz) ±10 | $\Delta\omega_B$ (MHz) ±5 | $V$ (ms$^{-1}$) ±4 | $V_c$ (ms$^{-1}$) (Calculated) | $V_0$ (ms$^{-1}$) |
| 0.00 | 972 | 59 | 319 | 319 | 319 |
| 0.06 | 994 | 64 | 326 | 324 | 326 |
| 0.10 | 1011 | 72 | 332 | 330 | 334 |
| 0.15 | 1021 | 90 | 335 | 336 | 342 |
| 0.20 | 1045 | 97 | 343 | 343 | 349 |
| 0.25 | 1068 | 116 | 350 | 351 | 356 |
| 0.30 | 1093 | 120 | 359 | 358 | 364 |

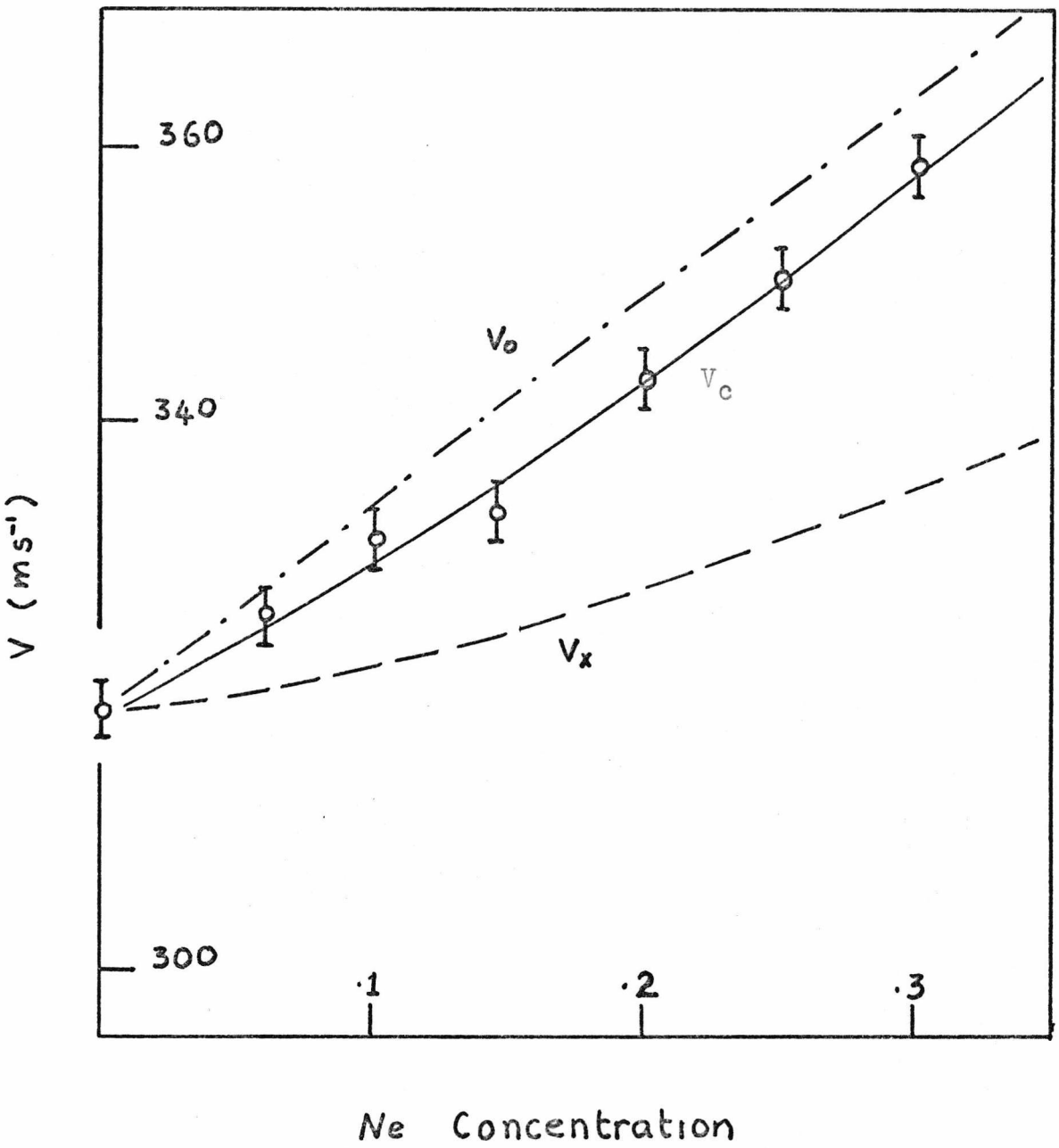


Figure 5.11: The velocity of sound in A - Ne mixture as a function of concentration.

The experimental sound velocity data agree with the predicted values within the experimental accuracy. This is clearly indicated by Figure (5.11).

The measured Brillouin linewidths are plotted as a function of concentration in Figure (5.12). The broken line through the points is drawn only to guide the eye. We have also shown the contribution to the linewidth expected from the viscosities. This is indicated by the smooth line in the graph. The viscosity line in the graph may be in error by as much as 15%. This is because experimental data are unavailable, and the viscosity of the mixture was obtained by direct interpolation of the viscosities of the pure components using the euqation:

$$\eta = \sum_i x_i \eta_i \qquad (5.8)$$

where $x_i$ and $\eta_i$ are the molar fraction and viscosity of component i respectively. This procedure was felt justifiable because the contribution of the viscosity term to the linewidth varies very slowly with concentration. This is because the viscosity contributes to the linewidth in the form of $\eta/\rho$, and the density, $\rho$ increase with concentration.

The mutual diffusion coefficient, $D_{12}$ of the mixture was estimated in a similar way as described for the Kr-He mixture. The results are tabulated in Table (5.11), where the experimental results are compared with the theoretical

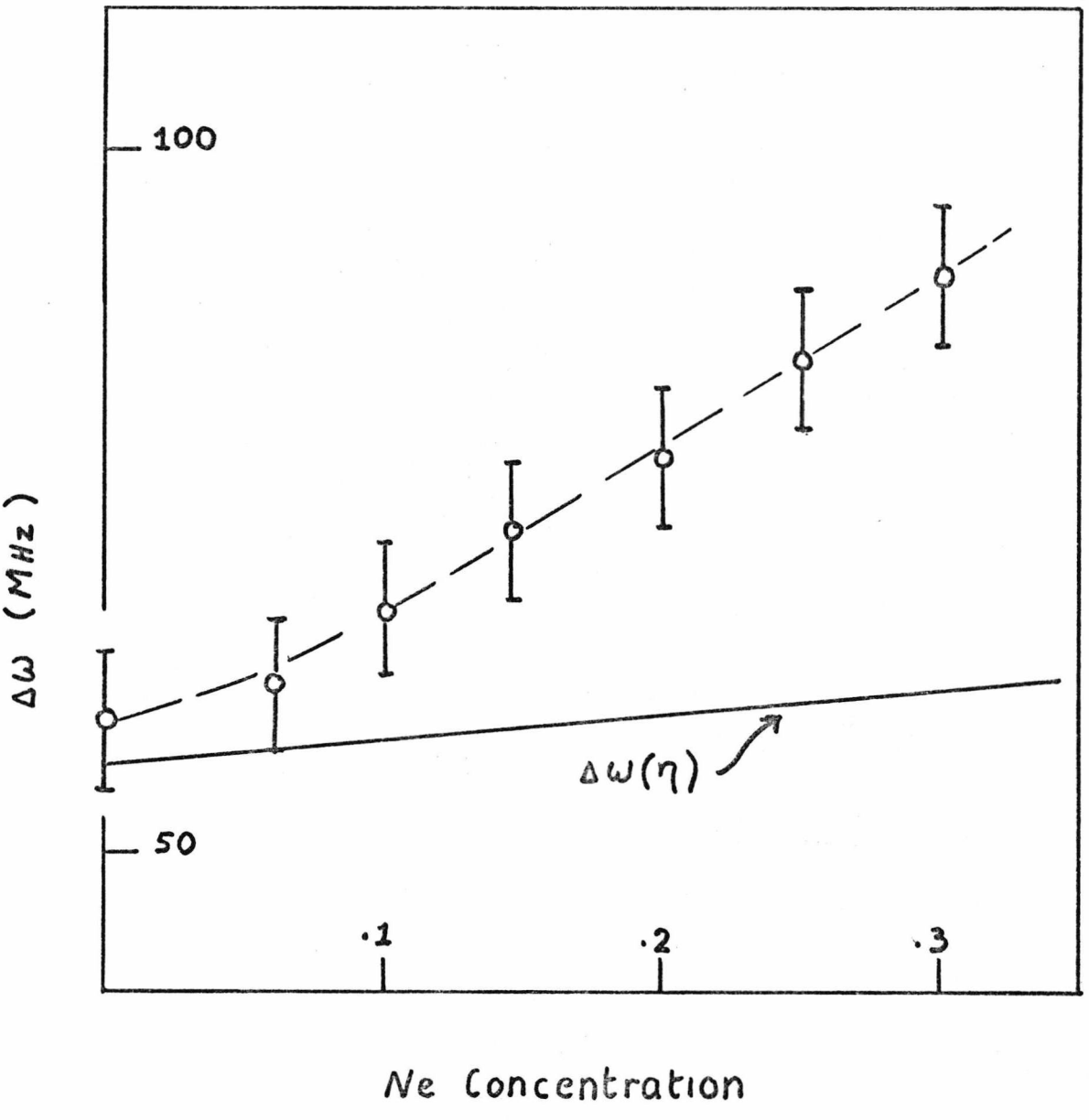


Figure 5.12: Brillouin linewidth of light scattered from A-Ne mixture as a function of concentration.

values, $D_{12}$ (calc.). Table (5.11) shows a deviation of the experimental values of $D_{12}$ from the theoretical values for concentrations greater than 0.1. Further increase in concentration produced an increase in the value of $D_{12}$ while it is predicted that $D_{12}$ should decrease with concentration (effectively the pressure).

Table 5.11: Mutual Diffusion Coefficient ($D_{12}$) of A-Ne Mixture

| Ne Concentration | $D_{12}$ (calc.) ($cm^2\ s^{-1}$) | $D_{12}$ (Expt.) ($cm^2\ s^{-1}$) $\pm .01$ |
|---|---|---|
| .05 | .042 | .04 |
| .10 | .040 | .04 |
| .15 | .036 | .04 |
| .20 | .032 | .05 |
| .25 | .029 | .05 |
| .30 | .025 | .06 |

## 5.2.4 Discussion

### 5.2.4.1 Spectrum of light scattered from binary gaseous Mixtures

Our experimental results on the Kr-He and A-Ne mixtures show that the velocity of propagation of sound

waves in these mixtures is lower than that calculated for the adiabatic sound velocity, $V_0$. However, the agreement of the observed sound velocities in the two mixtures with that predicted theoretically assuming coupling between the sound modes and the diffusion modes is very good. Also in the case of the Kr-He mixture the observed dispersion of the sound velocity agrees very well with that predicted by the same theory, over the range of scattering vectors at which the experiment was performed.

In the Kr-He system the range of concentrations and scattering vectors over which the experiment could be performed were dictated by the properties of the mixture. For concentrations higher than 0.03 (the maximum in this work) the excessive broadening of the lines made it impossible to resolve discrete peaks in the spectrum. This is illustrated by the series of spectra in Figure (5.13). This led to a difficulty of interpreting the spectrum at higher concentrations, i.e. we can no longer treat it as being the result of discrete energy transport processes.

The limit of the scattering vector, K, is dictated by the mean free path of the system. As K is increased we observed the transition of the scattering process from the hydrodynamic to the kinetic limit, as illustrated by the spectra in Figure (5.14). The scattering process can then no longer be treated by purely hydrodynamic theories.

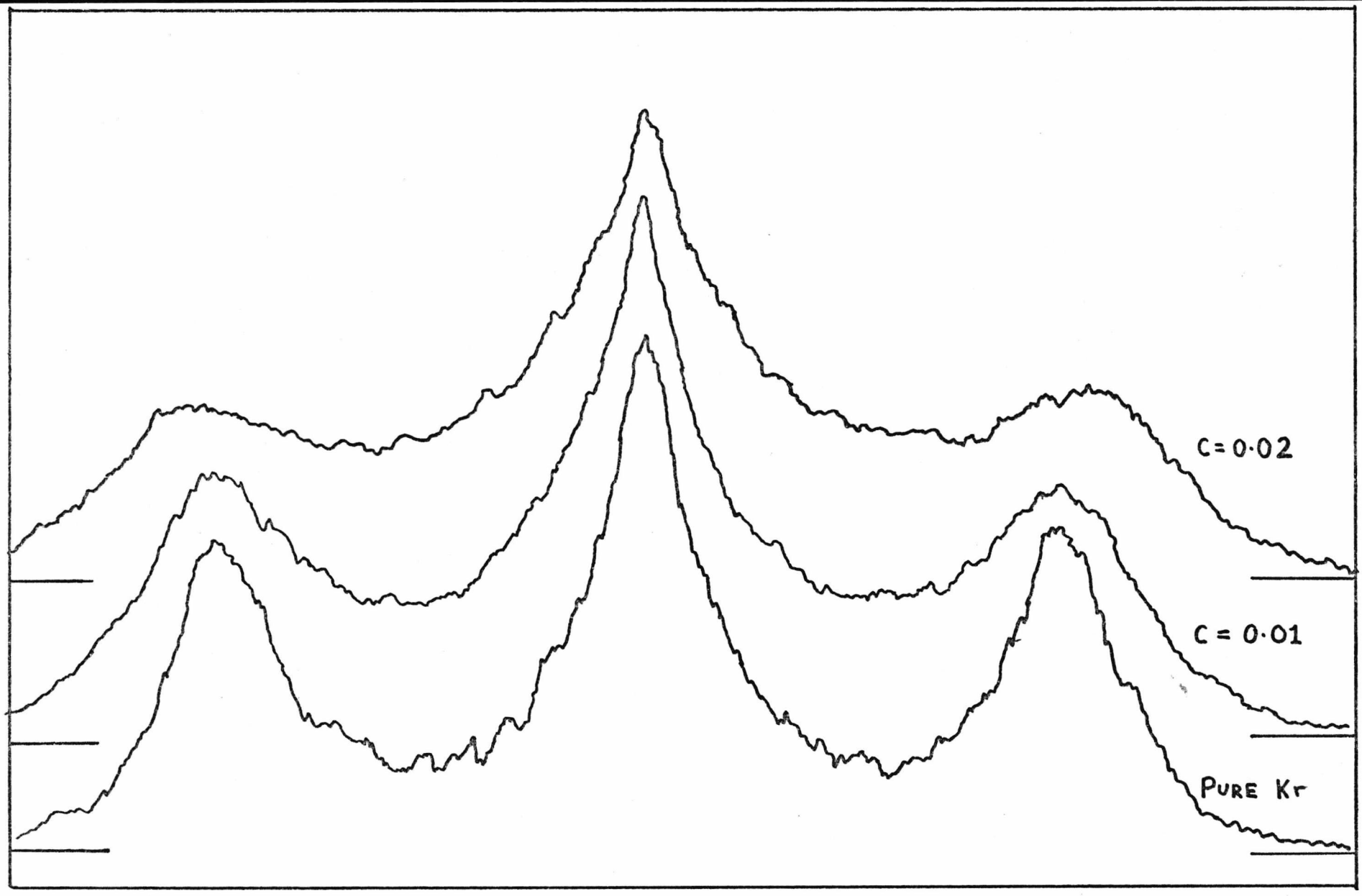


Figure 5.13: Spectra of light scattered from Kr-He mixture at various concentration s.

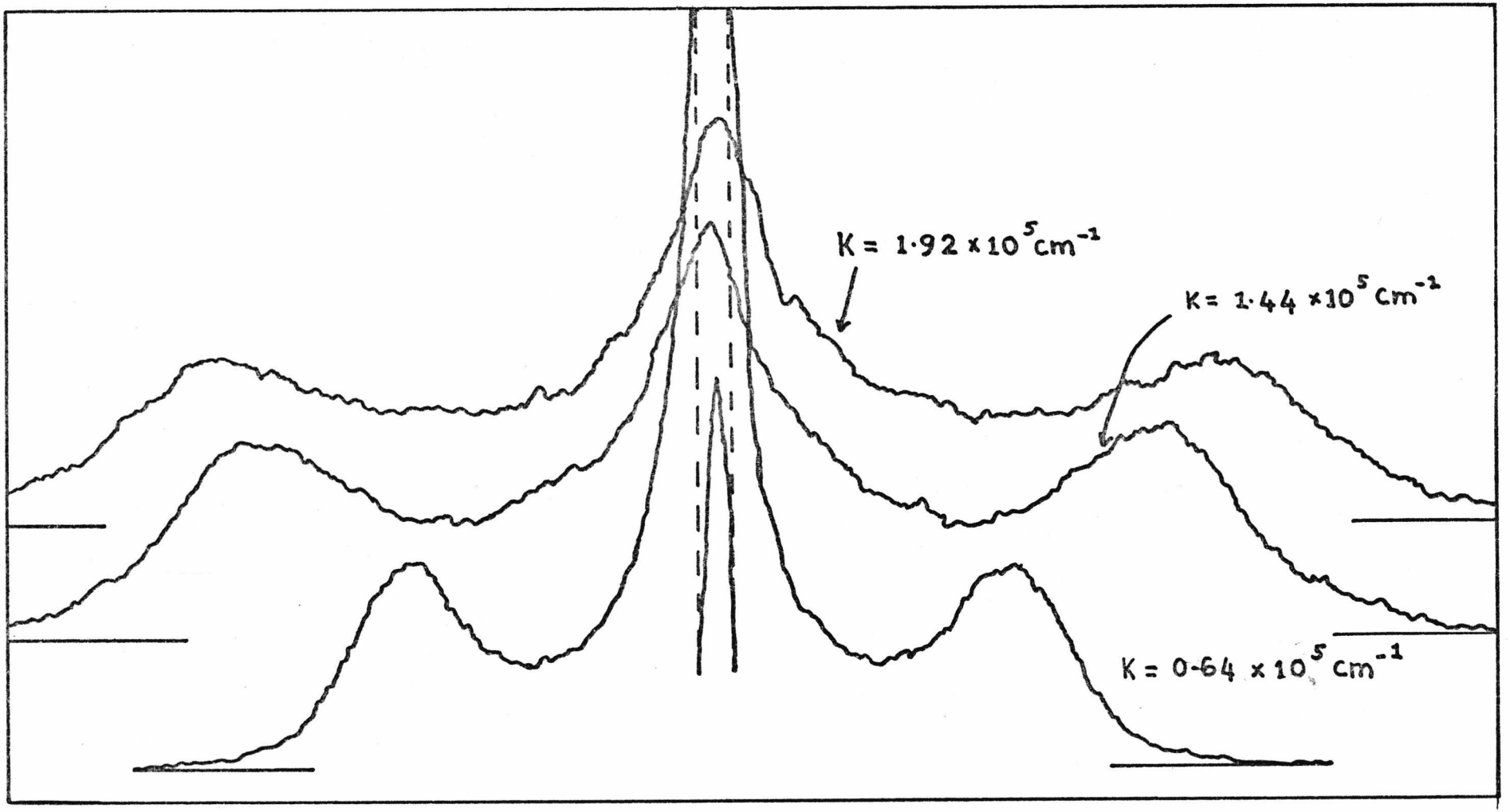


Figure 5.14: Spectra of light scattered from Kr-He mixture at various scattering angles (i.e. scattering vectors).

5.2.4.2. Calculation of Atomic Radius from $D_{12}$ (17)

From table (5.8) we see that the observed values of $D_{12}$ for the Kr-He system shows reasonable agreement in magnitude as well as corresponding pressure dependence with the theoretical values, $D_{12}$(calc.).

For the A-Ne mixture, however, the observed $D_{12}$, as shown in Table (5.11) increases with increasing concentration (and pressure) for concentrations greater than 0.1. This deviation in the observed values of $D_{12}$ arises from a deviation in the linewidths of the Brillouin lines. At this stage we can only speculate on the cause of this effect. There are two factors which could cause this deviation. These are the concentration and the ratio of atomic masses of the constituents. In the Kr-He mixture the concentration was very low and the ratio of atomic masses large, while in the A-Ne mixture the concentration was high and the ratio of the atomic masses was small. (The shortage of time has prevented further investigation into this effect to be made in this work).

Using the observed mutual diffusion coefficient we can (in principle) use equation (5.7) to obtain the atomic radius, $\sigma_{12}$, of the mixture (17). Taking the mean of the values of $D_{12}$ for the Kr-He mixture and the lower concentration values ($C < 0.1$) of $D_{12}$ for the A-Ne mixture we obtain $\sigma_{12}$(Kr-He) = $(3.6 \pm 0.5)\times10^{-8}$ cm and $\sigma_{12}$(A-Ne) = $(3.1 \pm 0.5)\times10^{-8}$ cm. These are compared with the values of $\frac{1}{2}(\sigma_1 + \sigma_2)$ (16) for the mixtures in Table (5.12).

We have also shown in Table (5.12) the values of $D_{12}$ (reduced to STP) and the values of previous measurements quoted by Chapman and Cowling (17).

Table 5.12: $D_{12}$ reduced to STP and $\sigma_{12}$ for Kr-He and A-Ne mixtures

| Mixture | $D_{12}$ ($cm^2$ $s^{-1}$) | | $\sigma_{12} \times 10^8$ (cm) | $\frac{1}{2}(\sigma_1+\sigma_2) \times 10^8$ (cm) (16) |
|---|---|---|---|---|
| | Ref (17) | This work ± .08 | ± .5 | |
| Kr-He | 0.558 | 0.43 | 3.6 | 3.16 |
| A-Ne | 0.276 | 0.28 | 3.1 | 3.11 |

## 5.3. Concluding Remarks

The experimental results in this work show that the hydrodynamic equations describe adequately the evolution of the correlation functions of the thermodynamic parameters in simple liquid systems and gaseous systems at moderate pressures. This is illustrated by the agreement between theoreticalpredictions and experimental observations in the systems investigated.

This work also demonstrated the versatility and accuracy of light scattering as a tool applied to fluid systems.

References in Chapter V

(1) I.L. Fabelinskii; 'Molecular Scattering of Light', Plenum Press (1968)

(2) C.P. Abbis, C.M. Knobler, D.K. Teague, C.J. Pings, J. Chem. Phys. 42, 4145 (1965)

(3) A.C. Sinnock, B.L. Smith; Phys. Rev. 181, 1297 (1969)

(4) R.A. Aziz, D.H. Bowman, C.C. Lim; Can. J. Chem. 45 2079 (1967)

(5) Reference 12 of Chapter IV

(6) Parameters used to calculate the values of $\alpha_c$ were obtained from various works:
J.P. Boon, G. Thomaes; Physica 29, 208 (1963)
J.P. Boon, J.C. Legros, G. Thomaes; Physica 33 547 (1967)
S. Förster; Cryogenics 3, 176 (1963)
C. Gladun, F. Henzel; Cryogenics 10, 210 (1971)
G.A. Cook; 'Argon, Helium and the Rare Gases' Interscience Publications, N.Y., London (1961)

(7) D.G. Naugle; J. Chem. Phys. 44, 741 (1966)

(8) J.A. Cowan, R.N. Ball; Canadian J. Physics 50 1881 (1972)

(9) Reference 1.
A.B. Bhatia; 'Ultrasonic Absorption' Oxford University Press (1967)

(10) J. Marcoux; Canadian J. Phys. 48 243 (1970)
J. Marcoux; Canadian J. Phys. 48 1947 (1970)

(11) Reference 15 of Chapter II

(12) Compare the data in reference (4) with those of J. Thoen, E. Vangeel, W. Van Dael; Physica 45, 339 (1969)

(13) P. Gray, S.A. Rice; J. Chem. Phys. 41 3689 (1964)

(14) E.V. Larson, D.G. Naugle, T.W. Adair III; J. Chem. Phys. 54, 2429 (1971)

(15) J. Kestin, Y. Kobayashi, R.T. Wood; Physica 32, 1065 (1966)

(16) J.O. Hirschfelder, C.F. Curtis, R.P. Bird; 'Molecular Theory of Gases and Liquids' John Wiley and Sons, Inc. (1964)

(17) S. Chapman, T.G. Cowling; 'The Mathematical Theory of Non-Uniform Gases' (Third Edition) Cambridge University Press (1970).

# APPENDIX I

## The Solution of Differential Equations using Laplace and Fourier Transforms

As seen in the text, in Chapters II and III (equations 2.27 - 29 and 3.8 - 11) the linearized hydrodynamic equations are differential equations involving derivatives with respect to $\bar{r}$ and t. The use of integral transforms in solving such equations is very well known.

These integral transforms have been introduced in the text as a sequential outcome of the discussion towards the derivation of the form of the spectrum of the scattered light. Hence we introduced the Fourier transform:

$$X(\bar{K}) = \int_{-\infty}^{\infty} d\bar{r} e^{-i\bar{K}.\bar{r}} X(\bar{r}) \qquad (I.1)$$

and the Laplace transform:

$$X(s) = \int_{0}^{\infty} dt\, e^{-st} X(t) \; ; \quad s = i\omega \qquad (I.2)$$

With the definitions (I.1) and (I.2) differential equations are transformed into multiplications by powers of -iK and -s; thus we have the transformation relations:

$$\nabla X(\bar{r}, t) \longrightarrow -i K X(K, t)$$

$$\nabla \cdot X(\bar{r}, t) \longrightarrow -i K \cdot X(K, t) \qquad (I.3)$$

$$\nabla^2 X(\bar{r}, t) \longrightarrow -K x (K, t)$$

$$\frac{\partial}{\partial t} X(\bar{r}, t) \longrightarrow sX(\bar{r}, s) - X(\bar{r}, 0)$$

As an example of the application of these transformations we take the energy transport equation (2.29):

$$\rho_0 C_v \frac{\partial T}{\partial t}(\bar{r}, t) - \frac{C_v(\gamma-1)}{\beta} \frac{\partial \rho}{\partial t}(\bar{r}, t) - \lambda \nabla^2 T(\bar{r}, t) = 0 \qquad (I.4)$$

Applying Laplace transform on the time coordinate in (I.4) we obtain:

$$\rho_0 C_v \left[sT(\bar{r}, s) - T(\bar{r}, 0)\right] - \frac{C_v(\gamma-1)}{\beta} \left[ s\rho(\bar{r}, s) - \rho(\bar{r}, 0)\right]$$

$$- \lambda \nabla^2 T(\bar{r}, s) = 0 \qquad (I.5)$$

The spatial coordinate can then be Fourier transformed to yield:

$$\rho_0 C_v \left[sT(K, s) - T(K, 0)\right] - \frac{C_v(\gamma-1)}{\beta} \left[ s\rho(K, s) - \rho(K, 0)\right]$$

$$+ \lambda K^2 T(K, s) = 0 \qquad (I.6)$$

On rearranging (I.6) we get the familiar form:

$$T(K, s)\left[\rho_0 C_v s + \lambda K^2\right] - \rho(K, s)\left[\frac{C_v(\gamma-1)}{\beta}\right]$$

$$= T(K, 0)\ \rho_0 C_v - \rho(K, 0)\ \frac{C_v(\gamma-1)}{\beta} \qquad (I.7)$$

Similarly, the transformations can be applied to the other hyrdodynamic equations to obtain $X(K, s)$ in terms of $X(K, 0)$.

The inverse Laplace transformation is facilitated, as described in the text, by solving the dispersion equation $D(s) = 0$. A scheme for finding the approximate roots of polynomial equations in a power series of the coefficients is outlined in appendix II. Having obtained the roots of the dispersion equation, say, $s_1$, $s_2$, ... $s_n$, it is then a matter of algebraic manipulations to break up $\frac{N(s)}{D(s)}$ into partial fractions:

$$\frac{N(s)}{D(s)} = \frac{A}{(s-s_1)} + \frac{B}{(s-s_2)} + \cdots \frac{R}{(s-s_n)} \qquad (I.8)$$

whose inverse can be obtained from tables of standard Laplace transform pairs.

# APPENDIX II

## Solution of Polynomial Equations in terms of a power series of the Coefficients

Here we outline the scheme for obtaining approximate solutions to a polynomial equation in terms of a power series of the coefficients. This scheme is applicable to polynomial equations whose coefficients are power series of certain parameters which we can form the solution of, i.e. the equation is of the form:

$$X^n + A\alpha X^{n-1} + (B\alpha + C\alpha^2)X^{n-2} + \ldots + \alpha^r = 0 \qquad \text{(II.1)}$$

This scheme is easily illustrated using a specific example. To this end we take the dispersion equation (2.36), which is of the form:

$$X^3 + A\alpha^2 X^2 + (B\alpha^2 + C\alpha^4)X + D\alpha^4 = 0 \qquad \text{(II.2)}$$

to which we try to find solutions of the form

$$X = a_0 + a_1\alpha + a_2\alpha^2 + \ldots \qquad \text{(II.3)}$$

By inspection we can infer that $a_0 = 0$.
Hence we have in this case

$$X = a_1\alpha + a_2\alpha^2 + \ldots \qquad \text{(II.4)}$$

Substituting (II.4) into (II.2) and equating successive powers of $\alpha$ to zero we get (for the two lowest powers of $\alpha$)

$$a_1(a_1^2 + B) = 0 \qquad \text{(II.5)}$$

$$3a_1^2 a_2 + Aa_1^2 + Ba_2 + D = 0 \qquad \text{(II.6)}$$

(II.5) gives 3 values of $a_1$ which are

$$a_1 = \begin{cases} 0 \\ \pm\sqrt{-B} \end{cases}$$

Substituting these values of $a_1$ into (II.6) we get the values of $a_2$ which are

$$a_2 = \begin{cases} -D/B \\ -\frac{1}{2}(A - D/B) \end{cases}$$

Putting these values of $a_1$ and $a_2$ into (II.4) we get the roots of the equation (II.2) to the second order in $\alpha$:

$$\left.\begin{aligned} X &= -(D/B)\alpha^2 \\ X_+ &= +(\sqrt{-B})\alpha - \tfrac{1}{2}(A-D/B)\alpha^2 \\ X_- &= -(\sqrt{-B})\alpha - \tfrac{1}{2}(A-D/B)\alpha^2 \end{aligned}\right\} \qquad \text{(II.7)}$$

The process can be extended to higher orders if necessary.

The complication increases with increasing order of the polynomial equation, however, this scheme yields solutions much easier than solving the equation algebraically. Indeed for polynomial equations of order > 3 where an exact algebraic method is not available this scheme is very appropriate.

# APPENDIX III

## Procedure for Preparing a Gas Mixture of a given Concentration

Here we outline the derivation of equations (4.32-33) in the text, concerning the relationship of the pressure and concentration of the gas mixture. Ideal gas condition is assumed throughout this discussion.

For a given volume the partial pressure $P_i$ of the component i of the mixture is proportional to the molar fraction, $x_i$, of the component. Writing x as the molar fraction of the second component, we have

$$x = \frac{P - P_0}{P} \qquad \text{(III.1)}$$

or

$$P = P_0/(1 - x) \qquad \text{(III.2)}$$

where P is the total pressure of the mixture and $P_0$ is the pressure of the first component, (already in the sample volume).

The concentration, C, of the mixture is defined as:

$$C = \frac{\text{mass of component \#2}}{\text{mass of component \#1}}$$

$$= \frac{xM_2}{(1-x)M_1} \qquad \text{(III.3)}$$

where $M_1$ and $M_2$ are the molar masses of the components respectively.

Rearranging (III.3) we obtain:

$$x = \frac{CM_1}{CM_1 + M_2} \qquad \text{(III.4)}$$

Putting (III.4) into (III.2) we have the result:

$$P = P_0\left(1 + C\frac{M_1}{M_2}\right) \qquad \text{(III.5)}$$

Now, as shown in Figure (4.23) the system consists of the sample cell and the pressure line. Here we define the following:

$V_l$ = volume of pressure line,

$V_C$ = volume of sample cell,

$R = V_C/V_l$,

$P_C$ = pressure in the cell,

$P$ = pressure required in the cell,

$P_l$ = pressure required in the pressure line.

The procedure for changing the concentration of the mixture is to introduce enough of the second component into the cell to a pressure given by (III.5). To obtain this the pressure line is filled up to a pressure $P_l$ and the system is then isolated from the gas cylinders. The gas in the pressure line is then allowed to flow into the

sample cell until the pressures in the sample cell and pressure line equalise. This process is described by the equation:

$$P_l V_l + P_C V_C = P(V_l + V_C) \qquad \text{(III.6)}$$

Rearranging this equation and substituting (III.5) for P we finally obtain:

$$P_l = P + R(P - P_C)$$

The value of R has to be determined experimentally.

Appendix IV.

```
        LORENTZIAN FITTING;
"BEGIN"
"REAL"G1,G2,RET,RH,BH;
"INTEGER" I,NP,N,L,K,J,R,E,PLOT;
"INTEGER""ARRAY" IM[1:50];
"REAL""ARRAY"XD,YD[1:1000],XX,YFX[1:2500],XPEAK,YPEAK[1:20];
"READ" READER(6),NP,PLOT;
"FOR"I:=1"STEP"1"UNTIL"NP"DO"
"BEGIN""READ" READER(1),YD[I]; XD[I]:=I-1; "END";
"BEGIN" "REAL" MAX,MIN; MAX:=0.0;
"FOR"I:=1"STEP"1"UNTIL"NP"DO"
"IF"YD[I]>MAX"THEN"MAX:=YD[I];
"FOR" I:=1"STEP"1"UNTIL"NP"DO"
YD[I]:=YD[I]/MAX;
MIN:=MAX;
"FOR"I:=1"STEP"1"UNTIL"NP"DO"
"IF"YD[I]<MIN"AND"YD[I]>0.000000"THEN"MIN:=YD[I];
K:=1; "FOR"I:=3"STEP"1"UNTIL"(NP-2)"DO"
"BEGIN" "IF"YD[I]>YD[I-1]"AND"YD[I]>YD[I+1]"THEN"
"BEGIN" J:=I; "IF"YD[J]>100*MIN"THEN"
"BEGIN" "IF"YD[J-1]>YD[J-2]"AND"YD[J+1]>YD[J+2]"THEN"
"BEGIN" IM[K]:=J; YPEAK[K]:=YD[IM[K]]; XPEAK[K]:=XD[IM[K]];
R:=K;K:=K+1;  "END";"END";"END";"END";
"FOR"K:=1"STEP"1"UNTIL"R"DO"
"PRINT"SAMELINE,''S5``,'PEAK`,K,'AT`,XPEAK[K],''L``;
RH:=(YPEAK[2]+YPEAK[5])/2;
BH:=(YPEAK[1]+YPEAK[3]+YPEAK[4]+YPEAK[6])/4; RET:=BH/RH;
 "END";
"BEGIN""REAL"PT;"ARRAY"G[1:R];
"FOR"K:=1"STEP"1"UNTIL"R"DO"
"BEGIN" G[K]:=0.0; I:=IM[K]; PT:=YD[I];
J:=I;
INC: J:=J+1; "IF"YD[J]>PT/2"THEN""GOTO"INC;
G[K]:=J-I;
J:=I;
DEC: J:=J-1; "IF"YD[J]>PT/2"THEN""GOTO"DEC;
G[K]:=(G[K]+(I-J))/2;
"END";
"FOR"K:=1"STEP"1"UNTIL"R"DO"
"PRINT"''S5``,G[K],''L``;
G1:=(G[2]+G[5])/2; G2:=(G[1]+G[3]+G[4]+G[6])/4;
"END";
"PRINT"SAMELINE,G1,G2,XPEAK[1],XPEAK[2],XPEAK[3],XPEAK[4],XPEAK[5],
XPEAK[6],''L``;
"BEGIN"
"INTEGER" M,Q;
"REAL"DG1,DG2,DX1,DX2,DX3,DX4,DX5,DX6,FN,F1,F2,F3,F4,F5,F6,C1,C2,
B1,B2,B3,B4,B5,B6,A1,A2,X1,X2,X3,X4,X5,X6,GR1,GR2,GX1,GX2,GX3,GX4,
GX5,GX6,RES;
X1:=XPEAK[1]; X2:=XPEAK[2]; X3:=XPEAK[3]; X4:=XPEAK[4]; X5:=XPEAK[5];
X6:=XPEAK[6];
C1:=G1;     C2:=G2;
Q:=0;
ITERT1: RES:=DG1:=DG2:=0.0;
A1:=G1*G1; A2:=RET*G2*G2;
"FOR"I:=1"STEP"1"UNTIL"NP"DO"
```

```
  "BEGIN"
  F1:=XD[I]-X1;
  F2:=XD[I]-X2;
  F3:=XD[I]-X3;
  F4:=XD[I]-X4;
  F5:=XD[I]-X5;
  F6:=XD[I]-X6;
  B1:=F1*F1+G2*G2;
  B2:=F2*F2+G1*G1;
  B3:=F3*F3+G2*G2;
  B4:=F4*F4+G2*G2;
  B5:=F5*F5+G1*G1;
  B6:=F6*F6+G2*G2;
FN:=A1*(1.0/B2+1.0/B5)+A2*(1.0/B1+1.0/B3+1.0/B4+1.0/B6)-YD[I];
  RES:=RES+YD[I]*FN*FN;
  DG1:=DG1+2*G1*((F2*F2)/(B2*B2)+(F5*F5)/(B5*B5))*FN;
  DG2:=DG2+2*RET*G2*((F1*F1)/(B1*B1)+(F3*F3)/(B3*B3)+(F4*F4)/(B4*B4)
   +(F6*F6)/(B6*B6))*FN;
  "END";
  GR1:=G1-RES/(DG1*NP);
  GR2:=G2-RES/(DG2*NP);
M:=0;    Q:=Q+1;
  "IF"ABS(GR1-G1)>0.01"AND"GR1>C1/2.0"THEN"
  "BEGIN"  "IF" GR1<C1. "THEN"
  "BEGIN" G1:=GR1; M:=M+1; "END";    "END";
  "IF"ABS(GR2-G2)>0.01"AND"GR2>C2/2.0"THEN"
  "BEGIN" "IF"GR2<C2 "THEN"
  "BEGIN" G2:=GR2; M:=M+1; "END";   "END";
"PRINT"SAMELINE,G1,``S3``,G2,``L``;
"IF"M>0"AND"Q<10"THEN""GOTO"ITERT1;
Q:=0;
  A1:=G1*G1; A2:=RET*G2*G2;
ITERT2:RES:=DX1:=DX2:=DX3:=DX4:=DX5:=DX6:=0.0;
  "FOR"I:=1"STEP"1"UNTIL"NP"DO"
  "BEGIN"
  F1:=XD[I]-X1;
  F2:=XD[I]-X2;
  F3:=XD[I]-X3;
  F4:=XD[I]-X4;
  F5:=XD[I]-X5;
  F6:=XD[I]-X6;
  B1:=F1*F1+G2*G2;
  B2:=F2*F2+G1*G1;
  B3:=F3*F3+G2*G2;
  B4:=F4*F4+G2*G2;
  B5:=F5*F5+G1*G1;
  B6:=F6*F6+G2*G2;
FN:=A1*(1.0/B2+1.0/B5)+A2*(1.0/B1+1.0/B3+1.0/B4+1.0/B6)-YD[I];
  RES:=RES+YD[I]*FN*FN;
  DX1:=DX1+2*RET*G2*G2*F1/(B1*B1)*FN;
  DX2:=DX2+2*G1*G1*F2/(B2*B2)*FN;
  DX3:=DX3+2*RET*G2*G2*F3/(B3*B3)*FN;
  DX4:=DX4+2*RET*G2*G2*F4/(B4*B4)*FN;
  DX5:=DX5+2*G1*G1*F5/(B5*B5)*FN;
  DX6:=DX6+2*RET*G2*G2*F6/(B6*B6)*FN;
  "END";
```

```
  GX1:=X1-RES/(DX1*NP);
  GX2:=X2-RES/(DX2*NP);
  GX3:=X3-RES/(DX3*NP);
  GX4:=X4-RES/(DX4*NP);
  GX5:=X5-RES/(DX5*NP);
  GX6:=X6-RES/(DX6*NP);
M:=0;O:=O+1;
  "IF"ABS(GX1-X1)>0.01"AND"ABS(GX1-X1)<2.0"THEN"
  "BEGIN" X1:=GX1;M:=M+1;"END";
  "IF"ABS(GX2-X2)>0.01"AND"ABS(GX2-X2)<2.0"THEN"
  "BEGIN" X2:=GX2;M:=M+1;"END";
  "IF"ABS(GX3-X3)>0.01"AND"ABS(GX3-X3)<2.0"THEN"
  "BEGIN" X3:=GX3;M:=M+1;"END";
  "IF"ABS(GX4-X4)>0.01"AND"ABS(GX4-X4)<2.0"THEN"
  "BEGIN" X4:=GX4;M:=M+1;"END";
  "IF"ABS(GX5-X5)>0.01"AND"ABS(GX5-X5)<2.0"THEN"
  "BEGIN" X5:=GX5; M:=M+1;"END";
  "IF"ABS(GX6-X6)>0.01"AND"ABS(GX6-X6)<2.0"THEN"
  "BEGIN" X6:=GX6;M:=M+1;"END";
"PRINT"SAMELINE,X1,X2,X3,X4,X5,X6,''L``;
"IF"M>0"AND"O<10"THEN""GOTO"ITERT2;
  XPEAK[1]:=X1; XPEAK[2]:=X2;XPEAK[3]:=X3;XPEAK[4]:=X4;XPEAK[5]:=X5;
  XPEAK[6]:=X6;
  "END";
"PRINT"''L3``;
  "PRINT"SAMELINE,XPEAK[1],XPEAK[2],XPEAK[3],XPEAK[4],XPEAK[5],
  XPEAK[6],G1,G2,''L``;
  "BEGIN"
  "REAL" A1,A2,F1,F2,F3,F4,F5,F6,X1,X2,X3,X4,X5,X6;
  A1:=G1*G1;  A2:=RET*G2*G2;
  X1:=XPEAK[1]; X2:=XPEAK[2]; X3:=XPEAK[3]; X4:=XPEAK[4];
  X5:=XPEAK[5];  X6:=XPEAK[6];
  "FOR"I:=1"STEP"1"UNTIL"2000"DO"
  "BEGIN"
  XX[I]:=(I-1)*NP/1999;
  F1:=(XX[I]-X1)*(XX[I]-X1) + G2*G2;
  F2:=(XX[I]-X2)*(XX[I]-X2) + G1*G1;
  F3:=(XX[I]-X3)*(XX[I]-X3) + G2*G2;
  F4:=(XX[I]-X4)*(XX[I]-X4) + G2*G2;
  F5:=(XX[I]-X5)*(XX[I]-X5) + G1*G1;
  F6:=(XX[I]-X6)*(XX[I]-X6) + G2*G2;
YFX[I]:=A1*(1.0/F2+1.0/F5) +A2*(1.0/F1+1.0/F3+1.0/F4+1.0/F6);
  "END";          "END";
  "BEGIN"
  K:=1;
  "FOR"I:=2"STEP"1"UNTIL"1999"DO"
  "BEGIN" "IF" YFX[I]>YFX[I-1]"AND"YFX[I]>YFX[I+1]"THEN"
  "BEGIN" J:=I;  YPEAK[K]:=YFX[J]; XPEAK[K]:=XX[J];
  R:=K; K:=K+1; "END"; "END";
"PRINT"''L3``;
  "FOR"K:=1"STEP"1"UNTIL"R"DO"
  "PRINT" SAMELINE,XPEAK[K],YPEAK[K],''L``;
  "FOR"K:=1"STEP"1"UNTIL"R"DO"
  "PRINT"SAMELINE,''S5``,'PEAK`,K,'AT`,XPEAK[K],''L``; "END";
"IF"PLOT>2"THEN""GOTO"SKIP1;
"BEGIN""REAL"YM,XM,XSCL,YSCL;"INTEGER"MP,TP;
```

```
  SETORIGIN(2400,1);
DRAWLINE(1800,0);
  MOVEPEN(0,0);
YM:=YPEAK[1];XM:=NP-1;YSCL:=300/YM;XSCL:=1800/XM;
MP:=ENTIER(XD[1]*XSCL); TP:=ENTIER(YD[1]*YSCL);
MOVEPEN(MP,TP); CENCHARACTER(1);
"FOR"I:=2"STEP"1"UNTIL"NP"DO"
  "BEGIN"
TP:="IF"YD[I]*YSCL"LE"1100"THEN"ENTIER(YD[I]*YSCL)"ELSE"1100;
MP:=ENTIER(XD[I-1]*XSCL);
  MOVEPEN(MP,TP); CENCHARACTER(1);
  "END";
  MOVEPEN(0,0);
XM:=2000.0-1.0;XSCL:=1800.0/XM;
TP:=ENTIER(YFX[1]*YSCL); MOVEPEN(0,TP);
  "FOR"I:=2"STEP"1"UNTIL"2000"DO"
  "BEGIN"
TP:="IF"YFX[I]*YSCL"LE"1100"THEN"ENTIER(YFX[I]*YSCL)"ELSE"1100;
MP:=ENTIER((I-1)*XSCL);
  DRAWLINE(MP,TP);
  "END";
MOVEPEN(2400,0);
  "END"   GRAPHPLOT;
SKIP1:  "END"  CURVEFIT;
```